UNIVERSITÀ
DEGLI STUDI
DI PADOVA

Sede amministrativa: Università degli Studi di Padova

Dipartimento di Astronomia

SCUOLA DI DOTTORATO DI RICERCA IN ASTRONOMIA
CICLO XXIII

Timing studies of compact objects

Direttore della Scuola: Ch.mo Prof. Giampaolo Piotto

Supervisore: Ch.mo Prof. Luca Zampieri

Dottorando: Claudio Germanà

Contents

Riassunto

Le proprietà della variabilità temporale nelle sorgenti astrofisiche sono di notevole interesse e riguardano una vasta gamma di fenomeni che si sviluppano in diversi tipi di oggetti. In questa tesi di dottorato abbiamo investigato due classi di fenomei astrofisici, entrambi legati a studi sulla varabilità temporale. La tesi presenta l'analisi scientifica dei dati raccolti dalla Crab pulsar con gli innovativi contatori di fotoni ottici Aqueye e Iqueye, la cui risoluzione temporale è la più alta mai raggiunta nel dominio ottico (centinaia di picosecondi). Aqueye (Barbieri et al. 2008, 2009) è stato progettato per essere montato al telescopio Copernico in Asiago. Iqueye (Naletto et al. 2009, 2010) è una versione innovativa e progettato per il telescopio NTT in La Silla.
Altre investigazioni qui descritte riguardano lo sviluppo e la verifica di idee per interpretare e modellizzare la variabilità temporale al millisecondo osservata in sistemi binari X.

Per quanto riguarda l'analisi scientifica dei dati dalla Crab pulsar, essa richiede che ai fotoni raccolti venga associato, con alta precisione, il rispettivo tempo di arrivo secondo un osservatore inerziale. Quindi dobbiamo riferire il tempo di arrivo dei fotoni (TOAs) ad un sistema di riferimento che approssimi al meglio uno inerziale. Solitamente i TOAs all'osservatorio vengono trasformati in TOAs misurati da un osservatore al baricentro del sistema solare. Tempo2 (Hobbs et al. 2006a; Edwards et al. 2006) è un software sviluppato per modelizzare con estrema precisione ($\sim$ 1 ns) i TOAs misurati in un sistema di riferimento inerziale.

Dopo aver baricentrizzato i TOAs, abbiamo usato un codice numerico per calcolare la fase della Crab pulsar. Dallo studio dell'andamento della fase nel tempo è possibile misurare il periodo di rotazione della stella di neutroni e sue derivate.
L'analisi dei residui in fase rispetto al modello standard può rivelare peculiarità della sorgente e dell'ambiente circostante. Con questo tipo di analisi è possibile anche verificare la bontà del modello che corregge i tempi di arrivo al baricentro del sistema solare. Se c'è qualche discrepanza inaspettata allora

è interessante investigare sulla sua origine fisica. Un risultato importante ottenuto dall'analisi dei residui in fase è stata la scoperta del primo sistema planetario extrasolare attorno alla pulsar PSR B1257+12 (Wolszczan & Frail 1992; Wolszczan 1994; Konacki & Wolszczan 2003). Altri studi riguardano verifiche della teoria della Relatività Generale (Helfand et al. 1980; Kramer et al. 2006). Inoltre, il timing delle pulsars è stato proposto come potenziale strumento per la rivelazione di onde gravitazionali (Stappers et al. 2006; Manchester 2010).

Dall'analisi dei residui in fase sono state notate inaccuratezze nel ricostruire i TOAs al baricentro del sistema solare, dovute a problemi con i files di configurazione del software Tempo2. Una volta risolti questi problemi, possiamo concludere che i periodi di rotazione della Crab pulsar misurati con Aqueye/Iqueye sono in accordo entro qualche picosecondo con quelli riportati nell'archivio radio del Jodrell Bank Observatory.
I TOAs dei fotoni generano una componente di rumore che segue la statistica di Poisson. Le differenze tra i periodi radio e ottici sono maggiori dell'errore Poissoniano stimato. Con i dati raccolti da Aqueye/Iqueye è stato possibile misurare la derivata prima del periodo di rotazione già con osservazioni su una base temporale di soli 2 giorni. Anche in questo caso abbiamo notato discrepanze maggiori dell'errore statistico.
Misurando il tempo di arrivo del picco ottico al baricentro del sistema solare e confrontandolo con quello riportato nell'archivio radio, è stato ricavato il ritardo temporale del picco radio rispetto a quello ottico. Il picco ottico arriva $\sim 120\mu s$ in anticipo rispetto a quello radio, in accordo con altri osservatori (Shearer et al. 2003; Oosterbroek et al. 2008). L'analisi ha anche rivelato un deriva della fase ottica rispetto a quella radio che sembra essere legata alle discrepanze già menzionate tra i periodi di rotazione. Ulteriori investigazioni hanno portato alla preliminare conclusione che il segnale ottico dalla Crab pulsar potrebbe essere influenzato da una componente di rumore che non segue la statistica di Poisson, conosciuto come *timing noise*. Rumore non Poissoniano nel segnale da stelle di neutroni è stato rivelato da diversi autori (Boynton et al. 1972; Lyne et al. 1993; Scott et al. 2003; Hobbs et al. 2006b; Patruno et al. 2009), comunque su basi temporali di mesi o anni. Ulteriori osservazioni sono necessarie per verificare la presenza di rumore non Poissoniano su scale di giorni.

In questa tesi di dottorato è stata anche esplorata qualche idea sulla interpretazione e modelizzazione della variabilità temporale al millisecondo, osservata nel flusso X delle Low Mass X-ray Binaries (LMXBs; e.g. van der Klis 2004). Queste oscillazioni quasi-periodiche (QPOs), a frequenze fino a 1200 Hz, sono state rivelate con i contatori di fotoni X a bordo del satellite Rossi X-ray Timing Explorer (RXTE; Bradt et al. 1993). Oscillazioni al mil-

lisecondo sono tipiche del tempo scala orbitale a distanze prossime all'oggetto compatto. Lo studio temporale di queste sorgenti potrebbe essere un modo indiretto per studiare il moto della materia in uno spazio-tempo fortemente curvato, quindi per verificare la teoria della Relatività Generale in regime di campo forte.
La tesi descrive qualche idea per interpolare le frequenze dei moti relativistici, calcolate per orbite nella metrica di Kerr, con i QPOs osservati nelle LMXBs. Abbiamo calcolato il chi-quadro ridotto (χ^2/dof) su una griglia di masse e momenti angolari e notato che il minimo χ^2/dof si ottiene per masse della stella di neutroni maggiori di 2 $M_\odot$. Questi valori sono grandi rispetto alla usuale massa di una stella di neutroni ($1.4M_\odot$) ottenuta dalle pulsar binarie. Comunque, in sistemi binari in accrescimento come le LMXBs, è stata misurata una massa della stella di neutroni maggiore di quella tipica (Casares et al. 2006, 2010). Va precisato che, utilizzare i QPOs al millisecondo per ottenere stime precise della massa di una stella di neutroni potrebbe non essere ancora un metodo sicuro, vista la complessità della fenomenologia e le tuttora poco chiare proprietà.

Se i QPOs ad alta frequenza nel flusso X delle LMXBs sono prodotti da corpi che orbitano in prossimità dell'oggetto compatto, allora un modello consistente dovrebbe prendere in cosiderazione anche l'evoluzione della loro forma in uno spazio-tempo curvo. In collaborazione con il Dipartimento di Fisica e di Matematica dell'Università di Ljubljana abbiamo simulato curve di luce e spettri di potenza prodotti da un oggetto costituito da particelle libere orbitanti un buco nero di Schwarschild. Durante il moto orbitale la forma dell'oggetto è fortemente alterata dall'intensa forza mareale del buco nero (Čadež et al. 2008; Kostić et al. 2009). Tali simulazioni numeriche sono in grado di riprodurre lo spettro di potenza osservato nella LMXB con un buco nero XTE J1550-564 (Germanà et al. 2009).

Abstract

The detailed knowledge of the temporal behaviour of astrophysical objects is one of the main sources of information about physical processes occurring in several classes of objects. In this PhD thesis we investigated two different astrophysical topics, both of them linked to timing. We present the scientific analysis of the data collected from the Crab pulsar by means of the novel optical extremely fast-photon counters Aqueye and Iqueye, that have the best temporal resolution ever achieved in the optical domain (hundreds of picoseconds). Aqueye (Barbieri et al. 2008, 2009) was designed to be mounted at the Copernico telescope in Asiago. Iqueye (Naletto et al. 2009, 2010) is an improvedversion for the NTT telescope.
Here we also discuss some ideas on modelling the millisecond variability observed in the X-ray flux from Low Mass X-ray Binaries with either a neutron star or a black hole.

The timing analysis of the optical emission from the Crab pulsar requires to time-tag with extreme precision the photons as collected by an inertial observer. Therefore we must refer the time of arrival of photons (TOAs) to a reference frame that approximates an inertial frame to the level of precision needed. One usually refers TOAs to a reference system located at the solar system barycenter. Tempo2 (Hobbs et al. 2006a; Edwards et al. 2006) is a software meant to model with extreme precision (up to $\sim$1 ns) TOAs as collected by an inertial observer.
After baricentering TOAs a numerical code making use of a standard template was used to determine the phase of the mean peak of the Crab pulsar profile. By studying the phase behaviour it is possible to extract information about both the rotational period of the fast rotating neutron star and its derivatives. Moreover, the analysis of the phase-residuals left out after subtracting the standard pulsar timing model may reveal interesting features of the pulsar and its surroundings. With the anlysis of the residuals one can also check for possible discrepancies on the modelling. If some systematic residuals show up, then it is interesting to investigate the physical origin. Just to quote a few noticeable examples, we mention the discovery of the first extra-

solar planetary system around the pulsar PSR B1257+12, obtained from the analysis of pulsar phase-residuals (Wolszczan & Frail 1992; Wolszczan 1994; Konacki & Wolszczan 2003). Other foundamental results deal with tests of General Relativity theory (Helfand et al. 1980; Kramer et al. 2006). Moreover, pulsar timing is now being planned as a tool to reveal gravitational wave (Stappers et al. 2006; Manchester 2010).

The analysis of the optical phase-residuals of the Crab pulsar we performed has revealed poor corrections in the Roemer delay due to the Tempo2 configuration files. After correcting for them we can conclude that the rotational periods of the Crab pulsar measured by Aqueye/Iqueye agree with those quoted in the Jodrell Bank radio archive up to a few picoseconds.
The TOAs from a photon-counter usually are affected by noise that obeys the Poisson statistics. We noticed possible discrepancies between the radio and optical rotational periods larger than the estimated Poissonian error, but a more extensive analysis of the pulsar timing noise and related errors is needed before any definitive conclusion can be drawn. We were able to measure the spin down of the neutron star already over a baseline of a few days. Discrepancies with that reported in the Jodrell Bank radio archive are underlined.
By comparing the time of arrival of the optical peak at the solar system barycenter with that quoted in the Jodrell Bank radio ephemerides archive we find a radio-optical delay in agreement with that reported in the literature (Shearer et al. 2003; Oosterbroek et al. 2008), that is, an optical peak leading the radio one by $\sim 120\mu s$. We also noticed same radio-optical phase drift with time, which may be related to the radio-optical rotational period discrepancies mentioned above. A further investigation on the possible origin of these discrepancies led to the preliminary conclusion that the signal from the Crab pulsar may be affected by an extra-noise component, known as *timing noise*, not suitable described by the Poissonian statistics. Non-Poissonian noise in the signal from neutron stars has been reported by other authors (Boynton et al. 1972; Lyne et al. 1993; Scott et al. 2003; Hobbs et al. 2006b; Patruno et al. 2009), but using integration times of months or years. Further observations to confirm the existence of non-Poissonian noise in the Crab pulsar are needed.

In this PhD thesis we also present some ideas on the origin of the millisecond X-ray timing variability in the X-ray flux from Low Mass X-ray Binaries (LMXBs), with either a black hole or a neutron star (e.g. van der Klis 2004). These quasi-periodic oscillations (QPOs), at frequencies up to 1200 Hz, were discovered by means of the X-ray photon-counters on board of the Rossi X-ray Timing Explorer satellite (RXTE; Bradt et al. 1993). Millisecond time-scales are typical for matter orbiting close to the compact

object. Therefore, timing studies of these sources could provide a way to investigate the motion of matter in a strongly curved space-time, thus probing General Relativity in the strong field limit.
We describe some ideas on fitting relativistic frequencies in the Kerr metric to observed QPO frequencies in LMXBs. Using a grid of masses and specific angular momenta for the neutron star we show that numerical fits have a low χ^2/dof for masses of the neutron star above 2 $M_\odot$. Such masses are bigger than the canonical value $1.4M_\odot$ measured in double radio pulsars. However, in accreting bynary systems a mass of the neutron star larger than the canonical value has been measured (Casares et al. 2006, 2010). We note that precise measurements of neutron star masses by means of millisecond QPOs are uncertain because of the yet poorly understood phenomenology.

If high frequency QPOs in the X-ray flux of LMXBs are produced by orbiting blobs of matter close to the compact object then a full-consistent modelling should also account for the interaction of the shape of the blob with the curved geometry of the space-time. In collaboration with the Department of Mathematics and Physics of the University of Ljubljana we ran simulations of light curves and power spectra produced by clumps of free particles orbiting a Schwarzschild black hole, that are deformed by tidal interaction. The numerical code was developed by Čadež et al. (2008), Kostić et al. (2009). The numerical simulations reproduce the high frequency part of the power spectrum observed in the black hole LMXB XTE J1550-564 (Germanà et al. 2009).

Chapter 1

Scientific Introduction

The studies of the temporal behaviour of the observed phenomena trace the origin of the human being. The repeating seasonal pattern certainly was the first best observed celestial phenomenon in order to sustain a succesful farming culture.

In astronomy we may say that the temporal analysis is "the" basic tool. For example, in cosmology the study of the universe is referred to distances which in turn are measured in term of light travel time. If we want to know more about a galaxy we analyze the light from it, which in turn is a package of oscillating waves over a characteristic time-scale.
Besides the oscillation time-scales of the electromagnetic field, one can get information on astrophysical sources by studying the behaviour of the repeating pattern, if any, displayed by the light emitted. For instance, oscillations in the signal over a characteristic time-scale indicate the source to be an eclipsing binary system.
Nowadays with timing analysis of astrophysical sources we refer to phenomena showing a repeting pattern under the second time-scale. Thus, in order to monitor so short time-scales, fast photometry is needed and the develope of extremely fast photon-counters is certanly important in order to improve timing studies.

1.1 Pulsars: millisecond lighthouses in the sky

Rotating neutron stars certainly are the most representative class of objects showing a well defined repeating pattern in time. These compact objects originate from supernova explosions. Their emission is characterized by pulsations on ms-s time-scales caused by the rotation of the neutron star (at the

expense of their high rotational energy). A beam of radiation, tipically in the radio band, is emitted by their magnetic cups. If the star is oriented in the sky such that both beams, or even one of them, cross the line of sight we see the source like a lighthouse with a pulsation period equal to the rotational period of the neutron star. Since neutron stars have an extreme momentum of inertia, the rotational period should follow a steady spin down due to the loss of rotational energy. Thus the observed pulses are very regular. If not, pulsar timing provides a way to investigate new physical phenomena characterizing the source and its sorrounding.

The first pulsar ever detected in the radio band was PSR J1921+2153 (with a rotational period of 1.337 s; Hewish et al. 1968). At that time, Hewish and collaborators were involved in studying interplanetary scintillation of compact radio sources by means of a newly constructed large dipole array. During the observations carried out over autumn 1967, the first periodic radio signal from the pulsar came up. However, initially the pulsation was not associated with the rotation of a compact star but rather with its possible oscillation.

The discovery by Hewish and collaborators opened a new window on both observational and theoretical astrophysics. Indeed, since then several pulsars were discovered (Large et al. 1968b), in particular two fast-rotating pulars: The Crab pulsar (Staelin & Reifenstein 1968), with a rotational period of only 33 ms, and the Vela pulsar (Large et al. 1968a), with a period of 89 ms. From the theoretical point of view, radio pulsars were the observative firm on the theory endorsing the existence in the universe of compact objects made of neutrons (Baade & Zwicky 1934).

Pulsars do not emit only in the radio band, their emission is distribuited all over the electromagnetic spectrum. Pulsations in the optical band from the Crab pulsar were discovered soon after those in the radio band (Cocke et al. 1969). The 50 ms rotating pulsar B0540 in the Large Magellanic Cloud was discovered in the X-ray band (Seward et al. 1984) and it has been studied in the optical and other energy bands as well (Mignani et al. 2010).

If detected as binary systems, rotating neutron stars can provide a way to study foundamental phenomena of modern physics. Relativistic pulsars are laboratories in which it is possible to test General Relativity theory predictions (Hulse & Taylor 1975; Kramer et al. 2006).
A surprising result reached thanks to the long monitoring of the radio pulsar PSR 1257+12 was the discovery of the first extrasolar planetary system (Wolszczan & Frail 1992; Wolszczan 1994; Konacki & Wolszczan 2003).
Stairs et al. (2000) have shown that young pulsars can freely precess, a result that theoretically is not expected for a single rotating neutron star. Optical studies of the Crab pulsar by Čadež & Galičič (1996), Čadež et al. (1997,

2001) raised the question whether the pulsar in the Crab Nebula freely precesses. If confirmed, free precession can give information on the internal structure of the star, hence on the equation of state of the matter at nuclear density.

Despite their discovery more than 40 years ago, little is known about the emission mechanisms in pulsars. Therefore it has becoming more and more demanding to study these objects in several energy emission bands. In the optical band, the brighter sources are the Crab pulsar ($V \sim 16.5$), the Vela ($V \sim 23.6$) and the pulsar in the Large Magellanic Cloud PSR B0540-69 ($V \sim 22.5$), which are rotation-powered pulsars. However, with the advent of new high time resolution instruments in the optical band both rotation-powered pulsars and magnetars have been discovered. To date, the number of Isolated Neutron Stars (INSs) detected in the ultraviolet, optical and infrared band is 24 (for a general review, see Mignani 2010). INSs have been detected and studied in X-ray (~ 80) and γ-ray bands (~ 60) as well (Becker 2009; Abdo et al. 2010).
A yet unkown phenomenon charcterizing INSs is the noise left out after subtracting the standard slow down model to the data (Cordes & Helfand 1980; Hobbs et al. 2006b). This noise is dubbed *timing noise* and it may be related with physical processes in either the emission energy mechanism (Forman et al. 1974) or the INS sorrounding (Scott et al. 2003). One usually refers the word timing noise to what maybe left out by the modelling because of its yet unkown physics. Recent studies by Patruno et al. (2009) have revealed timing noise also in the X-ray emission from fast-rotating neutron stars hosted in accreting binary systems.

Having in mind the several scientific issues described above, we can say that pulsar timing may provide clues on foundamental physics. For instance, pulsar timing has recently been proposed as a tool to detect gravitational waves emission (Stappers et al. 2006; Manchester 2010).
It appears clear that it is worth to devolepe new improved instrumentations to monitor and study the yet unknown issues of pulsar physics. After a review, in the following we concentrate on the scientific analysis of the optical data collected from the Crab pulsar with the nanosecond-time resolution photon-counters Aqueye (Barbieri et al. 2008, 2009) and Iqueye (Naletto et al. 2009, 2010).

1.2 The pulsar in the Crab Nebula

As well known, the young fast-rotating neutron star in the Crab Nebula (PSR B0531+21 or PSR J0534+2200) displays a light curve with a characteristic

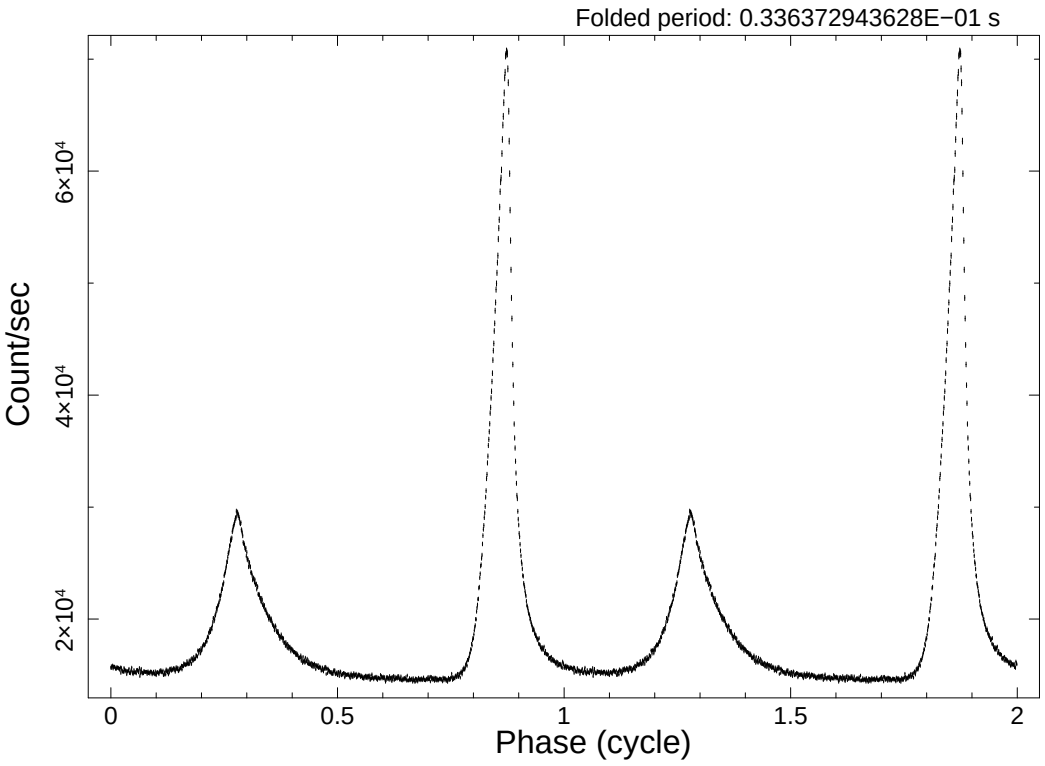

Figure 1.1: Optical light curve profile of the Crab pulsar obtained with Iqueye at the NTT telescope on December 2009. Two rotation of the neutron star are shown. The integration time is $\sim$ 800 s.

double peak profile (see Fig. 1.1) with a rotational period of 33 milliseconds, almost aligned in phase over the whole electromagnetic spectrum. It is the brigthest optical pulsar and the first to be detected as a pulsating source in the optical band (Cocke et al. 1969; Lynds et al. 1969). The central star of the Nebula was optically identified by Minkowski (1942) and later discovered to be a radio source (Bolton et al. 1949). However, it was only about 20 years later that, soon after the detection of the first pulsar by Hewish et al. (1968), pulsating radio emission was observed (Staelin & Reifenstein 1968; Comella et al. 1969), providing strong evidence for a connection with a supernova explosion. The pulsations were later recognized to be Giant Radio Pulses (occasional powerful pulses with an energy thousands times larger than that of the average pulses). The Crab pulsar is also a powerful X-ray and gamma-ray emitter (Bowyer et al. 1964; Haymes et al. 1968).

1.2.1 Multi-wavelenght observations

Several studies concentrated on the pulse shape of the Crab in various photometric bands (e.g. Percival et al. 1993; Lundqvist et al. 1999). The pulse shape is characterized by a double peak profile, separated in phase by $\sim 140°$ and almost aligned through the entire electromagnetic spectrum (although the morphological details differ substantially from radio to Gamma-rays). This clearly suggests that the emission originates from two polar beams from an almost orthogonal rotator. The pulse shape is very stable, despite the secular decrease of the luminosity (Nasuti et al. 1996) and the presence of glitches and timing noise (Lyne et al. 1993). Occasionally small variations of the shape of the pulse have been observed (Karpov et al. 2007). Wavelength-dependent changes in the pulsar properties have been reported also by Fordham et al. (2002).

Precise timing of pulsar light curves in different wavebands (Mignani 2009a; Kanbach et al. 2010) is a powerful tool to constrain theories of the spatial distribution of various emission regions. A time delay most naturally implies that the emission regions differ in position. It has been shown that the main pulse and the interpulse are not aligned in time in the radio, X-ray and Gamma-ray bands, but the high energy photons lead the radio ones (Kuiper et al. 2003; Rots et al. 2004). At optical and radio wavelengths Shearer et al. (2003) and Oosterbroek et al. (2008) performed simultaneous absolute timing and found an optical peak leading the radio one by hundrends of μs. Simultaneous X-ray and optical observations has been performed as well, leading to the conclusions that the X-ray-radio time delay depends on the hardness of the X-ray radiation (Molkov et al. 2010).

1.3 Studies in the Optical band of the Crab pulsar

It is widely accepted that the optical emission of pulsars is synchrotron radiation from relativistic particles that spiral around the pulsar magnetic field lines. The basic engine is the pulsar rotational energy, that is somehow transferred to low-frequency radiation and into accelerating charged particles. The major uncertainty is related to the acceleration mechanism of this relativistic wind. Very little is known about the acceleration site, either surface and magnetic poles or further out near the light cylinder, where the particles rotating with the neutron star field lines reach the velocity of light.

The optical spectrum of the Crab shows a flat, featureless continuum, that is well fitted by a power-law with spectral index $\alpha = 0.1 \pm 0.01$ (Nasuti

et al. 1996). Stroboscopic observations were used to obtain the spectrum during the main pulse and the interpulse, finding a dereddened spectral index $\alpha = -0.2 \pm 0.1$ (Carramiñana et al. 2000). Optical polarization measurements (Mignani 2009b) of the Crab pulsar have also been attempted and showed that the optical emission is highly polarized, especially in the bridge and off-pulse phase (Kanbach et al. 2005). Highly polarised emission strongly depending on the pulse phase has been observed also in the soft Gamma-rays with *INTEGRAL* (Dean et al. 2008). Recently, Słowikowska et al. (2009) studied the linear polarization of the Crab pulsar with very high time resolution (11μs) and showed that degree of optical polarisation and the position angle correlate in surprising details with the light curves at optical wavelengths and at radio frequencies, suggesting a subtle connection between presumed non-coherent (optical) and coherent (radio) emissions.

Short timescale (few minutes) modulations of the phase and amplitude of the optical light curve were investigated by Čadež & Galičič (1996), finding evidence for a 60 s modulation that was interpreted as the pulsar free precession period. This raised the question whether a young fast-rotating neutron star can freely precesses (Čadež et al. 1997, 2001). If confirmed, the Crab free precession could be used to constrain the pulsar moment of inertia and hence the equation of state of nuclear matter.

1.4 Aqueye/Iqueye: extremely fast optical photon-counters

A new generation of extremely fast optical photon counters are being developed in light of the future Extremely Large Telescopes (ELTs; Dravins et al. 2005; Barbieri et al. 2006). Extremely large telescopes such as E-ELT will provide very high photon fluxes, allowing studies on the statistics of the photons collected. Therefore several instrumental features are needed: high quantum efficiency, capability to time tag the arrival time of each photon to better than few tens of picoseconds, high stability clock running for hours, acquisition devices capable to sustain arrival rates from 10 Hz up to 1 GHz. In such way, the time frontier of astronomy will be pushed toward the limit imposed by Heisenberg's principle. Therefore, we have called this novel method to utilize the light from the celestial sources as "Quantum Astronomy".
Modern technologies of single photon detectors, clocks and data storage allow today to reach the wanted photometric capabilities, as we have shown starting from the QuantEye study in the frame of the instrumentation for the

ESO OWL (Dravins et al. 2005; Barbieri et al. 2006) and following developments (Naletto et al. 2007; Barbieri et al. 2008). A valuable contribution to the understanding of pulsar emission mechanisms can certainly comes from studies of very high photon fluxes, time tagged by such very fast photon counters.

While the exploitation of the full "quantum" capability of such novel photometer requires the high photon fluxes insured by the ELTs, an instrument having the above mentioned characteristics will serve two important purposes: on one side, it will serve as a prototype to test in the real astronomical environment those concepts and lead to a final design for an upgraded version for the E-ELT, on the other, it will produce new astrophysical results on a variety of objects, including optical pulsars, thanks to the enormous dynamic range, very low intrinsic noise, extremely accurate time tagging of each detected photon.

To put these expectations to solid tests, a first simple photometer for the 182cm telescope of Asiago, named Aqueye (the Asiago Quantum Eye; Barbieri et al. 2008, 2009) has been built. Subsequently, an improved version for the NTT telescope, Iqueye (the Italian Quantum Eye; Naletto et al. 2009, 2010) has been developed.

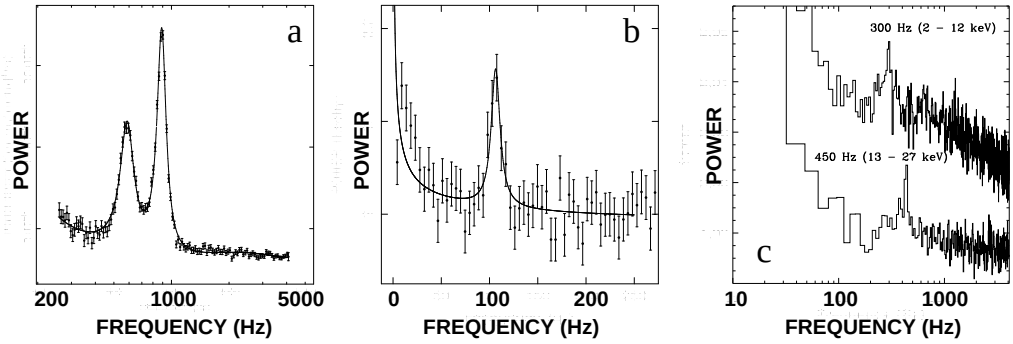

Figure 1.2: (*a*) Twin kilohertz (kHz) QPOs detected in the Z-source Sco X-1, (*b*) hectohertz (hHz) QPOs in the atoll-source 4U 0614+09, (*c*) High Frequency (HF) QPOs in the black hole GRO J1655-40 (van der Klis 2004)

1.5 Timing studies of X-ray binaries

During the past decade, the millisecond time-scales variability seen in the X-ray flux from X-ray binaries (Fig. 1.2) was brought to the attention of the astrophysicists community. X-ray binaries mainly emits in the X-ray band, thus their timing analysis deals with X-ray photons. These sources have either a neutron star or a black hole as compact objects and a companion star with a mass $\leq 1 M_{\odot}$. In sources with a neutron star, its magnetic field is low ($10^8 - 10^9$ G). For this reasons these objects are dubbed Low Mass X-ray Binaries (LMXBs; Frank et al. 2002). Due to the strong gravitational pulling of the compact objects, matter from the companion accretes onto the compact objects and forms an accretion disc around it. During accretion, because of the large temperature, the innerpart of the accretion disc emits thermal X-ray photons. One more class of X-ray binaries are High Mass X-ray Binaries, whose companion star is a massive star. These objects accrete usually via stellar wind and do not show variability on millisecond time-scales. In the following we concentrate on the timing variability in LMXBs.

The Rossi X-ray Timing Explorer satellite (Bradt et al. 1993) has discovered millisecond time-scale modulations in the X-ray flux from LMXBs. This time scale is typical for matter orbiting close to the compact object. Therefore, timing studies of these sources could provide a way to investigate the motion of matter in a strongly curved space-time, thus probing General Relativity in strong field regime. Information about so rapid phenomena are obtained calculating the power spectrum of the photon-time series collected. The peaks seen in the power spectra have a non-zero width, thus they are dubbed Quasi-Periodic Oscillations (QPOs).

1.5.1 What is a QPO?

A QPO is a peak of given width in the Fourier power spectrum. It usually is fitted with a Lorentzian (van der Klis 2004)

$$P_\nu \propto \frac{\Delta\nu}{(\nu-\nu_0)^2+(\Delta\nu/2)^2} \tag{1.1}$$

where ν_0 is the central frequency of the peak, $\Delta\nu$ its Full Width at Half Maximum (FWHM). The FWHM depends on the coherence time of the oscillation $\tau = 1/\pi\Delta\nu$. The quality factor Q of a QPO is

$$Q = \frac{\nu_0}{\Delta\nu}\ , \tag{1.2}$$

which gives a measure of the coherence of the peak. QPOs are modulations in the power spectrum with $Q > 2$, while those with $Q < 2$ are classified as peaked noise.
The amplitude of a QPO is the integrated power of the peak $P = \int P_\nu d\nu$ and it is usually expressed in terms of "root mean square amplitude" (rms; Nowak et al. 1999)

$$rms = \left(\frac{< N^2 > - < N >^2}{< N >^2}\right)^{1/2} \tag{1.3}$$

where N is the count rate (number of photons/s) in the segment of data. The significance of a QPO is given by (van der Klis 1998)

$$n_\sigma = \frac{1}{2} N\ rms^2 \left(\frac{t}{\Delta\nu}\right)^{1/2} \tag{1.4}$$

where t is the integration time ($t \gg 1/\Delta\nu$).

1.5.2 The QPOs morphology

The observed timing variability in LMXBs shows a large dynamic range ($\sim 10^{-3} - 10^3$ Hz). In the past years the attention has been focused on those time-scales typical for the motion of matter close to the compact objects (10^3 Hz). However, studies on the Low Frequency (LF) QPOs have been done as well and showed that they are correlated with the High Frequency (HF) ones (Psaltis et al. 1999). LF QPOs in systems with a neutron star (NS LMXBs) in the range $0.001 - 0.01$ Hz are dubbed *millihertz QPOs*, those with a frequency range from 0.5 Hz to 2 Hz are known as *1Hz QPOs*, *normal/flaring branch oscillations* (N/FBOs) are in the interval $4 - 20\ Hz$

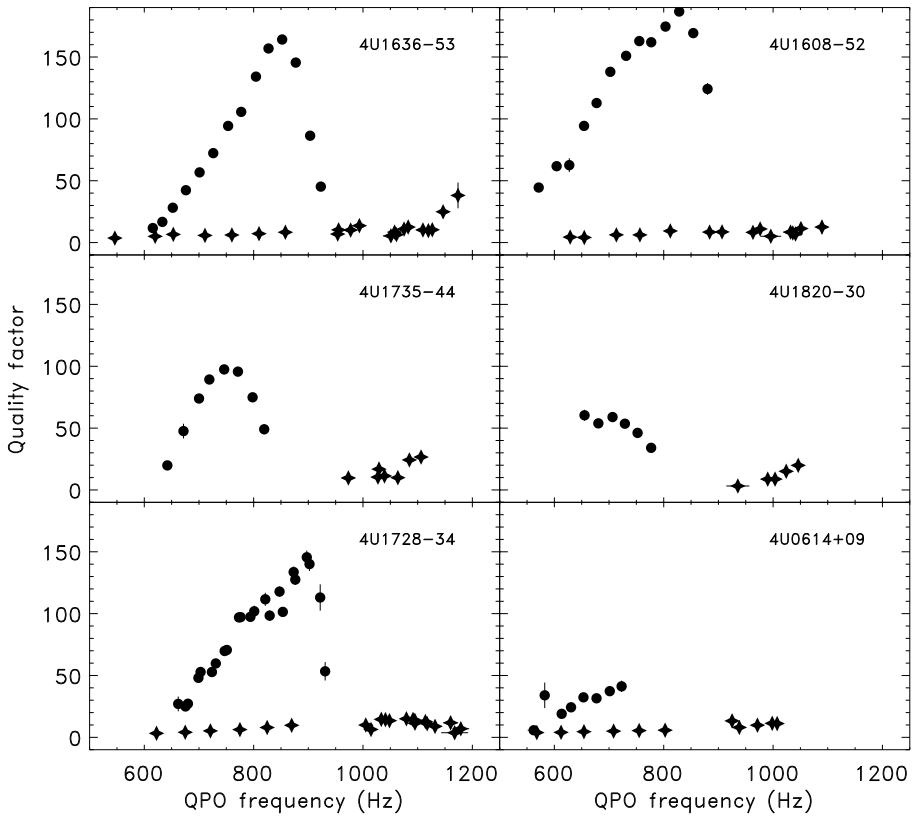

Figure 1.3: Quality factor (coherence) $Q = \nu_0/\Delta\nu$ of both the upper (crosses) and lower peak (dots) versus their central frequencies for several sources with a neutron star (Barret et al. 2006). The lower peak in frequency of the twin peaks is much coherent than the upper one.

and finally $\sim 20 - 60\ Hz$ QPOs are called *horizzontal branch oscillations* (HBOs). The names N/FBOs and HBOs derive from different X-ray state of the source in wich they are detected. Several features with similar properties are seen in systems with a black hole, depending on the spectral state of the source (for a general review see van der Klis 2004).

In systems with a neutron star, beside LF QPOs and HF QPOs, another class of QPOs with frequency around 100-300 Hz is observed. They are called hectoHz (hHz) QPOs. hHz QPOs have central frequencies that do not drift up and down like LF and HF QPOs. For this reason, they are believed to be related to the spin frequency of the neutron star. The spin frquency of some sources has been measured during type I X-ray bursts, i.e. sudden repeated increments of the X-ray luminosity of a factor of 10, followed by a slower

Source	Type	Frequeny (Hz)	$rms(\%)$	$FWHM$ (Hz)
4U 0614+09	Atoll	$400-600$	$6-15$	
		$500-1045$		$\sim 88 \pm 26$
		327		
		$630, 727$	$16.5-15.8$	
4U 1728-34	Atoll	$637-716$	$5.2-6.9$	$8-94$
		$500-1100$	$5.5-8.1$	
Sco X-1	Z	$570-830$	$0.9-1.2$	~ 80
		$870-1130$	$0.6-0.9$	$13-68$
GX 17+2	Z	$470-780$	$3-5$	~ 70
		$645-1087$	$5.7-2.5$	$180-90$

Table 1.1: Frequency range and typical values of both the rms (fractional root mean square) and the $FWHM$ (full width at half maximum) for twin kHz QPOs observed in Z e atoll sources. Z sources are much more brighter than atoll, accreting close to the Eddington limit.

decay (Méndez & Belloni 2007). hHz QPOs are not observed in system with a black hole. Spin frequencies are well measured in Accreting Millisecond Pulsars (AMPs), another class of LMXBs showing both QPOs and a well defined spike at the spin frequency of the neutron star (see Fig. 2.1).

Those QPOs with frequency typical of the orbital motion often show up as a couple: They are called twin peak High Frequency (HF) QPOs (Fig. 1.2; van der Klis et al. 1996). Twin peak HF QPOs have puzzling proprieties. In sources with a black hole they always have the same central frequencies, therefore they are believed to carry imprints of some foundamental physical mechanism (Remillard & McClintock 2006). In sources with a neutron star twin peaks drift in frequency up and down as the spectral state of the source changes (Kaaret et al. 1998). Moreover, in these sources a systematic behaviour of both the power and the coherence of the peaks versus their frequency is clearly observed (Fig. 1.3; Barret et al. 2006). One more remarkable feature is the clustering of the ratio of their central frequencies at $\sim 3:2$ (Fig. 1.4 bottom; e.g. Török et al. 2008). In Table 1.1 we report the main parameters for twin HF QPOs observed in some sources with a neutron star.

1.5.3 Proposed models for the QPOs phenomenon

Several models have been proposed to explain twin peak HF QPOs. The relativistic precession model is based on the orbital motion of test particles

in a curved space-time (see Chapter 6; Stella et al. 1999). Miller et al. (1998) proposed that the twin peaks in NS LMXBs could be produced by beat-frequency mechanisms (Fig. 1.4 top). A clustering of the central frequencies of the twin peaks around a $\sim 3:2$ ratio was claimed by Abramowicz & Kluźniak (2001) as probe of non-linear resonance mechanisms in a strongly curved space-time (Fig. 1.4 bottom). Other models take into account disk-seismology or magnetohydrodynamics waves through the accretion disk (for a general review see van der Klis 2004). Osherovich & Titarchuk (1999) proposed that the origin of twin HF QPOs maybe related to both keplerian oscillations in a rotating reference frame and interaction of the matter with the magnetosphere of the neutron star.
In Chapter 6 we describe in more detail the motion of a test-particle in the Kerr metric, its implications and limits for the modelling of the twin HF QPOs.

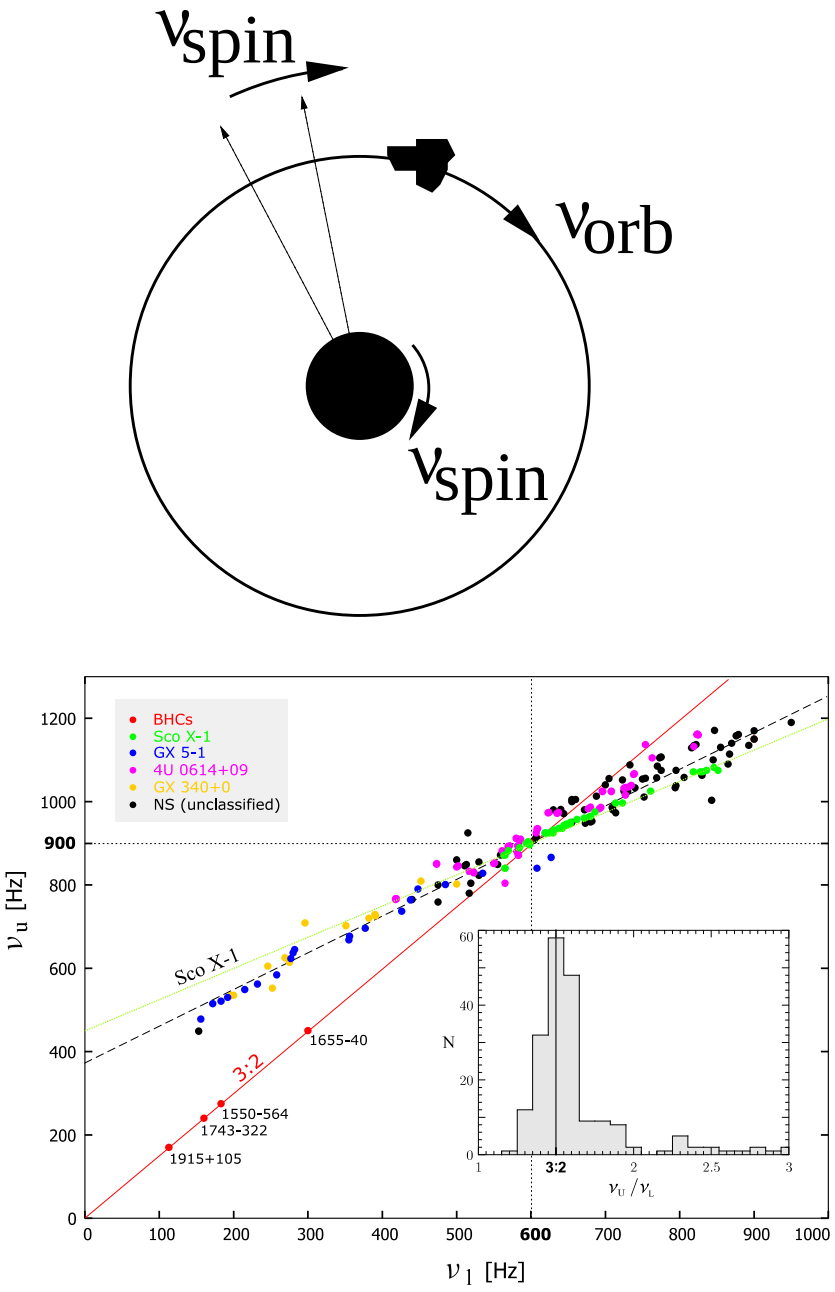

Figure 1.4: *Top*: The beat-frequency model idea for the twin peak kHz QPOs in systems with a neutron stars. A blob of matter orbiting the nutron star at the orbital frequency ν_{orb} beats with the spin frequency of the neutron star ν_{spin} thus producing a modulation at ν_{orb} and one at $\nu_{orb} - \nu_{spin}$ (Miller et al. 1998). *Bottom*: The 3:2 frequency ratio clustering of the twin peaks claimed by the relativistic resonance model (Török et al. 2006)

Chapter 2

Timing analysis techniques

Different techniques are used to study the variability in time of astrophysical sources. The adopted approach depends on the specific problem and variability timescale one is interested in. For bright sources with small underlying noise and for ordinary time-scales (hours), one can look directly at variations of the light curve. However, if the source pulses on much shorter time-scales (typically smaller than 1 sec), then it is hard to disentangle the signal. In these cases Fourier transform techniques are the best approach. The Fourier transform of a signal displays the spectrum of the relavant frequencies in the modulation.

If we want to study in detail the shape of the pulsation, then we have to reconstruct also its profile. By masuring both the amplitude and phase of the many Fourier components of the power spectrum one can express the signal as a Fourier series. For strictly periodic sources of known period we can reconstruct the pulse shape by folding the signal over intervals whose lenght is the period of the pulsation. This method is known as epoch-folding technique. It averages the profile over a number of intervals equal to the number of periods contained in a given observation.

2.1 Fourier analysis

The Fourier analysis is a powerful tool to perform timing studies of rapidly varying signals. It states that any signal can be decomposed into a sum of many sine waves, hence allowing the study of the proprierties of the signal and of the mechanism producing it.

This is particularly useful when dealing with pulsating sources. The goal is to determine the period of the pulsation. If the source is strictly periodic and extremly stable (e.g. pulsars) then the Fourier spectrum will show a spike

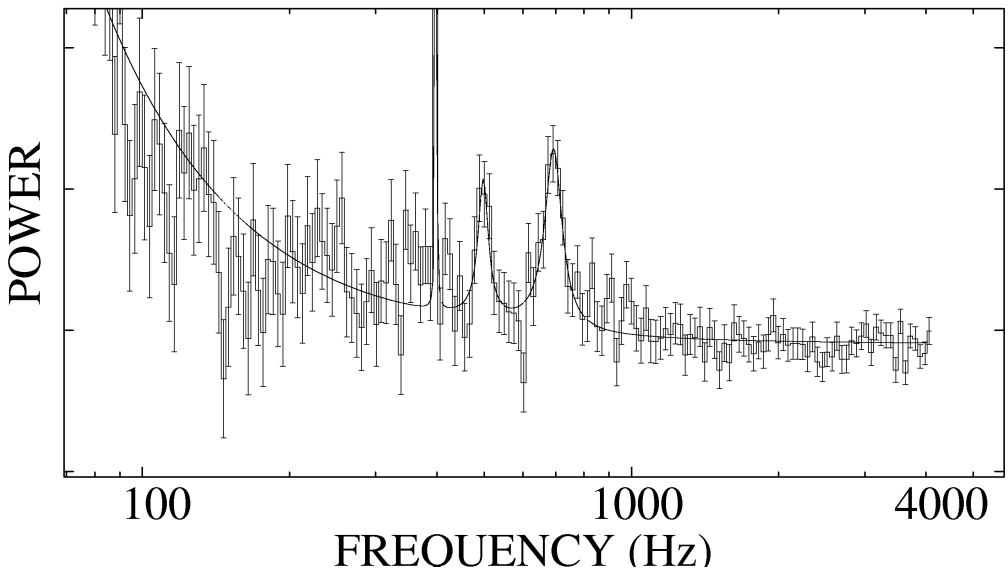

Figure 2.1: Power spectrum from the accreting millisecond pulsar SAXJ1808.4-3658. The broadened peaks are twin kHz QPOs. The pulsation from the rotation of the neutron star at 401 Hz shows up as a spike (Wijnands et al. 2003).

at the rotational frequency of the neutron star. If the signal is not either strictly periodic or stable (e.g. quasi-periodic oscillations in X-ray binaries) broadened peaks are observed (Fig. 2.1).

2.1.1 The Fourier Transform

If the signal $x(t)$ is a continuous function, then the FT decomposes it into an infinite number of sine waves. We can write

$$x(t) = \int_{\infty}^{-\infty} a(\nu) e^{-2\pi\nu i t} d\nu \tag{2.1}$$

$$a(\nu) = \int_{\infty}^{-\infty} x(t) e^{2\pi\nu i t} d\nu \tag{2.2}$$

with $-\infty < t < \infty$, $-\infty < \nu < \infty$; in this case we refer to the continuous FT. The continuous FT does not introduce spurious features in the analysis, i.e. the continuous FT of a sine wave is a delta function. As we will see this is not true for the "discrete" Fourier transform.

Let our signal $x(t)$ be a time series of lenght T divided into N intervals, each of equal width $t_k = kT/N$ and containing a number of photons x_k $(k = 0, ..., N-1)$. Then the Fourier transform a_j is an equidistant discrete

series of step $\delta\nu = 1/T$

$$a_j = \sum_{k=0}^{N-1} x_k e^{2\pi i j k/N} \qquad j = -\frac{N}{2}, ..., \frac{N}{2} - 1 \tag{2.3}$$

$$x_k = \frac{1}{N} \sum_{j=-N/2}^{N/2-1} a_j e^{-2\pi i j k/N} \qquad k = 0, ..., N-1. \tag{2.4}$$

where x_k is the discrete inverse Fourier transform.

The squared modulus of the a_j represents the power spectrum of the signal, it tells us "how much signal" is modulated at the frequency ν_j. Following the normalization by Leahy et al. (1983) the power spectrum is (e.g. see Fig. 2.1)

$$P_j = \frac{2}{N_{ph}} |a_j|^2 \tag{2.5}$$

where N_{ph} is the total number of photons.

2.1.2 Relation between Discrete and Continuous Fourier Transform

We can think to express a discrete time series x_k $(k = 0, ...N-1)$, of finite lenght T, in terms of a continuous and infinite signal $x(t)$ multiplied by a window function

$$w(t) = \begin{cases} 1, & 0 \leq t \leq T \\ 0, & otherwise \end{cases} \tag{2.6}$$

and a delta function

$$i(t) = \sum_{k=-\infty}^{\infty} \delta\left(t - t_k\right). \tag{2.7}$$

Using the convolution theorem, the FT of $y(t) = x(t)w(t)i(t)$ is $b(\nu) = a(\nu) * W(\nu) * I(\nu)$, where $W(\nu)$ and $I(\nu)$ are the Fourier transforms of $w(t)$ and $i(t)$. The FT $W(\nu)$ is a wide peak with some sidelobes. The FT $I(\nu)$ is again a delta function centered at $\nu_j = j/\delta t$. The window function introduces a broadening of the peaks, the sampling function other peaks one usually does not expect, coming from a reflection of the power spectrum with respect to the Nyquist frequency $\nu_{N/2} = N/2T$, a pheomenon know as "aliasing".
Aliasing is overcome by binning the time series into bins of width δt. Indeed binning a time series is like averaging the signal over the bin width. The problems caused by the windowing can be more serious: It can spread the Fourier transoform of a sine wave over the entire spectrum (see M. Van der Klis, Fourier Techniques in X-ray Timing).

2.2 Epoch folding techniques

These techniques are useful for analyzing periodic signals. The method is also used to search for periodicity in a time series. The first step is to guess a period, then the time series is divided into intervals of lenght equal to the period guessed. The values for each periodic point are averaged and plotted as a function of the chosen period, that is, if the test period was six day, the seventh bin is plotted back with the first day's data bin. This is the step known as *epoch folding*, since the different test periods are stacked and averaged over an epoch. An epoch is defined in units of the period chosen, such that an entire period ranges from 0-1 in epoch, or phase. Fig. 2.2 shows the signal collected in Asiago (October 11, 2008, obs 4 in Table 4.1) and binned at 1 s (above) and then the Crab pulsar profile (below) after folding the time series over many periods of the source.

To determine the period a test statistic is applied to the folded light curve and the results of this statistics gives the period. The test statistic applied to the folded data is quite similar to a chi-square test, but the interpretation of the output is different. Instead of looking for the minimum we try to maximize the χ^2 with respect to the average value of the time series (Leahy et al. 1983):

$$\chi^2 = \sum_{i=1}^{N_b} \frac{(x_i - \bar{x})^2}{\sigma_i^2} \tag{2.8}$$

where N_b is the number of bins the time series is divided into, $\bar{x}$ the average value of the signal and σ_i the associated error of the ith bin.
The best period is the one that maximizes the sum (2.8) (Fig. 2.3). This means that, folding over that specific value of the period P, the light curve has a well peaked and defined profile, statistically not consistent with being constant.

2.2.1 Estimating errors: sinusoidal and non-sinusoidal signals

The error on the period from epoch-folding techniques can be estimated following Leahy (1987). Larsson (1996) suggested a different method based on a work by Kovacs (1981). The gaussian frequeny error for a sinusoidal and evenly sampled signal is

$$\sigma_f = \frac{\sqrt{2} a \sigma_{tot}}{\sqrt{N} A T}, \tag{2.9}$$

where σ_{tot} is the standard deviation in the unfolded time series, N the total number of data points, A is the sinusoidal amplitude and T the total time

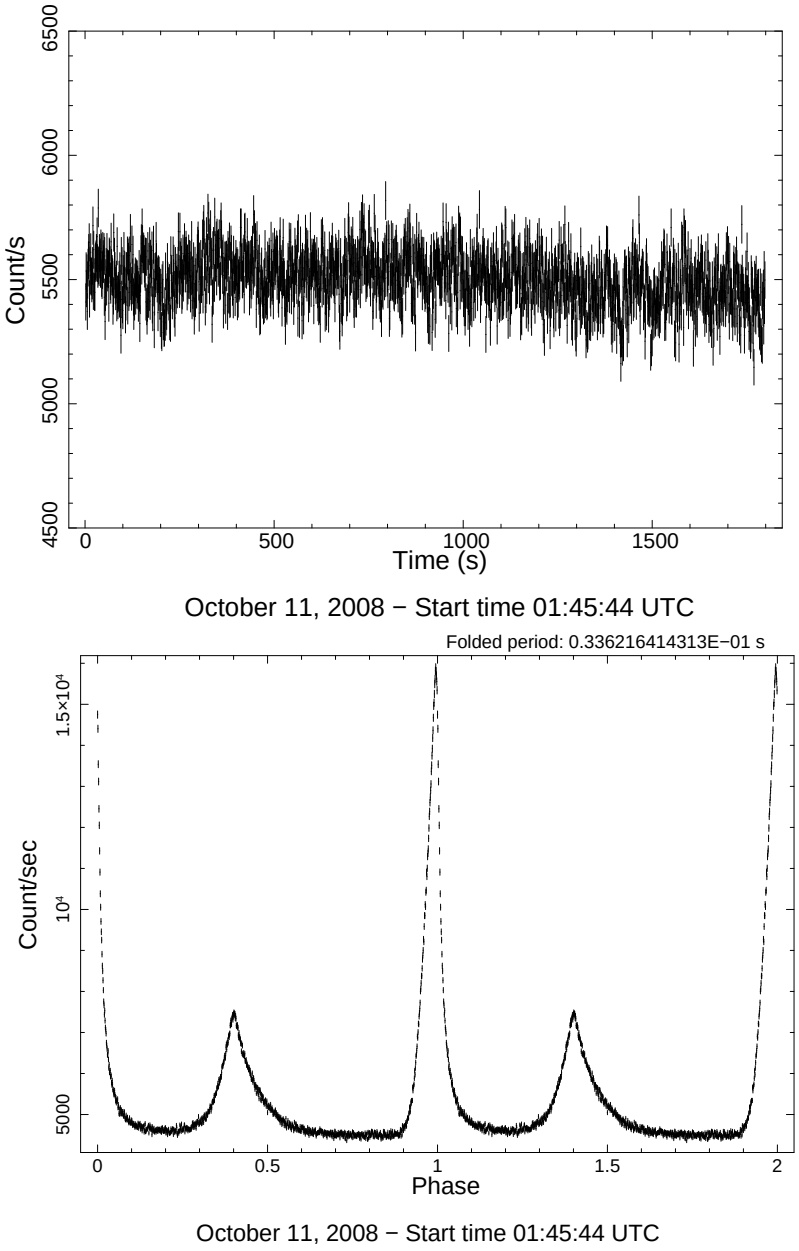

Figure 2.2: *Top*: Time series binned at 1 s as taken by Aqueye from the Crab pulsar. *Bottom*: Folded light curve of time series above. The bin size is 33.6 μs producing 1000 bins for each period of the Crab pulsar (33.6 ms). For clarity two rotation of the Crab pulsar are shown (i.e. phase 0-2.)

lenght for the data. The parameter a was estimated to be $a \approx 0.45$. Following

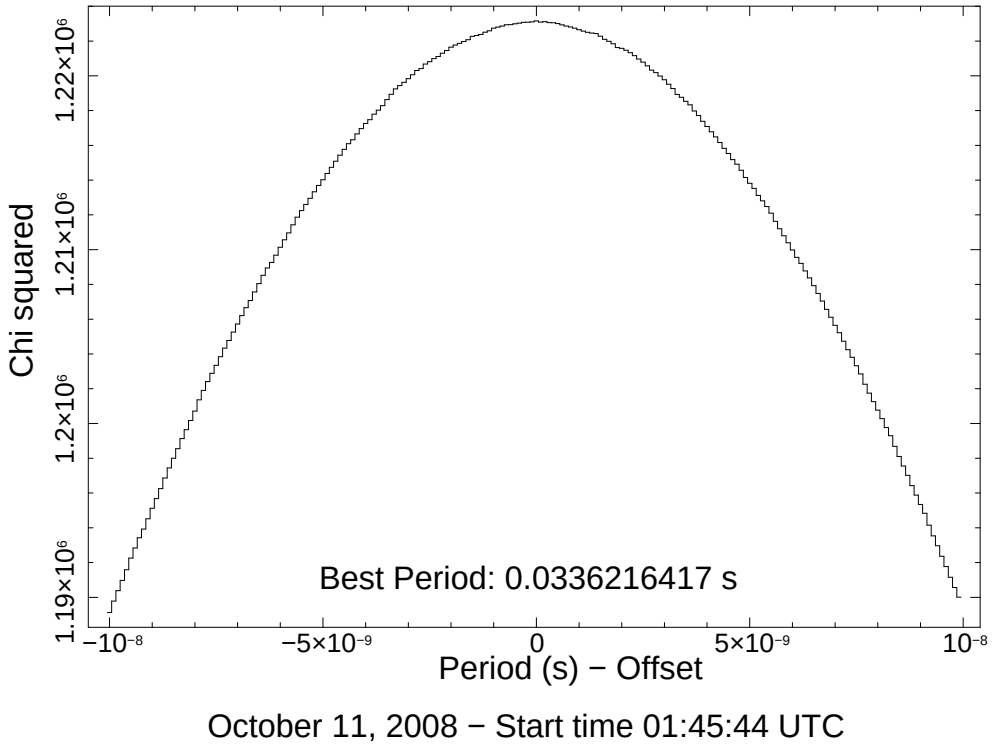

Figure 2.3: χ^2 distribution of the Crab pulsar rotational period. The best estimate of the period is the one that corresponds to the maximum of χ^2. Observation taken in Asiago on October 11, 2008 (obs 4 in Table 4.1).

Larsson (1996) we can arrange (2.9) for the error on the period

$$\sigma_P^2 = \frac{6\sigma_{tot}^2}{\pi N A^2 T^2} P^4 \tag{2.10}$$

where P is the estimated period of the sinusoid.
For a non-simusoidal signal we can write the amplitude A as a weighted sum over the many Fourier components $\nu_k = k\nu_1$ forming the signal. The error on the period is

$$\sigma_P^2 = \frac{6\sigma_{tot}^2}{\pi^2 N T^2} \frac{P^2}{\sum_{k=1}^{m} k^2 A_k^2}, \tag{2.11}$$

thus we need to know the Fourier harmonic contents of the signal. This can be easily calculated performing an iterating fit procedure to the signal: The signal can be written as a sum of sin waves whose amplitudes and phases are determined by the fit.

2.3 Other mathematical tools: cross-correlation, auto-correlation functions

The correlation function can be used to detect non-randomness in the data, to identify an appropriate model for a time series (if the data are not random) or to detect deterministic components masked in a random background because correlation functions of deterministic data (like sine wave) persist over all time displacements, while correlation functions of stocastic processes tend to zero for large time displacement (for 0-mean time series).

If $f(\mathbf{r}, t)$ and $g(\mathbf{r}, t)$ are functions in space and time their cross-correlation is defined as follow

$$f \otimes g = \int f^* (\mathbf{r}, t)\, g (\mathbf{r} + \delta\mathbf{r}, t + \tau)\, dt, \tag{2.12}$$

where $\delta\mathbf{r}$ and τ are spatial and temporal delays, respectively, and $*$ stands for the complex conjugate of f. We may say that the cross-correlation function tells us the degree of "similarity" between two functions, i.e. the *degree of coherence* at two different space-time points.
If $g(\mathbf{r}, t) = f(\mathbf{r}, t)$ we name (2.12) auto-correlation function: The signal is cross-correlated to itself. If $f(t)$ is only a function of time and makes oscillations on a typical time scale $\hat{t}$, then (2.12) describes the degree of correlation as function of a delay τ. The value of τ at which $f(t) \otimes f(t + \tau)$ reaches the minimum is the typical time-scale $\hat{t}$ over which the signal makes oscillations.

Fig. 2.4 (top) shows the autocorrelation of the signal from the Crab as seen by Aqueye on October 11, 2008, 01:45:44. The normalitation is such that the autocorrelation is one at zero delay. The count rate for this observation is $\sim 5000 count/s$ while the source net photon flux is $\sim 1000 - 2000 count/s$ (see Table 4.2). The time resolution (bin time) is $30\mu s$. The figure on the bottom shows a zoom-in the region around the main pulsation, from which we can estimate the width of the beam of light.
It is also interesting to use these concepts to study the nature of the electromagnetic field of a signal (Appendix A).

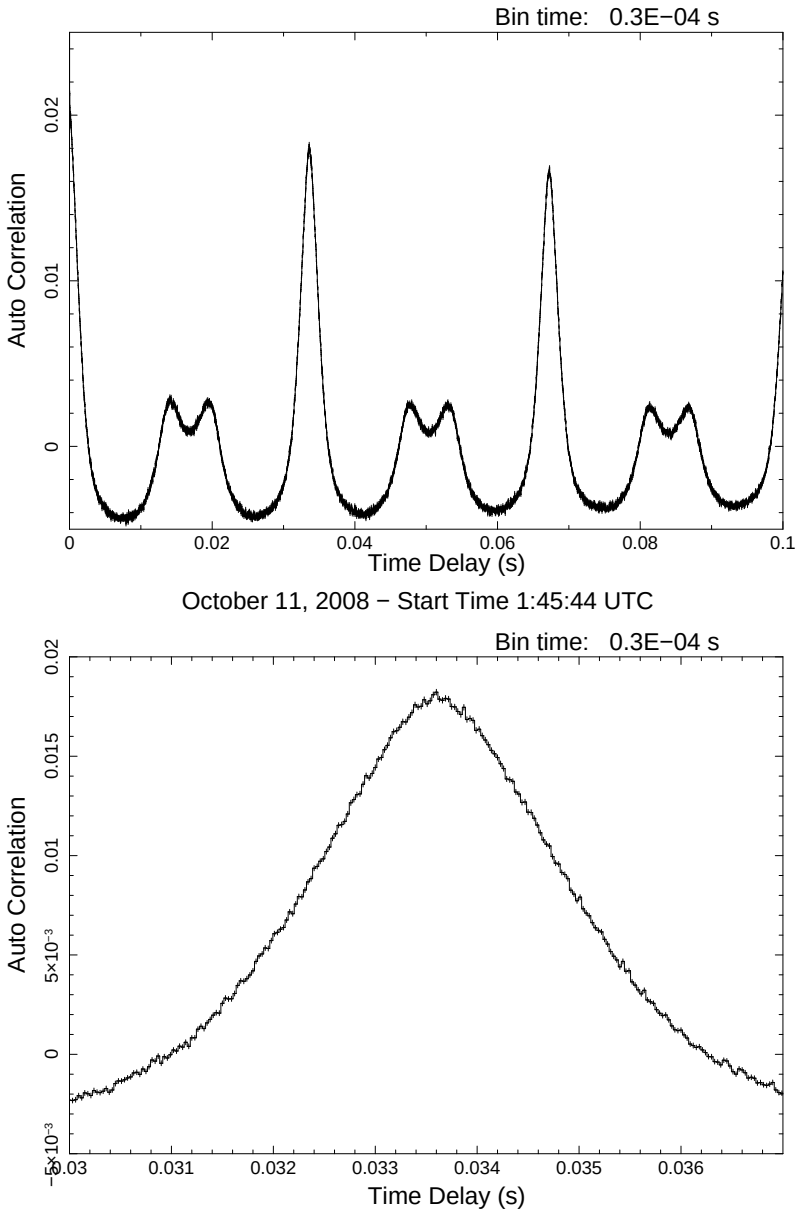

Figure 2.4: *Top*: The autocorrelation of the Crab pulsar signal calculated over intervals 0.3 s long and averaged into one frame. The bin time is $30\mu s$. The characteristic profile is seen. *Bottom*: A zoom-in the region around the main peak, from which we can estimated the width of the beam of light.

Chapter 3

Baricentering and phase-analysis procedure

Studying pulsars requires to time-tag with extreme precision the photons we collect from them. Therefore we must refer the time of arrival of photons (TOAs) to a reference frame that approximates an inertial frame to the level of precision needed. For microsecond precisions it is sufficient to account for both the rotation and revolution of Earth. Therefore it is common to refer TOAs to the solar system baricenter (SSB). The light travel time delay between the position of the observatory and that of SSB is commonly referred to as Roemer delay. To achieve higher time-tagging precisions one should also correct for the deviation of the photon's trajectories due to the presence of massive bodies in the solar system (Shapiro delay), and accounting for the non-uniform time beaten by clocks lying in the gravitational field of the solar system (Einstein delay).

In this chapter we will describe how to apply corrections to the acquired time series. We analyze the barycentric corrected TOAs adopting the tools described in Chapter 2. A more accurate approach, known as phase-analysis in pulsar timing, is described.

3.1 From site to solar system-barycentered TOAs: Tempo2

The photons from the pulsar are collected at the observatory, and we refer to them as site arrival times (SATs). Before performing timing analysis some corrections to the SATs need to be done, i.e. we have to reconstruct the TOAs as detected by an observer in an inertial reference frame. This is meant to clean TOAs by all the effects they carry imprints of, undergone

along the path from the source to the observatory. For instance, for radio frequencies the dispersion measure (DM) due to the interstellar medium is relavant. Its effect is a delay on the TOAs detected, dependending on the frequency of the radiation. Thus one can use pulsars to give an estimate of the DM (e.g. Backer et al. 1993). The proper motion of the pulsar also introduces effects affecting TOAs and needs to be taken into account.
Photons get through our solar system and therefore their trajectories are distorted by the curvature of the space-time due to the presence of massive bodies such as the Sun, Jupiter, Saturn and the other smaller planets. The role of a planet depends on what precision we require: The higher the precision the more relevant smaller planets in describing the curvature of the space-time. The curvature introduces a delay on TOAs known as Shapiro delay.
Precise timing also requires the time beaten by clocks being uniform. In a gravitational field clocks run slower and this effect is also differential, depending on the gravitational potential the clock lies in (Einstein delay).
Therefore we need to model all these effect in order to reconstruct TOAs in an inertial reference frame. One usually refers TOAs to an observer located at the solar system barycenter (SSB) and name them baricenter arrival times (BATs).

Tempo2 (Hobbs et al. 2006a; Edwards et al. 2006) is a software meant to model with exterme precision (up to $\sim$1 ns) TOAs as collected by an inertial observer at SSB. The software is an updated version of its precursor Tempo. In Tempo the precision achieved on TOAs was of $\sim$100 ns. Since pulsar timing has been becoming more and more demanding other phenomena had to be taken into account (polar motion of Earth, Shapiro delays due to gaseous planets and other features listed in Table 2 in Hobbs et al. 2006a).

3.1.1 Site versus solar system-barycentric clocks

In recostructing TOAs in a inertial reference frame we can start discussing the so-called clocks correction chain. One must refer times to a clock running as much uniform as possible. At the observatory the clock against which TOAs are time tagged is an oscillator that, depending on its nature, can not run uniformely for an infinite interval of time. These clocks are usually characterized by an offset and a mean drift that needs to be corrected. As explained in Section 4.7 corrections are performed by means of the GPS time. The Bureau International des Poids et Measures (BIPM) publishes monthly bulletins with the offsets between various clock pairs. Using these bulletins one can tie GPS to UTC time. UTC time is the weighting of data from an ensamble of clocks around the world.

To account for the irregular rotation of Earth UTC is tied to Temps Atomique International (TAI) time by adding an integer number of leap seconds. However due to the gravitational and rotational energy of Earth, clocks on its surface do not run uniformely, therefore the time beaten by atomic clocks need to be tied to the Geocentric Celestial Reference System time (TCG). This is done by constructing a refence of clocks, named Terrestial Time (TT), which differs from TCG by a constant rate such that its unit corresponds to the second in the International System on the surface of the geoid

$$TT(TAI) = TAI + 32.184s \tag{3.1}$$

(for more details Guinot 1988; Petit 2003).

TT time expresses only approximately the proper time experienced by the observer at the observatory. More corrections should be taken into account. Indeed these geoid times are measured against a clock which still suffers the effects of the gravitational field of the solar system bodies. Thus we have now to refer TOAs to the "quasi-inertial" SSB frame.

The observatory and SSB are related by a relativistic 4-dimensional space-time transformation. The spatial part of the event is the distance from the observatory to SSB, altered by a negligible gravitational and special relativistic lenght contraction. The relativistic time-dilation effects however can not be neglected. The Einstein time-dilation integral is (Edwards et al. 2006)

$$\Delta_{\odot-\oplus} = \frac{1}{c^2}\int_{t_0}^{t}\left(U_\oplus + \frac{v_\oplus^2}{2} + \Delta L_C^{(PN)} + \Delta L_C^{(A)}\right)dt. \tag{3.2}$$

where $U_\oplus$ represents the gravitational potential where Earth moves in and $v_\oplus$ the velocity of its center. Its value is discussed in Irwin & Fukushima (1999), who computed it using the DE405 Solar system ephemerides (Standish 1998).

In (3.2) most of the correction comes from the acceleration of Earth during its motion around SSB. Thus (3.2) represents the time-dilation for an observer at the center of the geoid. The first two terms describe the gravitational redshift and the special relativistic time-dilation, respectly, and are those whose contributions are more relavant (with a mean drift of $\sim 1.5\times10^{-8}$ s/s); the third and fourth terms are higher-order relativistic and asteroids corrections ($\Delta L_C^{(PN)} \sim 1.97\times10^{-16}$ s/s and $\Delta L_C^{(A)} \sim 5\times10^{-18}$ s/s; Fukushima 1995).

Finally we have to make one more correction, accounting for the time-dilation and gravitational redshift of the observer on the surface of the Earth with respect to the geocenter. We refer to this quantity as differential gravitational redshift and time-dilation (Edwards et al. 2006)

$$\frac{1}{c^2}\left(\mathbf{s}\cdot\dot{\mathbf{r}}_\oplus + W_0 t_a^{obs}\right). \tag{3.3}$$

Here $\dot{\mathbf{r}}_\oplus$ is the velocity vector of the geocenter with respect to SSB given by the solar system ephemerides; $\mathbf{s}$ is a vector from the observatory to the geocenter, expressed as

$$\mathbf{s} = \mathbf{Q}(t_a^{obs})\mathbf{R}(t_a^{obs})\mathbf{W}(t_a^{obs})s_{ITRS}. \tag{3.4}$$

The matrices $\mathbf{W}$, $\mathbf{R}$ and $\mathbf{Q}$ account for the polar motion, rotation and the motion of Earth spin axis in the International Celestial Reference System (for more details see McCarthy & Luzum 2003; McCarthy & Petit 2004).

In (3.3) W_0 is the gravitational and spin potential of the Earth. Although this potential varies with the observation site and in time, Tempo2 ties the time TT to the SI coordinate time at the geocenter, using as definitive value $W_0 = 6.969\ 290\ 134 \times 10^{-10}c^2$ (Rickman 2001).
Once all transformations are performed, the lenght of the second beaten by the clock is the proper time experienced by an observer in the "quasi"-inertial frame located at SSB.

3.1.2 Getting through the solar system: Roemer and Shapiro delay

In the previous section we have seen how to obtain a uniform running clock in the inertial frame at SSB. A further correction on TOAs to account for the spatial distance between the observatory and SSB has to be done. Indeed photons are collected at the observatory and since we want to know the TOAs as detected by the inertial observer at SSB we should know the light travel time from the observatory to SSB. The Roemer delay is the vacuum delay between the arrival of the pulse at the observatory and SSB:

$$\Delta_{R\odot} = -\frac{\mathbf{r}\cdot\hat{\mathbf{R}}}{c}, \tag{3.5}$$

where $\mathbf{r} = \mathbf{r}_\oplus + \mathbf{s}$ is a vector from the observatory to SSB and it is constructed in two steps: $\mathbf{r}_\oplus$ is given by the planetary ephemerides, and $\mathbf{s}$ is given in (3.4). The vector $\hat{\mathbf{R}} \equiv \mathbf{R}/|\mathbf{R}|$ is a unit vector in the direction of the pulsar at the time of observation. $\hat{\mathbf{R}}$ is expressed in term of right ascension (α) and declination (β), the Cartesian components of the proper motion of the source in the plane of the sky (μ_α, μ_δ) and along the line of sight ($\mu_{||}$) (see Edwards et al. 2006). Expanding (3.5) one gets

$$\mathbf{r}\cdot\hat{\mathbf{R}} = r_{||} + \frac{\mathbf{k}_\perp\cdot\mathbf{r}_\perp}{|\mathbf{R}_0|} - \frac{r_{||}\,|\mathbf{k}_\perp|^2}{2\,|\mathbf{R}_0|^2} - \frac{k_{||}\mathbf{k}_\perp\cdot\mathbf{r}_\perp}{|\mathbf{R}_0|^2} \tag{3.6}$$

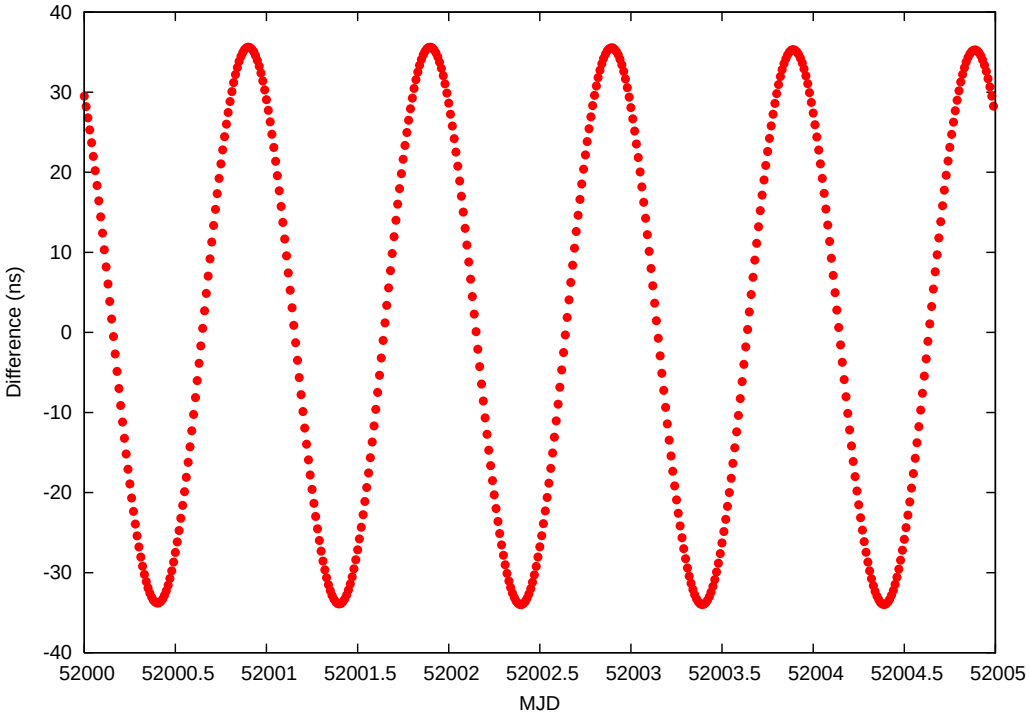

Figure 3.1: Difference of the Roemer delay as calculated by Tempo2 and Tempo for a set of simulated TOAs at the Asiago Cima Ekar observatory. The Earth diurnal oscillation is clearly seen. The amplitude reflects the effects due to the polar motion of Earth and to a different nutation-precession model used by Tempo2 (see text). Both the amplitude and shape of this figure testify the correct setup of our software (see Hobbs et al. 2006a).

here $\mathbf{k}_{||/\perp} \equiv \mu_{||/\perp} |\mathbf{R}_0| \left(t_a^P - t_{pos}\right)$; t_a^P is the time of arrival at the pulsar at a given position with respect to the baricentric at the epoch t_{pos}. In principle t_a^P can not be calculated without knowing the Roemer delay (3.5) itself; this is resolved by iteration procedures (see Edwards et al. 2006).
Equation (3.6) consists of four terms: the initial direction, the proper motion, a correction to unit length after the addition of the proper motion and its acelaretion or deceleration.

As already mentioned in Section 3.1 Tempo2 calculates the Roemer delay taking into account the polar motion of Earth (motion of the rotation axes relative to the crust). Since Tempo does not account for it this difference provides a way to check the Tempo2 installation setup. Indeed we can run Tempo2 in the "Tempo emulation mode" and calculate the Roemer delay. Taking the difference between the Roemer delays we can check whether the behaviour is as expected.
Not accounting for the polar motion gives the coordinates of the observatory

off the corrected values. The worst case resulting by a positional error $\delta\theta$, corresponding to $\delta\theta R_{\oplus}/c$, in timing is

$$\frac{\delta t}{1ns} \sim \frac{\delta\theta}{9.7mas} \tag{3.7}$$

The polar motion has three major components. A free oscillation with period about 435 days (Chandler wobble) and an annual oscillation forced by the seasonal displacement of air and water masses, beating with each other. For these reasons the position on the geoid of the mean pole can differ from the true pole by an amount up to ±300mas and the observatory will result off a few meters the real position. From equation (3.7) this will give an error in timing of $\sim \pm 30$ ns. Therefore the Roemer delay difference as calculated by Tempo and Tempo2 should show a diurnal oscillation signature with an amplitude of $\sim \pm 30$ns, drawn by the rotation of Earth.

Fig 3.1 shows the difference of the Romer delay between Tempo2 and Tempo for a set of simulated TOAs at the Asiago observatory. The amplitude of the oscillation is ∼35ns and it shows the typical diurnal oscillation. The amplitude also includes the contribution due to the out of date precession-nutation model used by Tempo (∼5 ns). The behaviour in Fig. 3.1 can be compared to that in Hobbs et al. (2006a, Fig. 4 left) and testifies the correct setup of the software.

One final important correction to account for is the delay caused by the curvature of the space-time due to massive bodies in the solar system (Shapiro delay). Tempo2 corrects for it taking into account the gravitational potential of the Sun, Venus and gaseous planets (Jupiter, Saturn, Uranus and Neptune). The Shapiro delay is expressed as

$$\Delta_{S\odot} = -2\sum_{j} \frac{Gm_j}{c^3} ln\,|r_j|\,(1-\cos\psi_j) + \Delta_{S\odot 2} \tag{3.8}$$

where m_j and r_j are the mass and the position, with respect to SSB, of the jth planet. ψ_j is the pulsar-telescope-object angle of the jth planet. The term $\Delta_{S\odot 2}$ is a second-order correction for the Sun, mostly accounting for the geometrical excess path lenght due to gravitational bending (Richter & Matzner 1983).

3.2 Rotational period from epoch folding techniques

Once TOAs are referred to the inertial observer at SSB we can analyze them. In this section we apply to the baricentric corrected time series (BATs) the

Table 3.1: Rotational period of the Crab pulsar measured by Aqueye in 2008 (see Table 5.1).

	MJD[a]	Period (s)
1	54749.99287724855327	0.0336216381
2	54750.00668638351852	0.0336216389
3	54750.04505792216435	0.0336216406
4	54750.07656540930556	0.0336216417
5	54750.10252841002315	0.0336216430
6	54750.14465028032407	0.0336216444
7	54750.97900758696759	0.0336216746
8	54751.97132990998842	0.0336217110

[a] Corrected MJD at the solar system barycenter (Tempo1 mode).

method to search for periodicities, already described in Section 2.2. To this purpose we adopted the task $efsearch$ in the timing analysis package Xronos[1] v. 5.21, distributed by the NASA's High Energy Astrophysics Science Archive Research Center.

The BATs are first saved into a FITS file and then loaded in the software. We searched for periodicities by folding the data over a range of periods and by looking for a maximun chi-square as a function of period (see Sec 2.2). We binned the data using 1000 bins per period and a resolution between contiguous periods in the search of 10^{-10} s. As an example Table 3.1 shows the rotational periods measured in this way for the Asiago observations of the Crab pulsar taken in October 2008. The start time is the GPS integer second, accurate to better than approximately +/-30 nanoseconds.
Fig. 2.3 shows the results of the epoch-folding analysis for observation 4. The average period of the Crab pulsar during the observation is $P_{Aqueye} = 0.0336216417$ s. For comparison, the period at the beginning of the observation, obtained interpolating the Jodrell Bank Crab ephemerides, is $P_{JB} = 0.0336216414$ s, 0.3 ns longer. Since Aqueye is sensitive to the spin down of the neutron star already over observations 20m long (~ 0.5 ns), we should compare the Aqueye-rotational period with that in the radio calculated at mid observation. If we do so then the radio period at mid observation is $P_{JB} = 0.0336216418$, within 0.1 ns P_{Aqueye}.

[1] http://xronos.gsfc.nasa.gov/

The expected statistical error σ_P on the period has been estimated using equation (2.11) (Larsson 1996), which takes into account the knowledge of the harmonic content of the pulse shape. In order to compute it we need to calculate the amplitude of each component in the Fourier series of the signal. We performed a χ^2 fit of the observed folded light curve of the Crab (see Fig. 4.2) to that written numerically as sum of many Fourier components. Once determined the amplitude of the Fourier components of the signal (see Fig. 4.1 bottom) we find $\sigma_P \simeq 120$ picoseconds. Therefore the rotational periods in Table 3.1 are in agreement within the statistical error to those from Jodrell Bank radio ephemerides calculated at mid observation (for a more suitable technique to estimate high-accuracy rotational periods see Section 3.3 and Chapter 4).

3.3 Period and period derivative from phase-analysis

The period derivative of the Crab pulsar is about 1.5ns/h. The accuracy achieved with our instrument already on a 20m long observation is $<$ 1ns, comparable to the change of the rotational period induced by the pulsar spin down. Therefore, epoch folding techniques are not suitable for high accuracy instruments. The method here described is used in pulsar astronomy to study the main aspects of pulsars. It consistes in determing the phase of a specific features of the light curve of the source and studying how its phase changes in time. For the Crab pulsar the reference point is the main peak of the folded light curve. The timing model for pulsars states that the phase of the source changes as follows:

$$\phi(t) = \phi_0 + \nu(t - t_0) + \frac{1}{2}\dot{\nu}(t - t_0)^2 + \frac{1}{6}\ddot{\nu}(t - t_0)^3 \tag{3.9}$$

where $\nu, \dot{\nu}$ and $\ddot{\nu}$ are the rotational frequency, its first and second derivative. Therefore from the behaviour of the observed phase one can estimate the rotational period and its derivatives. Moreover the residuals left out after fitting this model provide a way for studying unknown features of the source. For instance this method led to the discovery of the first extrasolar planetary system (Wolszczan & Frail 1992; Wolszczan 1994; Konacki & Wolszczan 2003).

The specific implementation of the analysis adopted here follows from the one developed by A. Čadež, (2008, Harrison project report).
To calculate the phase an analytical approximation of the pulse shape $S(\phi)$ is

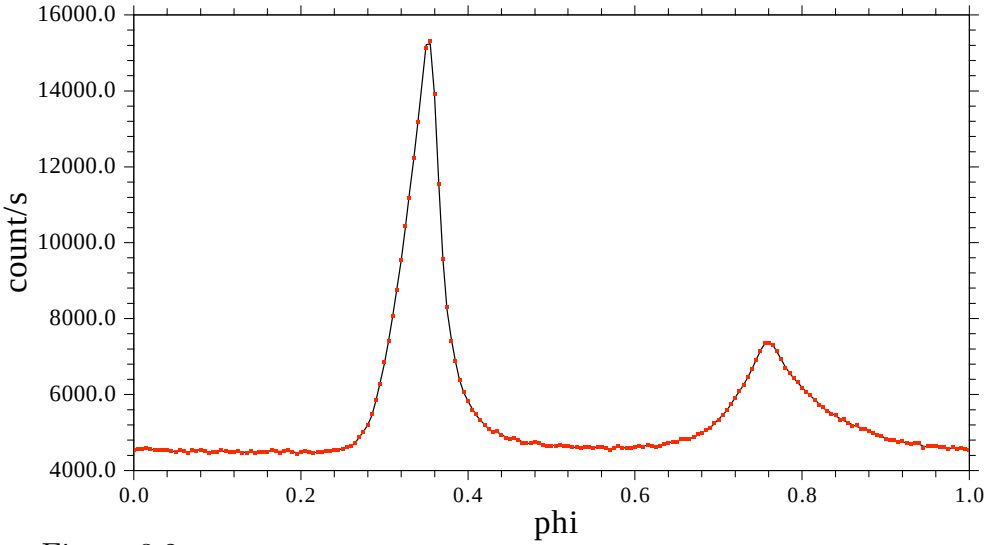

Figure 3.2: The analytic pulse shape (black) and the average pulse shape obtained from the folding of the data (red points).

constructed (Fig. 3.2), such that $S(\phi)$ is a continuous, periodic and differentiable function everywhere expect two points (Čadež 2008, Harrison project report). These two points correspond to the main and interpulse peak of the Crab pulsar. The phase $\psi(t)$ is defined by means of the following phase function $\mathbf{\Psi}(t,\psi)$

$$\mathbf{\Psi}(t,\psi) = \int_{t_0-P_{ini}N}^{t_0+P_{ini}N} \mathbf{P}(\phi(t))S'(\frac{t}{P_{ini}}+\psi)dt \tag{3.10}$$

where $\mathbf{P}(\phi(t))$ is the actual pulsar signal, N is an integer, P_{ini} an approximate rotational period for the observation determined by means of, for instance, Xronos or read directly from the Jodrell Bank radio ephemeris archive. S' is the derivative of the analytical profile S and it is used as template to calculate the phase of the mean peak of the Crab by means of a phase-cross-correlation of S' with the actual signal from the source $\mathbf{P}(\phi(t))$ (Fig. 3.3, 3.4).
Following the standard pulsar slow down model, the pulsar phase can be written as $\phi(t) = \psi_0 + \frac{t}{P} - \frac{1}{2}\dot{P}(\frac{t}{P})^2 + ...$ where P is the actual rotational period of the pulsar. That is, for no too long baseline (few days) we may say that the phase evolution from a reference phase ψ_0 is dictated by both the frequency $1/P$ of the pulsar and its first derivative $\dot{P}/P^2$. Since we choose P_{ini} such that $(P - P_{ini}) \ll 1$ the pulsar signal and the template does not change over the time interval $[t_0 - P_{ini}N, t_0 + P_{ini}N]$. What we want is the phase of the main peak as function of the time t_0 representing the middle

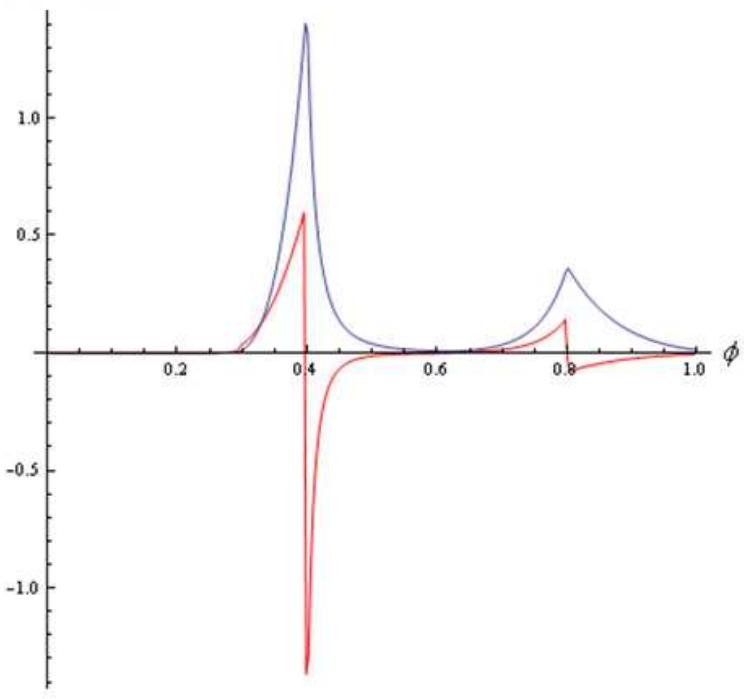

Figure 3.3: The analytic approximation for the pulse profile $S(\phi)$ (blue) and its derivative $S'(\phi)$ (red), used as a template in determining the average phase (by A. Čadež).

point of intervals n seconds long. The pulsar signal $\mathbf{P}(\phi(t))$ is averaged over such time intervals and then it is cross-correlated with the template S'. So, introducing $u = (t - t_0)/P_{ini}$, the phase function can be written as:

$$\begin{aligned}\mathbf{\Psi}(t_0, \psi) &= \int_{-N}^{N} \mathbf{P}\left(\psi_0 + \frac{t_0}{P} - \frac{1}{2}\dot{P}\left(\frac{t_0}{P}\right)^2 + u + \left(\frac{P_{ini}}{P} - 1 - \dot{P}\frac{P_{in}t_0}{P^2}\right)u + \right. \\ &\left. -\frac{1}{2}\dot{P}\left(\frac{P_{ini}}{P}\right)^2 u^2\right) S'\left(u + \frac{t_0}{P_{ini}} + \psi\right) du. \end{aligned} \tag{3.11}$$

The last two terms in the argument $\mathbf{P}$ are very small on the interval of integration. We choose ψ such that

$$\psi + \frac{t_0}{P_{ini}} = \phi(t_0) + \epsilon = \psi_0 + \frac{t_0}{P} - \frac{1}{2}\dot{P}\left(\frac{t_0}{P}\right)^2 + \epsilon \tag{3.12}$$

i.e. the phase of the pulsar at t_0 and that of the template (Fig. 3.3) at the same time differ by ϵ. When performing the cross-corrlation with respect to

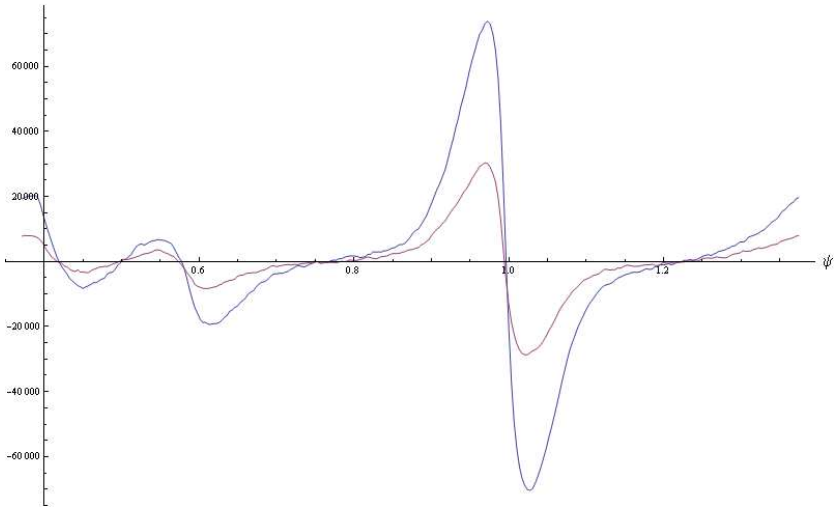

Figure 3.4: The correlation function $\mathbf{\Psi}(t_0, \psi)$ of the template with two sets of Ljubljana data taken in Oct. 11, 2008. The phase of zero crossing is ψ_0= 0.99 (by A. Čadež).

ψ, for each t_0, then ϵ gets $\epsilon \ll 1$, thus the integrand in the phase function can be expanded into a Taylor series and the phase function $\mathbf{\Psi}(t_0, \psi)$ can be written as:

$$\begin{aligned}
\mathbf{\Psi}\left(t_0, \psi\right) &= \int_{-N}^{N} \left(\left(\mathbf{P}\left(u + \frac{t_0}{P_{ini}} + \psi \right) + \epsilon + \left(\frac{P_{ini}}{P} - 1 - \dot{P}\frac{P_{ini} t_0}{P^2} \right) u + \right. \right. \\
&\quad \left. \left. -\frac{1}{2}\dot{P}\left(\frac{P_{ini}}{P}\right)^2 u^2 \right) S'\left(u + \frac{t_0}{P_{ini}} + \psi \right) \right) du \\
&= \epsilon \int_{-N}^{N} S'\left(u + \frac{t_0}{P_{ini}} + \psi \right) du + \\
&\quad -\frac{1}{2}\dot{P}\left(\frac{P_{ini}}{P}\right)^2 \int_{-N}^{N} u^2 S'\left(u + \frac{t_0}{P_{ini}} + \psi \right) du. \qquad (3.13)
\end{aligned}$$

The last line is arrived at by noting that $\int_{-N}^{N} S(x)S'(x)dx = \frac{1}{2}\int_{-N}^{N} \frac{d}{dx}S^2(x)dx$, and it vanishes since the integral is over an integer number of periods. We would remind that the analytical signal $S \equiv \mathbf{P}$, where $\mathbf{P}$ is the actual signal from the pulsar. The integral with the u term in the integrand also vanishes, because the rest of the integrand has even parity. Furthemore, the last integral is also negligible for not too large N, so what finally remains is only the first integral, which is a positive constant, multiplied by ϵ, i.e.:

$$\mathbf{\Psi}(t_0, \psi) \rightarrow \left(\psi + \frac{t_0}{P_{in}} - \phi(t_0) \right) \int_{-N}^{N} S'(u + \frac{t_0}{P_{ini}} + \psi) du \qquad (3.14)$$

S' has two discontinuities at the main and interpulse peak and under the condition of (3.14) the template is aligned with the pulse profile (e.g. Fig. 3.3), thus the phase of the pulsar is determined by the value $\psi_1(t)$ of the steepest zero crossing the phase function $\mathbf{\Psi}(t_0, \psi_1) = 0$ (Fig. 3.4). Since P_{ini} is very near the correct pulsar period, $\psi_1(t)$ changes with time very slowly.

To calculate the phase $\psi_1(t)$ we assumed a starting frequency $\nu_{ini} = 1/P_{ini}$ which is not exactly equal to the true one ν_0. The true frequency decreases as:

$$\nu = \nu_0 + \dot{\nu}_0 \cdot t + \frac{1}{2}\ddot{\nu}_0 \cdot t^2 \tag{3.15}$$

Taking the integral over the time, the true phase of the source is

$$\phi(t) = \nu_0 \cdot t + \frac{1}{2}\dot{\nu}_0 \cdot t^2 + \frac{1}{6}\ddot{\nu}_0 \cdot t^3. \tag{3.16}$$

We calculated a phase $\psi_1(t)$ evolving as the folllowing

$$\psi_1(t) = (\nu_0 - \nu_{ini}) \cdot t + \frac{1}{2}\dot{\nu}_0 \cdot t^2 + \frac{1}{6}\ddot{\nu}_0 \cdot t^3. \tag{3.17}$$

As $\ddot{\nu}_0$ is very small, the behavior of $\psi_1(t)$ over the data set is expected to be well approximated by a parabola.

Chapter 4

Asiago observations

The team from the Univeristy of Padova led by Prof. Cesare Barbieri and Prof. Giampiero Naletto observed the Crab pulsar with the extremely fast optical photon-counters Aqueye. Aqueye is a prototype mounted at the 182cm Copernico telescope of Cima Ekar in Asiago. An indipendent prototype of very fast photometer with a similar technology was built at the University of Ljubljana by the research group led by Prof. Andrej Čadež.
Synchronized observations of the Crab pulsar between Asiago and the observatory of Ljubljana were pursued. The goal of these joint observations was to show how well we can synchronize the phase of the Crab as seen by two such prototypes at different locations.

The phase-analysis procedure described in the previous chapter was applied to the data collected by Aqueye from the Crab pulsar. The data show a high quality such that we were able to determine the pulsar first-order slow down over a baseline of only 2 days.
We compared our measurements to the radio ones reported in the archive of the Jodrell Bank Observatory. The instrumet is able to account for the 0.5 ns rotational period discrepancy due to the different time beaten by iniertial and non-inertial clocks in the gravitational field of the Solar system.
A discussion on a further 0.4 ns discrepancy due to poor estimates of the Roemer delay is also given.

4.1 Aqueye: The Asiago Quantum Eye

Aqueye is mounted at the 182cm Copernico telescope in Asiago, cima Ekar, on the focal plane of the imaging spectrograph AFOSC, which is used as focal reducer. The Aqueye team have obtained observations in several runs from

June 2007 to October 2008, which have permitted to optimize the hardware and software, but also to obtain significant data on the Crab pulsar (Germanà et al. 2011, in preparation), on several rapidly variable stars, on diffuse nebulae with forbidden spectral lines.

The design of Aqueye follows that of QuantEYE (the Quantum EYE; Dravins et al. 2005; Barbieri et al. 2008), an instrument specifically tailored for studying rapid optical variability of astrophysical sources with the ESO E-ELT down to the quantum limit. It can record and store the arrival time of each single photon with a final precision of 500ps for a 1 hour long observing session. Here we shortly describe the opto-mechanical design and the acquisition system of the instrument. For further details see Barbieri et al. (2008, 2009).

The entrance aperture captures a field of view of 3 arcsec. Inside the instrument the light beam crosses a focal reducer and is then split in 4 symmetrical arms by a pyramidal mirror. In each arm, filters and polarizers can be inserted in a collimated portion of the beam. The beam is then refocussed on four SPADs (single photon avalanche photodiodes, produced by the Micro Photon Devices, Italy), that have a diameter of 50 μm, quantum efficiency in the visible band higher than 50%, dead time of 75 nanoseconds, and time-tagging capability better than 50 picoseconds. Every channel can be analyzed independently. The advantage of this design is to partly recover dead time effects in each SPAD, to increase the sustainable count rate, and to allow cross-correlations among the different sub-pupils.

Each signal from the SPADs is timetagged by a Time to Digital Converter (TDC) board (produced by Costruzioni Apparecchiature Elettroniche Nucleari, Italy), that makes use of an external Rubidium clock and a GPS unit for checking the long time stability of the clock. The TDC tags each event with a resolution of 24.4 ps per channel and transfers all the data to an external computer through an optical fiber, where the data are stored.

4.2 The Asiago Cima Ekar campaign

Observations at the Cima Ekar observatory started at the end of 2007 and were pursued by the Aqueye team led by Prof. Cesare Barbieri and Prof. Giampiero Naletto. As usual when dealing with prototypes, many technical problemes arise and need to be solved. A problem the instrument ran into displayed jumps in the phase of the main peak of the pulsar. This problem dealt with the acquisition system and was then solved. The first working run with good seeing conditions, was that performed at October 2008.

Table 4.1 shows the log of these observations. They span over two days and

Table 4.1: Log of the October 2008 observations of the Crab pulsar performed with Aqueye mounted at the 182cm Copernico telescope in Asiago. The start time of the observations is the GPS integer second, accurate to better than approximately +/-30 nanoseconds.

	Starting time (UTC)	MJD[a]	Duration (s)
1	October 10, 23:45:14	54749.99287724855327	1078
2	October 11, 00:05:07	54750.00668638351852	1197
3	October 11, 01:00:22	54750.04505792216435	1797
4	October 11, 01:45:44	54750.07656540930556	1797
5	October 11, 02:23:07	54750.10252841002315	1631
6	October 11, 03:23:46	54750.14465028032407	1197
7	October 11, 23:25:08	54750.97900758696759	3597
8	October 12, 23:13:57	54751.97132990998842	3998

[a] Corrected MJD at the solar system barycenter (Tempo1 mode).

have different durations. Fig. 4.1 (top) shows the count rate for the time series of observation 4 in Table 4.1. As can be seen the average count rate is 5000 count/s and includes photons collected from the background and from the nebula surronding the pulsar. The other observations show a similar average count rate.
Fig. 4.1 (bottom) shows the power spectrum for the same observation. It shows a well known pattern with the fundamental harmonic ∼29 Hz. At least other 20 harmonics are recognizable. The power spectrum was calculated by binning the time series in 200 μs. The binned time series was then divided into segments 1 second long. For each of them the power spectrum is calculated and then all of them are averaged into one. The average is meant to increase the signal-to-noise ratio. However, with such a high photon flux, it is not relevant to average power spectra into one. In order to check this, after barycentering (Chapter 3) we can construct the folded light curve of the source and fitting it to a sum of several Fourier components (Fig. 4.2). By means of an iterative chi-square fitting procedure, we determine the amplitude and the phase of each Fourier components. We fitted both the profile obtained by folding the light curve over the entire time series and the profile obtained averaging the pulse shape over several 1 minute long intervals. The binning time is 33μs. Table 4.2 shows the amplitude (count/s) of the first

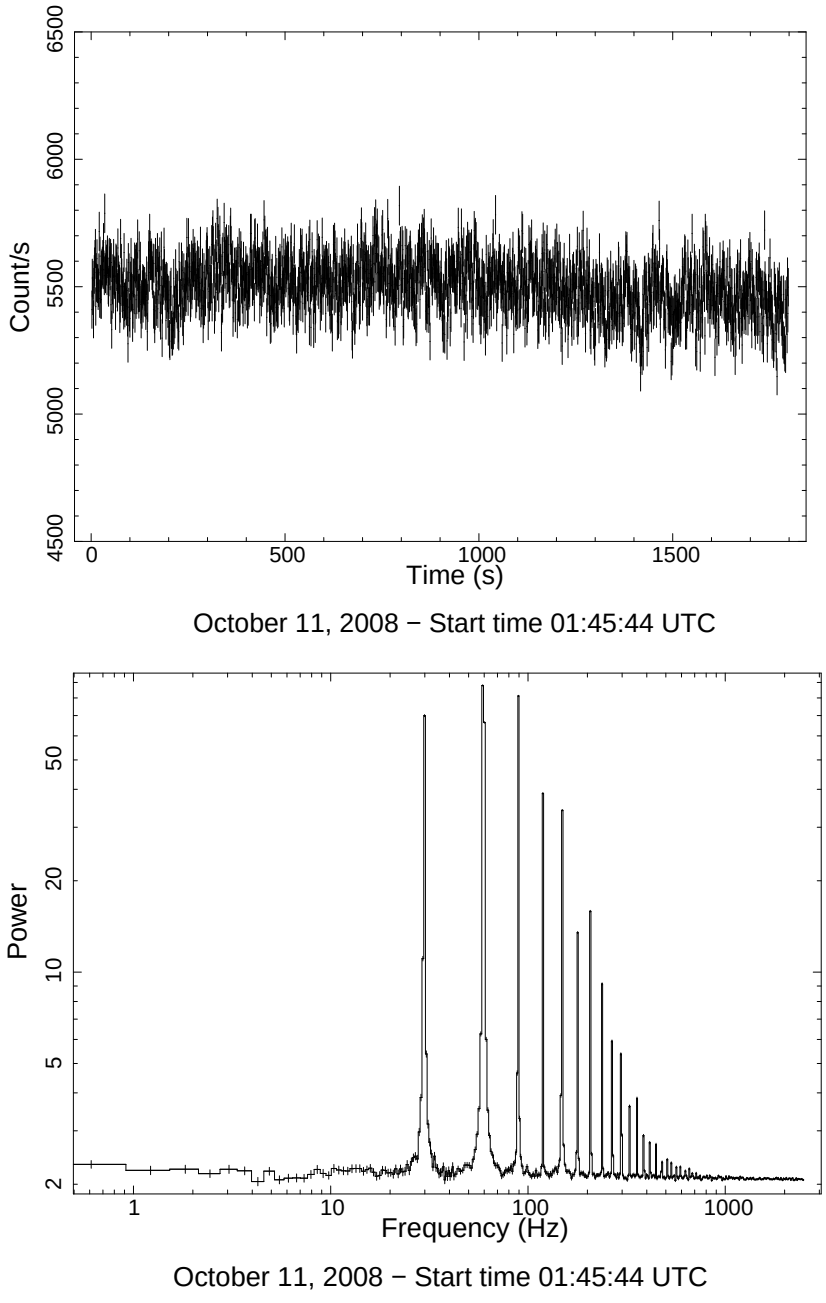

Figure 4.1: *Top*: Light curve (binned at 1 s) of the Crab pulsar obtained with Aqueye. The observation was performed on 11 October 2008, starting at 01:45:44 UTC (observation 4 in Table 4.1). *Bottom*: Power spectrum of the signal from the Crab pulsar as seen by Aqueye (observation 4). The binning time is 2×10^{-4} s. The typical harmonic content of the signal is visible.

Table 4.2: Amplitude of the (first and last five) harmonics of the Crab obtained fitting the folded light curve (see text for details). The amplitudes in the 2nd and 3rd column refer to two different folding procedures. The $\chi^2 \sim 1$ after fitting 50 harmonics.

Harmonic	Count/s[a]	Count/s[b]
Foundamental	761.2	752.9
2th	1492	1476.7
3nd	1064	1053
4rd	861	852
5th	973	963
46th	17.16	16.97
47th	17.87	17.68
48th	17.66	17.48
49th	16.07	15.90
50th	18.77	18.57

[a] Number of photons per second from the non-averaged power spectrum.

[b] As *a* after averaging 27 power spectra calculated over 1 minute long segments.

and last 5 Fouriers components. We see that differences are of the order of $\sim$1%.
The calculations shown in this section were used to estimate the statistical error associated with epoch folding techniques (see Section 2.2.1 and 3.2).

4.3 The radio phase of the Crab pulsar from the Jodrell Bank radio ephemerides archive

In order to test our instruments, we have to compare the phase of the Crab pulsar measured by Aqueye/Iqueye with that reported in the Jodrell Bank Crab radio ephemerides archive[1] (Lyne et al. 1993). Following the standard pulsar slow down model the behaviour of the phase of the pulsar is described by

$$\phi(t) = \phi_0 + \nu(t - t_0) + \frac{1}{2}\dot{\nu}(t - t_0)^2 + \frac{1}{6}\ddot{\nu}(t - t_0)^3 \qquad (4.1)$$

[1] http://www.jb.man.ac.uk/ pulsar/crab.html

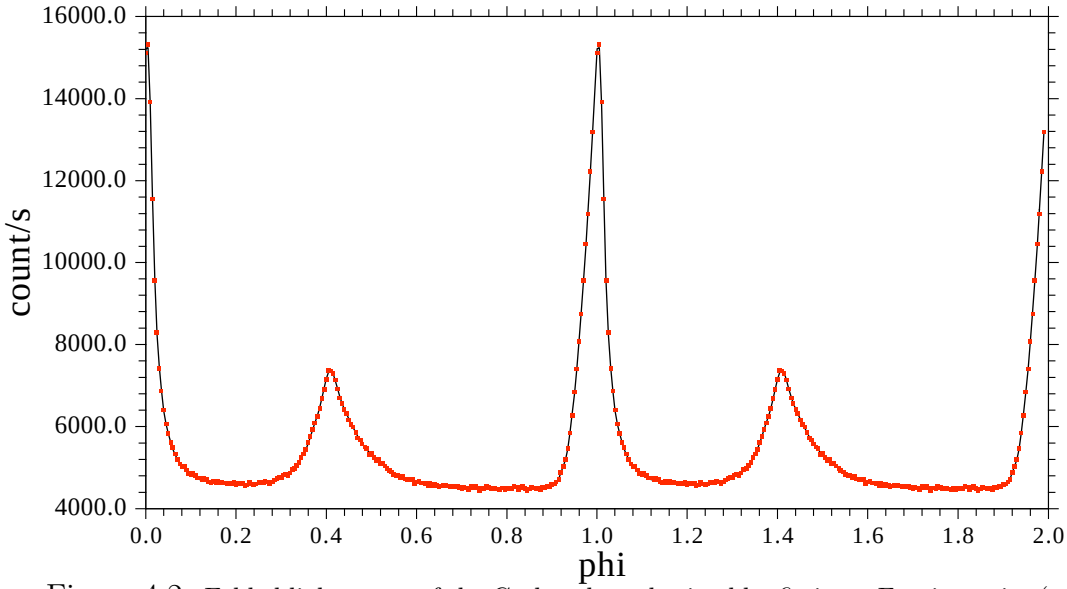

Figure 4.2: Folded light curve of the Crab pulsar obtained by fitting a Fourier series (see text). *Red points*: Observed folded light curve (observation 4 in Table 4.1). The error bars on the red points are of the order of tens of count/s. *Black curve*: fitted Fourier series.

where ν, $\dot{\nu}$ and $\ddot{\nu}$ are the rotational frequency, its first and second derivative, respectively. The phase ϕ_0 is the phase of the pulsar at the epoch t_0. Thus, the evolution of the phase $\phi(t)$ is dictated by ν, $\dot{\nu}$ and $\ddot{\nu}$.
In order to calculate the radio phase $\phi(t)$ we used the values of ν, $\dot{\nu}$ and $\ddot{\nu}$ nearest to our observation epochs and reported in the JB archive[2]. Then $\phi(t)$ is extrapolated all over our observation run by means of (4.1). What we are actually interested in is the phase-drift of (4.1) with respect to a phase $\phi'(t) = (t - t_0)/P_{ini} = \nu_{ini}(t - t_0)$, where P_{ini} is the rotational period used to calculate the optical phase from Aqueye/Iqueye (see Section 3.3 and 4.4). Therefore, we compare the optical phase to the radio phase described by

$$\Delta\phi = \phi(t) - \phi'(t) = \phi_0 + (\nu - \nu_{ini})(t - t_0) + \frac{1}{2}\dot{\nu}(t - t_0)^2 + \frac{1}{6}\ddot{\nu}(t - t_0)^3 \quad (4.2)$$

Equation (4.2) checks the correct functioning of our instruments. Indeed, if the optical-P_{ini}-folded-phase matches (4.2) then it means that Aqueye/Iqueye is seeing the Crab pulsar as reported in the Jodrell Bank radio ephemerides archive.
The phase ϕ_0 at epoch t_0 is calculated with a Fortran code available in

[2]http://www.jb.man.ac.uk/ pulsar/crab/all.gro

the radio ephemerides website[3]. Since the Fortran program makes use of a different ephemerides table[4], we tied ϕ_0 in (4.2) to that from the Fortran code. In order to check the consistency of our radio phase behaviour (4.2) we compared it to the radio ephemerides that Jodrell Bank directly sent us (Andy Shearer, private comunication). A remark should be done: For our typical observation runs (a few days) the role of $\ddot{\nu}$ maybe considered negligible.

4.4 The Crab pulsar observed in Asiago

The Crab pulsar was observed by the Aqueye team with the novel photon-counter Aqueye mounted on the Copernicus telescope at Cima Ekar in Asiago (Zampieri et al. 2011). For a log of the observations see Table 4.1. The TOAs were corrected to the Solar System Baricenter (SSB) by means of the software Tempo2[5] (Hobbs et al. 2006a; Edwards et al. 2006), that accurately accounts for general relativistic effects on both the photon's trajectory and on the time beaten by clocks at different coordinates in the Solar system's potential (see Chapter 3).

The first step in our reduction is the calculation of the phases, by cross-correlation of a standard template with the Crab profile averaged over n seconds long intervals (see Section 3.3). Then the measured drift of the phase with respect to a reference phase is fitted with a polynomial expression whose coefficients are the first and second derivative of the phase drift:

$$\psi(t) = \psi_0 + a(t - t_0) + b(t - t_0)^2. \tag{4.3}$$

Usually, for longer baselines, a cubic polynomial accounting for the third derivative of the phase is needed. In our case, a 2 days baseline, it is sufficient the second derivative of the phase. The second derivative of the phase gives the first derivative of the frequency. In order to understand that (4.3) is sufficient to fit the phase drift over a baseline of days, we can make the following calculation. The first derivatve of the period is estimated to be $\dot{\nu}/\nu^2 \sim 4\times10^{-13}$ s/s and the second derivative is $\sim \dot{\nu}^2/\nu^3 \sim 10^{-24}\mathrm{s}^{-1}$, where ν and $\dot{\nu}$ are the rotational frequency and its first derivative. Therefore over a 2 days baseline the first derivative changes by $\sim 10^{-19}$s/s and the changing of the period over 2 days due to the second derivative is $\sim 10^{-14}$s, too small to be detected by Aqueye. Therefore, over a baseline of a few days, the second derivative of the frequency is negligible. This means that we can neglect the

[3]http://www.jb.man.ac.uk/ pulsar/crab.html
[4]http://www.jb.man.ac.uk/ pulsar/crab/crab2.txt
[5]http://www.atnf.csiro.au/research/pulsar/ppta/tempo2

third dervitative of the phase, and thus fitting the phase drift to a parabola (eq. [4.3]).

The first derivative of (4.3) gives the shift in frequency in order to carry the assumed value of $1/P_{ini}$ to the true frequency at each n seconds integration. In other words, the true phase is

$$\phi(t) = \frac{(t - t_0)}{P_{ini}} + \psi(t) \tag{4.4}$$

where P_{ini} is the period at a given epoch used in the folding to calculate the folded light curve on intervals n seconds long; t_0 is the epoch to which all the measured phases after the folding are referred (see Section 3.3); a, b are the coefficients determined by the fit. Thus the rotational frequency at a given epoch t is $\nu(t) = d\phi(t)/dt$.

The above phase-analysis has been applied with two different assumptions for the barycentrization:
Tempo1 as emulated by Tempo2 (TDB time units are implicitly assumed) and Tempo2 in TCB units. The difference between TDB and TCB time units is a rate of 1.550 519 791 54$\times 10^{-8}$s/s (Irwin & Fukushima 1999). It is the mean value of the Einstein integral (eq.[3.2]), i.e. the mean value of both the time dilation and gravitational redshift, plus the value of the gravitational redshift on the surface of the geoid, due to the Earth gravitational potential (second term in eq.(3.3); see also Backer & Hellings 1986). Therefore the time in TDB units is not the proper time experienced by an inertial observer. The IAU resolution A4 (1991) recommends the use of the barycentric coordinate time (TCB). If TDB is used it should be specified. For uniformity reasons the Jodrell Bank (JB) monthly radio ephemerides are in TDB units. Moreover they are computed with a previous version of Tempo2, i.e. Tempo (hereafter Tempo1). Therefore in order to compare our measurements to JB radio ephemerides, we baricentered TOAs in the Tempo1 emulation mode. However, in order to have ephemerides in SI units we baricentered them in Tempo2 TCB units as well. The Jodrell Bank radio ephemerides are calculated setting the proper motion of the source equal to zero, and assuming the position of the Crab pulsar at J2000. Thus, in order to compare our measurements with JB radio ephemerides, in the barycentrization with Tempo1 we had to set a zero proper motion of the source as well.

The mean rate difference $K-1 = 1.550\ 519\ 791\ 54\times 10^{-8}$s/s (Hobbs et al. 2006a) between TDB and TCB units leads to rotational periods 0.5 ns longer than those reported in the JB radio ephemerides. Indeed, over the rotational period of the Crab (~ 0.033 s) the mean rate gives a 0.5 ns discrepancy.
Fig. 4.3 (top) shows the parabola fitted (blue line) to the phase calculated with Tempo2. The first observation is at $t \sim 86400$ s because the reference

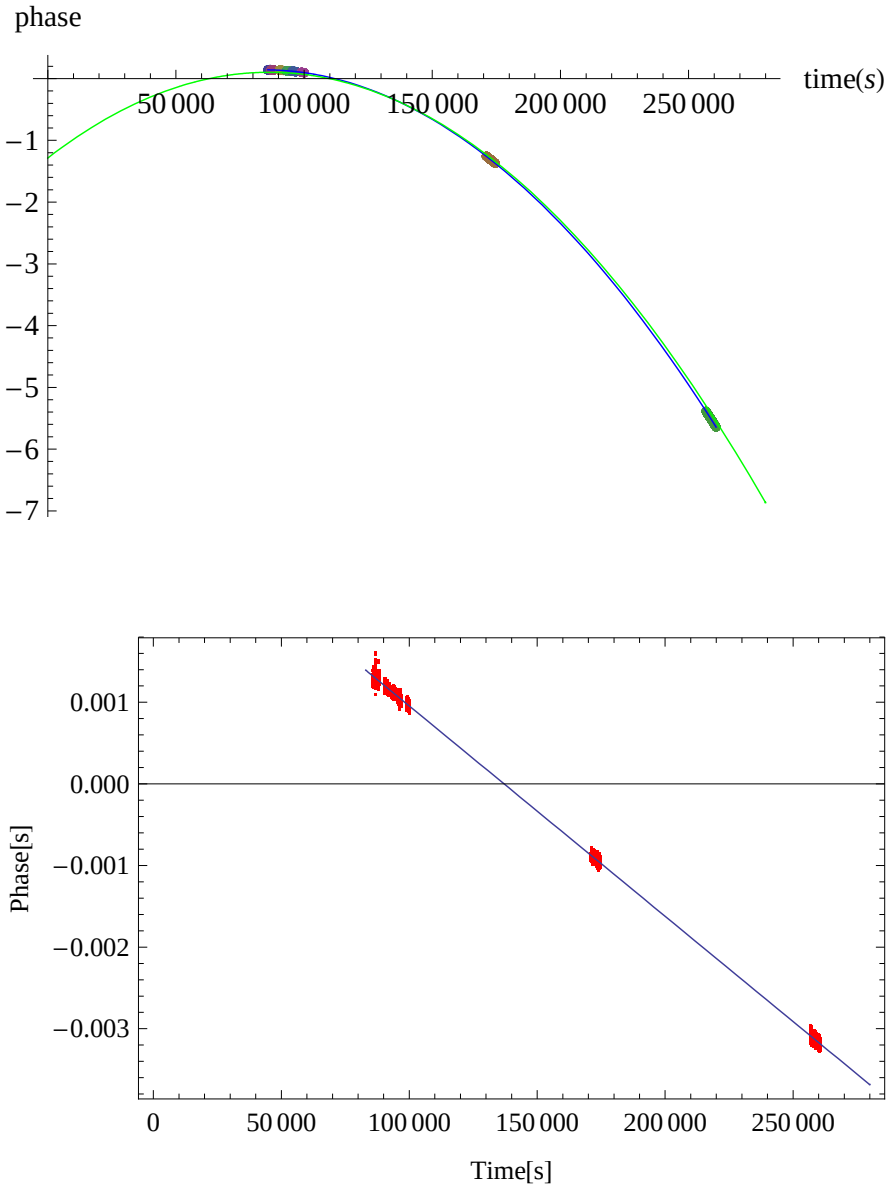

Figure 4.3: *Top*: The parabolic fit to the phase-drift measured by Aqueye (points). The different colours of the points indicates different observations (see Table 5.1 for a log of the observations). The blue line shows the best-fitted parabola. The green line is the phase from JB radio ephemerides. *Bottom*: The residuals left after subtracting the JB phases to those measured by Aqueye (see text).

epoch t_0 is at MJD=54749 (00:00:00 October 10, 2008), see Table 5.1. The green line is the parabola as from the JB radio ephemerides. Since we want

to check whether there is a difference in the curvature of the two curves, the initial phase is chosen such that the two curves match at MJD=5479.99. Already in this plot we note that, as time goes on, the blue curve drifts with respect to the green one. This means that the function $\psi(t)$ we measured does not match that from JB radio ephemerides (eq.[4.1]). Fig 4.3 (bottom) shows this discrepancy: It shows the residulas of the optical phases after subtracting the JB radio ones (green line). We see that there is a discrepancy up to $\sim 5ms$ over 2 days. The blue straight line is a fit to the residuals (red points) and shows a liner trend of $\sim 2.6\times10^{-8}s/s$. Thus, besides the mean rate difference between TCB and TDB units ($K - 1 = 1.550\ 519\ 791\ 54\times10^{-8}$s/s) there is something else leading the phases even further apart. However, we are comparing data baricentered in Tempo1 (Jodrell Bank) with those obtained from Tempo2 (Aqueye phases). We know that Tempo2 takes into account corrections which Tempo1 does not (e.g. polar motion of Earth, Shapiro delays due to gaseous planets and other features listed in Table 2 in Hobbs et al. 2006a). Therefore, the further $\sim 1.1 \times 10^{-8}s/s$ might be due to some of these corrections.
If we calculate the rotational periods with the best-fitted parabola to the data (blue line; eq. [4.4]) they are sistematically 0.9 ns longer than those reported in the JB ephemerides. Therefore we have a further 0.4 ns discrepancy.

4.4.1 On the origin of the further 0.4 ns discrepancy

In order to understand the further 0.4 ns discrepancy we ran the baricentrization in the Tempo1 emulation mode, performed again the phase-analysis and fitted the quadratic polynomial (4.3) to the phases; the following is the solution we got from the best fit:

$$\psi_{Tempo1}(t) = -0.778649 + \frac{0.0000318096}{s}t - \frac{1.85916 \times 10^{-10}}{s^2}t^2 \qquad (4.5)$$

We calculated the rotational periods from (4.5) and the ∼0.4 ns discrepancy with respect to the JB radio ephemerides is still there.
To check in more detail possible differences between Tempo2 and Tempo1 we ran again the baricentrization in Tempo2 but now in TDB units, since Tempo1 works only in TDB units. The following is the solution we got from the best fit:

$$\psi_{Tempo2TDB}(t) = -0.778837 + \frac{0.0000318182}{s}t - \frac{1.85934 \times 10^{-10}}{s^2}t^2. \quad (4.6)$$

We subtract (4.5) to (4.6) and plot the residuals between them in Fig. 4.4. There are residuals up to 26 μs (0.0008) in phase and therefore either Tempo2

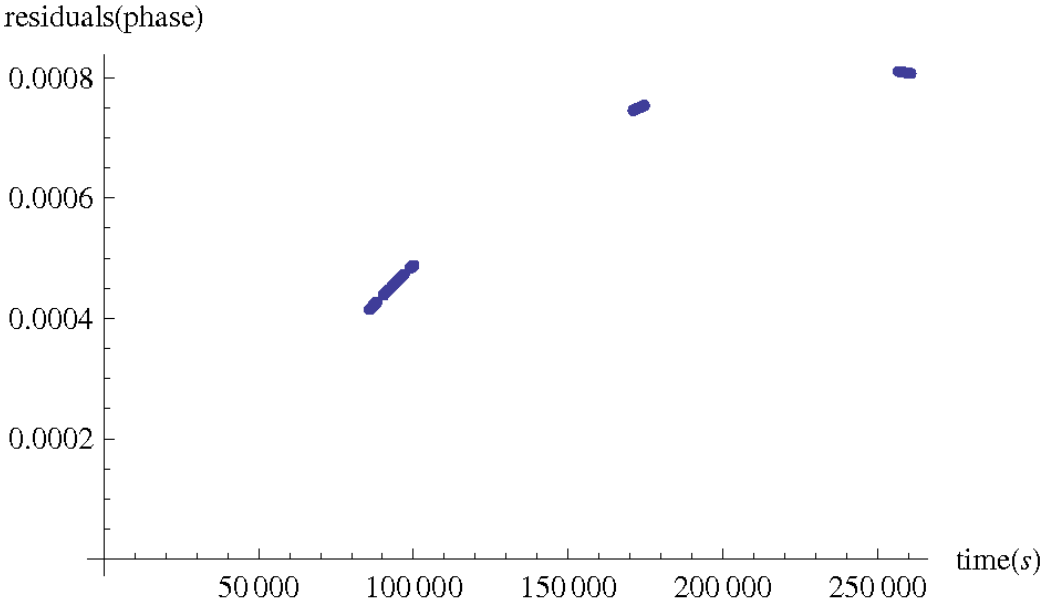

Figure 4.4: Residuals between (4.6) and (4.5).

or Tempo1 leaves some physical effects unmodelled. To check this further out we fit a cubic to the phases instead of a quadratic

$$\psi(t) = \psi_0 + a(t - t_0) + b(t - t_0)^2 + c(t - t_0)^3; \tag{4.7}$$

if there is some physical effect left unmodelled, it will be absorbed in the cubic term and the difference with the corresponding quadratic may reveal the origin of the 0.4 ns discrepancy.
From the best fit of the Tempo2TDB-phases to a cubic we get the following solution

$$\psi_{Tempo2TDB-cubic} = -0.777428 + 0.0000317892t - 1.85754\times10^{-10}t^2 - 3.46131\times10^{-19}t^3 \tag{4.8}$$

and its difference with the corresponding quadratic (4.6) is shown in Fig. 4.5 (top).
The best-solution from the fit of the Tempo1-phases to the cubic is

$$\psi_{Tempo1-cubic} = -0.796768 + 0.0000321824t - 1.88238\times10^{-10}t^2 + 4.45013\times10^{-18}t^3 \tag{4.9}$$

and its difference with the corresponding quadratic (4.5) is shown in Fig. 4.5 (bottom). We note that there are residuals up to 0.0004 in the Tempo1 case,

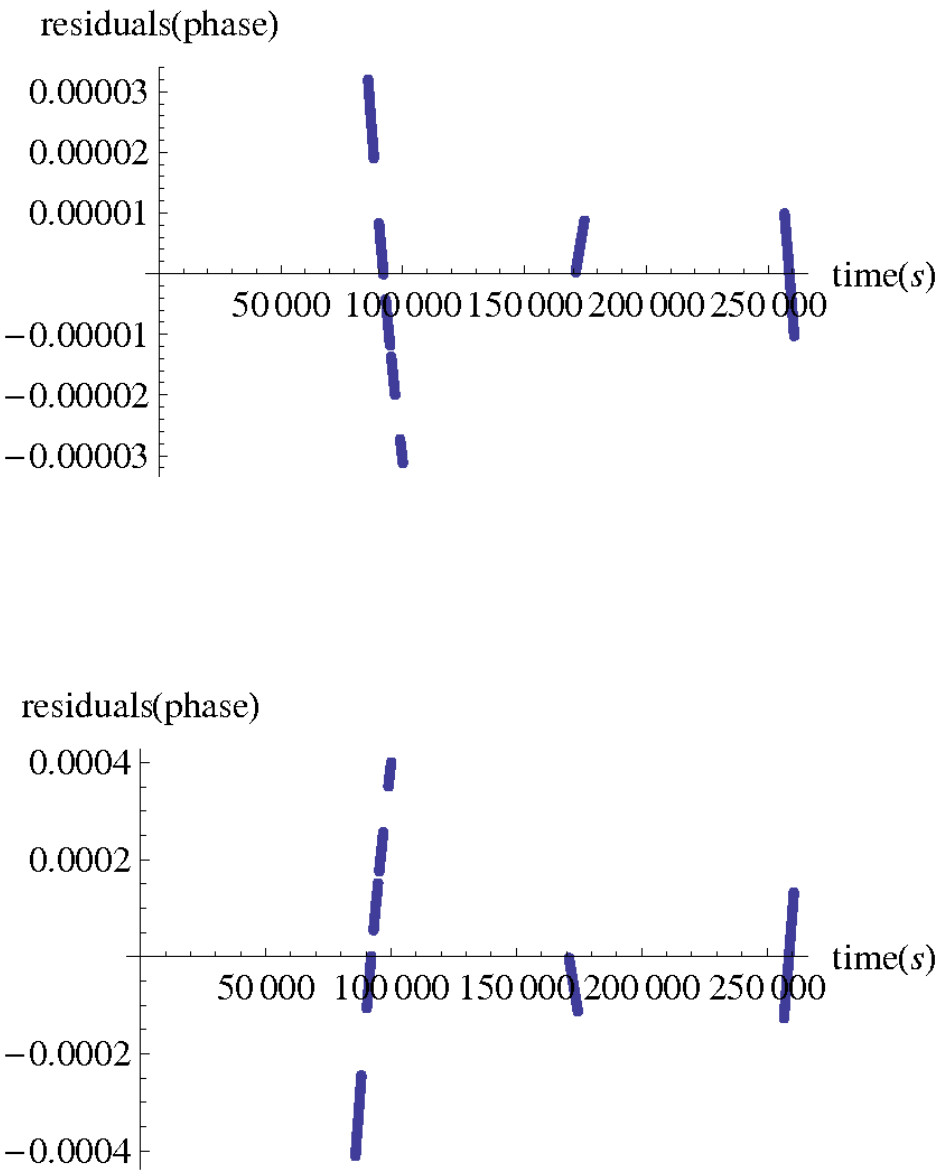

Figure 4.5: *Top*: Residuals between the cubic (4.8) and the quadratic (4.6) for the Tempo2TDB case. *Bottom*: Residuals between the cubic (4.9) and the quadratic (4.5) for the Tempo1 case. In the Tempo1 case the residuals are one order of magnitude bigger than those in the Tempo2TDB case.

therefore one order of magnitude bigger than those shown in the Tempo2TDB case. This might mean that Tempo1 does not properly correct for some physical effect. The rotational periods of the Crab calculated with (4.9)

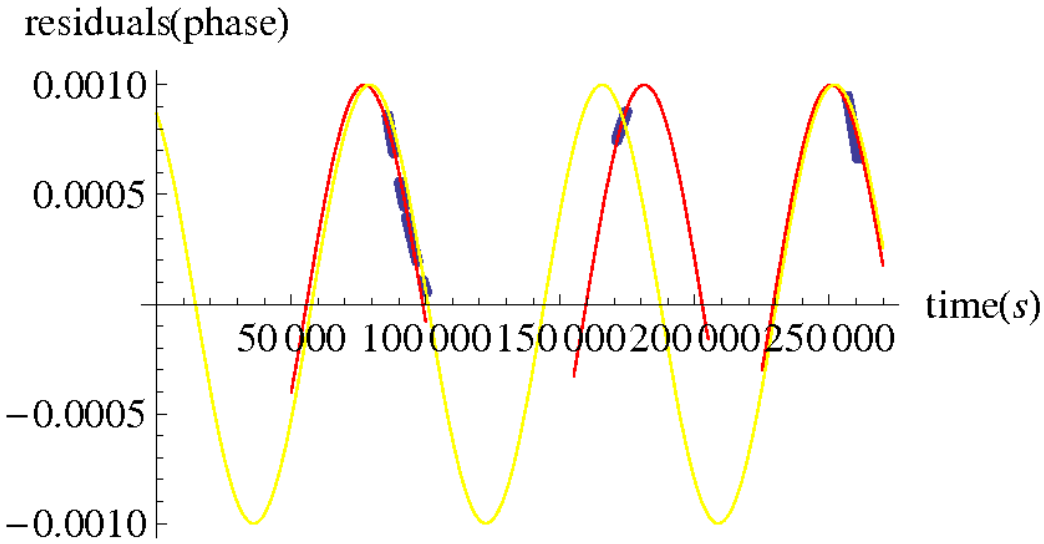

Figure 4.6: Residuals between the cubic (4.8) (Tempo2TDB) and (4.9) (Tempo1) (blue points). The amplitude in phase corresponds to $\sim 26 \mu s$. The yellow curve is a sinusoid with a diurnal period. The red curve in the middle is a portion of the yellow sinusoid shifted in phase. The trend of the residuals is much alike to that shown in Hobbs et al. (2006) (see also Fig. 3.1).

are not anymore sistematically 0.4 ns longer than those from the JB radio ephemerides: The discrepancy oscillates over the 2 days baseline from -0.4 ns to 0.4 ns.

It is instructive to study the difference between the Tempo2TDB-cubic-best-solution (4.8) and the Tempo1-cubic-best-solution (4.9). Fig. 4.6 shows the residuals. The shape of the residuals reminds a characteristic diurnal oscillation shown in Hobbs et al. (2006a, Fig. 4) and here reported in Fig. 3.1. The plot shows the difference of the Roemer delay as calculated by Tempo2 and Tempo1. As explained in Hobbs et al. (2006), the characteristic diurnal trend reflects the rotation of Earth and it shows up once we subtract the Roemer delay as calculated by Tempo1 to that from Tempo2. The Roemer delay is the light travel time from the observatory to the solar system baricenter (SSB), projected onto a vector from SSB to the source (see Section 3.1.2).

The phenomenon related to the trend in Fig. 3.1 is the polar motion of Earth. Since the rotation axes of Earth changes direction in an almost unpredictable way, the position of the true pole differs from that of the mean pole. That is, the position of the true pole is off with respect to that of the mean pole. Thus this offset affects the coordinates of the observation

site as well. If the coordinates of the observatory are not corrected for the polar motion then the Roemer delay is wrongly estimated and the offset shows up with a typical diurnal trend (see Section 3.1.2). Tempo1 does not correct for the polar motion, Tempo2 does. Moreover, Tempo1 uses an out of date precession-nutation model. However the large offset of $\sim 26 \mu s$ we get in Fig. 4.6 is not expected. As explained in Hobbs et al. (2006a) the offset between Tempo1 and Tempo2 expected from the polar motion correction is 40 ns at most.

To check for the correctness of the Roemer delay estimate we simulated a string of TOAs over a baseline of several years. Fig. 4.7 shows what is not expected: There is a huge divergence up to $\sim 30 \mu s$ from MJD$\sim$54500 on. The typical oscillations of $\sim$ 40 ns as reported in Hobbs et al. (2006a) are all over the flat region. The Asiago observation campaign is around 54750. Thus at these epochs the Roemer delay is wrongly estimated, introducing the 0.4 ns discrepancy we systematically get with respect to the JB radio rotational periods. For the record, the observations taken during the NTT campaign fall around MJD=54847 and MJD=55181. At these epochs the Romer delay difference begins again to be as expected. Indeed for the NTT campaign we never got this additional 0.4 ns discrepancy.
We checked the software for the origin of this problem. The bug was in the procedure for updating the configurative files described in the Tutorial. Therefore we downloaded all the files from the link
http://tempo2.cvs.sourceforge.net/viewvc/tempo2/tempo2/T2runtime/
and posted by "ankurchaudhary". Then we ran again the software to check for the trend of the Roemer delay difference. Fig. 4.7 (bottom) shows the trend one expects and shown in Fig. 4 of Hobbs et al. (2006a).

Having in mind all this analysis we can conclude that the instrument is able of detecting very small inaccuracy in the modelling of the TOAs from the pulsar to the observatory. For instance, we may think of using Aqueye in geological applications, e.g. monitoring the polar motion of Earth all along the years, i.e. studying this phenomenon by means of the extremely precise pulse-time-tagging from the Crab pulsar that Aqueye provides. Other applications might deal with the continental drift expected to be a few centimeter per year, leading to errors on TOAs of few ns.
Trying to give measures of the conversion factor K (Section 4.4) is tempting with such an instrument. The factor K gives the rate at which a non-inertial clock in the Solar system gravitational well beats the time with respect to an inertial one. The value quoted in literature is the mean value of the Einstein integral plus a term describing the gravitational redshift due to Earth. The K-value is calculated by interpolations and by means of numerical planetary ephemerides (Irwin & Fukushima 1999). Aqueye may be sensitive to the

variation of K during the year, depending on the position of Earth on its orbit and on the positions of the other planets.

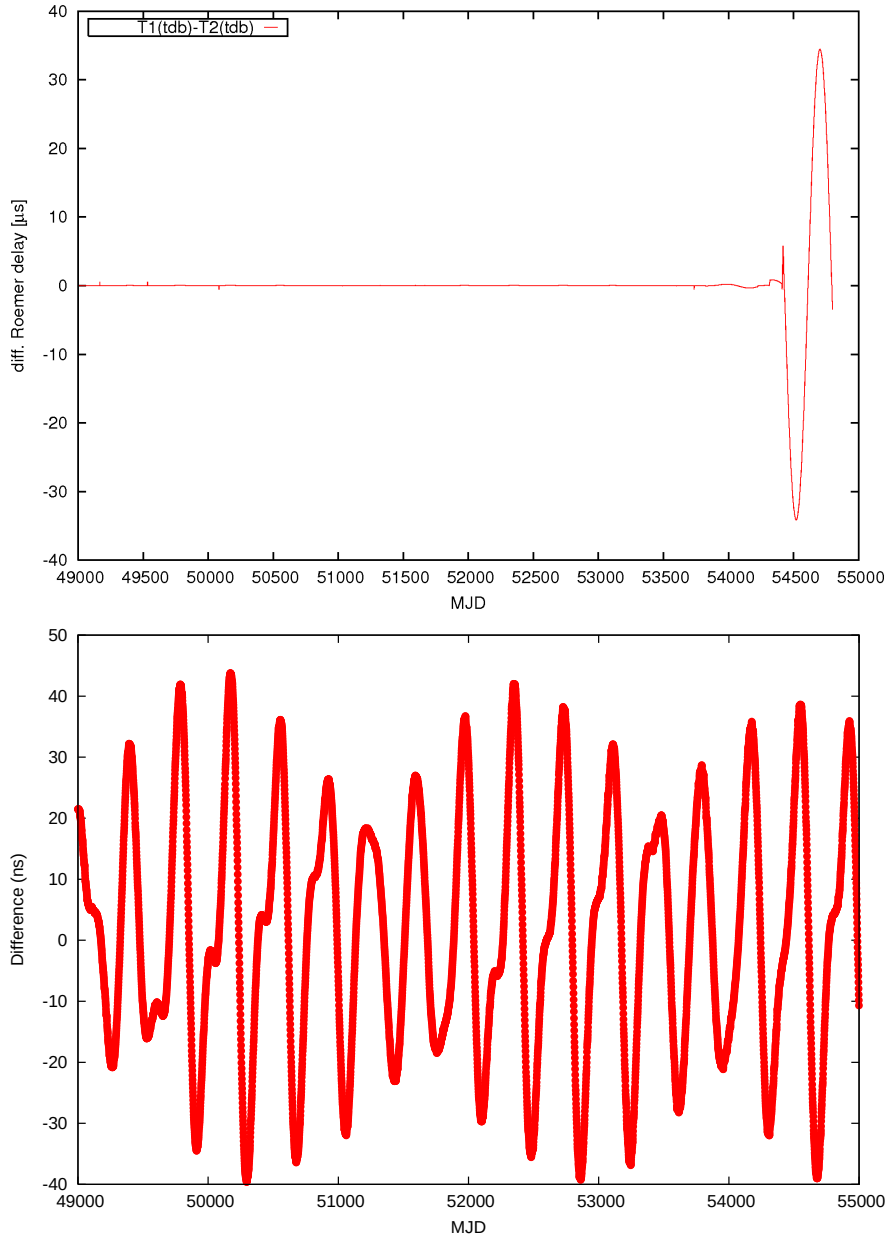

Figure 4.7: *Top*: Roemer delay difference Tempo2-Tempo1. The trend one expects are oscillations of ~ 40 ns in amplitude due to the polar motion of Earth not accounted for by Tempo1. The plot shows a huge divergence of amplitude of $\sim 30\mu s$ from MJD$\sim$54500 on. *Bottom*: The trend one expects as shown in Fig. 4 of Hobbs et al. (2006a) after loading in the software the correct updated files.

4.5 Rotational periods and first derivative measured by Aqueye in Asiago

From the behaviour of the observed phase of the pulsar one can estimate the rotational period and its derivatives. Fig. 4.8 shows the best-fitted parabola $\psi(t)$ (blue curve; equation 4.3) to the phase-drift of the Crab with respect to a reference phase. The reference epoch the phase-drift is calculated with respect to is $t_0 = 0$ (MJD=54749.0). In order to compare our ephemerides to those by Jodrell Bank, the time of arrivals were barycentered in the Tempo1 mode. We note that the parabola from Jodrell Bank ephemerides is off by the expected phase-shift (Shearer et al. 2003; Oosterbroek et al. 2008) between optical and radio (Fig. 4.8 middle; see Chapter 6).
In Section 4.4 we have seen that the true phase of the pulsar is

$$\phi(t) = \frac{(t - t_0)}{P_{ini}} + \psi(t). \tag{4.10}$$

The first derivative of (4.10) gives the rotational frequency of the pulsar at a given epoch t

$$\nu(t) = \frac{d\phi(t)}{dt} = \frac{1}{P_{ini}} + \dot{\psi}(t) \tag{4.11}$$

and the rotational period is $P = 1/\nu$. Here P_{ini} is the period at a given epoch used as reference in the estimation of the phase-drift. In this analysis we used the radio period at MJD=54750.0, $P_{ini} = 0.0336216386529$.
The best-fitted soultion $\psi(t)$ is

$$\psi(t) = 0.9683 + \frac{0.0000321341}{s}t - \frac{1.85941 \times 10^{-10}}{s^2}t^2 \tag{4.12}$$

and the rotational frequency as fuction of time

$$\nu(t) = \frac{d\phi(t)}{dt} = \frac{1}{0.0336216386529}Hz + 0.0000321341Hz - 3.71882 \times 10^{-10}Hzt. \tag{4.13}$$

In Table 4.3 we report the rotational periods at the beginning of each observation as measured by Aqueye (see Table 5.1 for a log of the obsevations). In the table the periods at the same epoch reported in the Jodrell Bank radio ephemerides are also given.
While we postpone a more detailed treatment of the error on the rotational periods to a forthcoming investigation here we provide an order of magnitude estimate as follows (Boynton et al. 1972). In Fig. 4.8 (bottom) the residuals after subtracting the best-fitted parabola to the data are of the order of 0.003

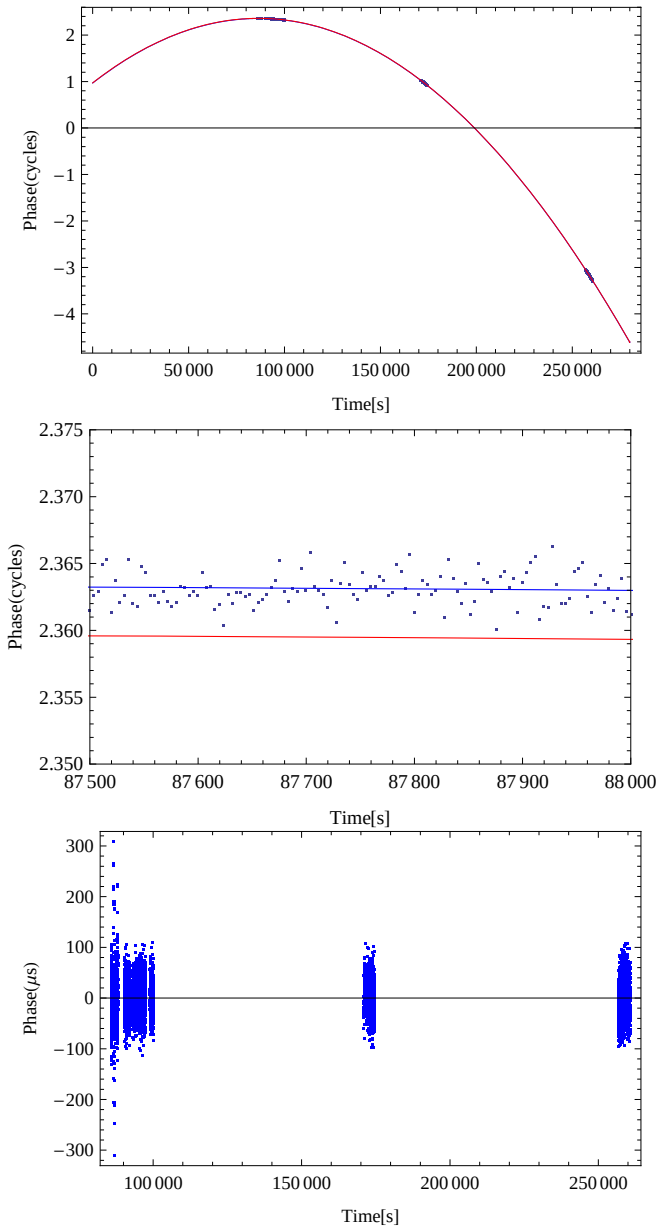

Figure 4.8: *Top*: Behaviour of the phase-drift of the main peak of the Crab over the obsevation run in Asiago on October 2008 (blue points). The blue curve is the best-fitted parabola (eq[4.12]). The red curve is the parabola from the Jodrell Bank radio ephemerides (Section 4.3). *Middle*: A zoom-in of the plot on the top, showing the difference in phase between optical and radio (Shearer et al. 2003; Oosterbroek et al. 2008, see Chapter 6). *Bottom*: phase-residuals after subtracting to the blue points on the top the best-fitted parabola (eq[4.12]; blue curve).

Table 4.3: Rotational periods of the Crab pulsar measured by Aqueye in 2008 compared to those reported in the Jodrell Bank radio ephemerides (see Table 5.1). Time of arrivals were barycentered in the Tempo1 mode.

	MJD[a]	Period (As) (s)	Period (JB) (s)
1	54749.99287724855327	0.0336216384023	0.0336216384049
2	54750.00668638351852	0.0336216388933	0.0336216388959
3	54750.04505792216435	0.0336216402869	0.0336216402895
4	54750.07656540930556	0.0336216414313	0.0336216414339
5	54750.10252841002315	0.0336216423742	0.0336216423768
6	54750.14465028032407	0.0336216439041	0.0336216439067
7	54750.97900758696759	0.0336216742076	0.0336216742102
8	54751.97132990998842	0.0336217102484	0.0336217102510

[a] Corrected MJD at the solar system barycenter (Tempo1 mode).

Table 4.4: Rotational periods of the Crab pulsar measured by Aqueye in October 2008 (see Table 5.1 for a log of the observations). Time of arrivals were barycentered with Tempo2 (TCB units).

	MJD[a]	Period (s) (Asiago)
1	54749.99304560657631	0.0336216389066
2	54750.00685473487799	0.0336216394081
3	54750.04522628093586	0.0336216408017
4	54750.07673377043712	0.0336216419460
5	54750.10269677046000	0.0336216428890
6	54750.14481863190191	0.0336216444188
7	54750.97917596163527	0.0336216747218
8	54751.97149830025131	0.0336217107620

[a] Corrected MJD at the solar system barycenter (Tempo2 mode).

in cycles ($\sim 100\mu s$). We assume this error as the error in measuring the phase of each point. The number of phases measured in each observation night is $N \sim 1122$ (each point refers to the phase calculated over a 2 s interval). Assuming that the noise follows a Poisson distribution, the average phase,

on each observation night, is uncertain by $0.003/\sqrt{1}122 = 9 \times 10^{-5}$ (e.g. see Boynton et al. 1972) and the phase difference $(\phi_2 - \phi_1)$ between beginning and end is uncertain by $\delta\phi = 1 \times 10^{-4}$. The average frequency measured during the baseline of the observations, $\Delta t = 172800$ s, is $(\phi_2 - \phi_1)/\Delta t$ and the error on this frequency is $\delta\nu = \delta\phi/\Delta t = 7 \times 10^{-10}$ Hz. Therefore the statistical error on the rotational periods is $\delta P = P^2\delta\nu = 1 \times 10^{-12}$ s. The statistical error on the radio period quoted by Jodrell Bank is $\sim 10^{-13}$ s. From Table 4.3 the rotational periods measured by Aqueye are systematically shorter than the Jodrell Bank ones by $\sim 3 \times 10^{-12}$ s. There is a discrepancy slightly bigger than the statistical error. This might be an indication of extra-noise from the source. However, since our error is an approximate estimate, no definitive conclusion can de drawn on extra-noise detected in Asiago. The last term in (4.13) is the first derivative of the rotational frequency. Jodrell Bank quotes a spin down in frequency of the neutron star (at MJD=54754.0) of $\dot{\nu} \sim -3.71865 \times 10^{-10}$. Our measurment is $\dot{\nu} \sim -3.71872 \times 10^{-10} \pm 2 \times 10^{-15}$. As will see in Chapter 5, this discrepancy is due to a mean drift of the optical phase with respect to the radio phase. We recently understood by comparison with simultaneous radio observations that those drifts in each observation run (Asiago/NTT runs), with different magnitude and sign from run to run, may be caused by short term variations of the dispersion measure and of the radio phase, that may differ from that reported in the Jodrell Bank radio archive. Therefore rotational periods are different by some ps. Differences in the first derivatives of the frequency $\dot{\nu}$ reported above might also be caused by this effect.

We would stress that in order to compare our data with those in the Jodrell Bank radio archive, we barycentered the time of arrivals (TOAs) we collected in the Tempo1 (Tempo) mode in Tempo2. The JB radio ephemerides are calculated with the previous version of the software Tempo. As we already mentioned in Section 4.4, in Tempo1 the length of the second is not the proper time beaten by an inertial clock. Moreover Tempo1 does not take into account for corrections that at this precision level might be relavant. Thus, in Table 4.4 we report the rotational periods after barycentering with Tempo2 in TCB units (see Section 4.4). The IAU resolution A4 (1991) recommends the use of the barycentric coordinate time (TCB). The main difference between rotational periods in the Tables 4.3, 4.4 is due to the use of TCB unints (SI units) instead of TDB. Since the TCB second is the proper time experienced by an inertial observer it is 1-K=1.550 519 791 54$\times 10^{-8}$ s (Irwin & Fukushima 1999) shorter than the TDB one and the rotational periods of the Crab are $\sim$ 0.5 ns longer than those in TDB units (see Section 4.4). We note also further and smaller differences, i.e. the ratio of the periods in Table 4.4 (TCB units) to those in the first column of Tables 4.3 (TDB

units) is not equal to the value K=1+1.550 519 791 54$\times 10^{-8}$ but ranges from $1+1.49992689\times10^{-8}$ to $1+1.52937061\times10^{-8}$. These differences may be due to either further corrections Tempo2 does (Hobbs et al. 2006a) or to some systematic errors in our data maybe introduced by Tempo1, such that the periods by Aqueye in Tables 4.3 do not agree with those from the Jodrell Bank radio ephemerides within the error we estimated. We would remind that we assumed a Poissonian noise to estimate the statistical error. It might be possible that if the noise in the source has a different distribution, then the error bar might be larger than that we estimated above (Patruno et al. 2009). A not yet clear component of noise in young pulsars (timing noise) has been observed by several authors, however over much longer integration time than those reported here (a few days) (Lyne et al. 1993; Scott et al. 2003). A further discussion on the discrepancies between optical and radio rotational periods in Tables 4.3 is given in Section 5.6.

4.6 Asiago-Jodrell phase-residuals

Fig. 4.9 shows the residual of the time of arrivals of the optical peak (Table 4.5) after subtracting the Jodrell Bank ephemerides. In order to calculate the time of arrival of the optical peak, we have to re-define the phase ϕ. The output of the code described in Section 3.3 gives a phase $\tilde{\phi}$ that describes how the beam of light from the pulsar is oriented with respect to the line of sight, which is how the radio phase is defined as well. Therefore, if at a given epoch t_0 the phase is $\tilde{\phi} = \tilde{\phi_0}$ then the time of arrival of the first pulse after t_0 at the detector is $T_{arr} = (1 - \tilde{\phi_0})P_0 = \phi_0 P_0$, where P_0 is the rotational period at t_0.

Fig. 4.9 shows that in Asiago the optical peak leads the radio one, in agreement with other authors (Shearer et al. 2003; Oosterbroek et al. 2008). The spreding on the residual is $\sim \pm 100\mu s$ (assumed as error bar). Since the number of points is $N \sim 1122$, for each observation night, the expected value of the time of arrival of the optical peak is uncertain by $\sim 100\mu s/\sqrt{N} \sim 3\mu s$ (Boynton et al. 1972). The quoted error for the JB radio peak at this epoch is $\sim 60\mu s$[6]. Therefore the optical peak leads the radio one by $\sim (113 \pm 60)\mu s$ (at $t = 86400$ s, epoch of the first observations). The blue line gives a slope of $(-7 \pm 43)\mu s$/day.

[6]http://www.jb.man.ac.uk/ pulsar/crab/crab2.txt

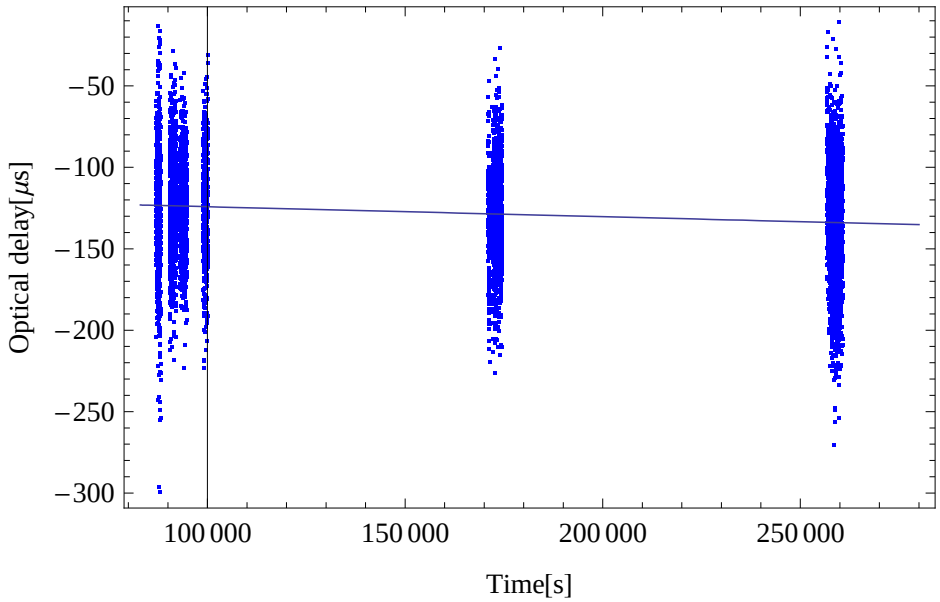

Figure 4.9: Residual of the the time of arrivals of the optical peak, measured by Aqueye, after subtracting the JB radio ones (see Fig. 4.8). The negative value means that the optical peak leads the radio one by $\sim 113\mu s$ (at $t = 86400$ s, epoch of the first observation; see text). The blue line is a linear fit to the residuals giving a drift of the optical peak with respect to the radio one by $\sim -7\mu s/day$. The time t=0 is at MJD=54749 (see Table 4.5 for a log of the observations).

4.7 The Asiago-Ljubljana observation campaign

A third fast photon counters was constructed for the 70 cm Vega telescope in Ljubljana, by the research group led by Prof. A. Čadež. The concepts design follow those of Aqueye. Unlike Aqueye, the prototype in Ljubljana has only one SPAD and the photon stream is focused on it by meas of an optical fiber.

In Oct. 2008, the Asiago and Ljubljana photometers were used for a campaign of synchronized observations of the pulsar in the Crab Nebula. To our knowledge, the only experiment of this kind was performed in 1971 by Horowitz et al. (1971). The aim of these join observations was to determine the stability of pulsar clock with respect to GPS clock and to determine the accuracy to which both observatories agree on the precise pulse arrival timing. Efforts in this campaign were also made to investigate the yet unknown physics of the phase (timing) noise seen in the pulsar (e.g. Boynton et al. 1972; Lyne et al. 1993; Čadež & Galičič 1996; Scott et al. 2003).

Table 4.5: The geodetic and geocentric different observing site considered in this work.

Telescope/Observatory	Copernicus/Asiago	Vega/Ljubljana
Geodetic long (° ′ ″)	+45 50 55.01	+46 02 37,65
Geodetic lat (° ′ ″)	+11 34 08.52	+14 31 39,73
Height (m)	1429	413
X (m)	4360967	4293298
Y (m)	892723	1112537
Z (m)	4554567	4568925

To prepare for this event, several prior activities, including the construction of a pulsar simulator built in Ljubljana by Prof. D. Ponikvar, were performed by the two teams in order to properly prepare and calibrate the two hardware sets. The coordinates of the two observatories in the WGS84 [7] reference frame are given in Table 4.5.

The relationship between the Time to Digital Converter (TDC) internal time and the GPS time was calculated in the following way (A. Čadež, 2008, Harrison project report). Let t_k be the TDC internal time at the k-th GPS second. A quadratic polynomial:

$$P_2(k) = c_2k^2 + c_1k + c_0 \tag{4.14}$$

is fitted to the function t_k and then the difference $t_k - P_2(k)$ is approximated with a Fourier series with 50 coefficients. Therefore, the TDC internal time as a function of GPS time is:

$$t_{\mathrm{TDC}}(t_{\mathrm{GPS}}) = c_2t_{\mathrm{GPS}}^2+c_1t_{\mathrm{GPS}}+c_0+\sum (a_icos((2\pi/T)it_{\mathrm{GPS}})+b_i(sin((2\pi/T)it_{\mathrm{GPS}})). \tag{4.15}$$

The measured scatter of residual differences $t_{TDC}(k) - t_k$ was about ±10ns (Fig. 4.10), consistent with the declared GPS accuracy. Since residuals were

[7] http://earth-info.nga.mil/GandG/publications/tr96201/tr96201.html

white noise we concluded that the TDC - GPS time transformation could not reasonably be improved any more, at least with the present quality of the GPS signal.

Subsequent to these initial tests, two receivers prepared by Thales Alenia Space Italy as prototypes for the GALILEO GNSS signals were brought to the Observatories. Further tests were performed by the two groups, again on the GPS signals and on the signals generated by the pulsar simulator. The results confirmed the previous ones, and actually were slightly better because the better quality of the GPS receiver inside the ACTS units. At this stage, the clocks of each group could be considered synchronized to the best possible precision with the available equipment, and indeed amply sufficient to reach the main scientific goal of the experiment, namely to unambiguously detect and measure phase noise in the pulsar.

Table 4.6: Log of the October 2008 observations of the Crab pulsar performed at the Vega telescope in Ljubljana. The start time of the observations is the GPS integer second, accurate to better than approximately +/-30 nanoseconds. Observations 2 and 3 are simultaneous observations with Asiago (see Table 4.1)

	Starting time (UTC)	MJD[a]	Duration (s)
1	October 10, 23:14:26	54749.968365918236522	1200
2	October 11, 00:07:22	54750.007936873654867	9658
3	October 11, 23:06:55	54750.963133542481746	3731
4	October 26, 22:21:55	54765.931893708696666	4306

[a] Corrected MJD at the solar system barycenter (Tempo1 mode).

Figure 4.10: Timing residuals $t_{TDC}(k) - t_k$ for the Asiago 3rd test run. Abscissa is time that spans over 1797 seconds.

4.8 Rotational periods and phase residuals in Ljubljana

Fig. 4.11 shows the phase-drift behaviour in Ljubljana (Table 4.6) with respect to both a folding epoch (MJD=54749) and a rotational period ($P_{ini} = 0.033621638529$) (see eq.[4.11]). The best-fitted parabola in Fig. 4.11 gives the following solution

$$\psi(t) = 0.975337 + \frac{0.0000320063}{s}t - \frac{1.85441 \times 10^{-10}}{s^2}t^2. \qquad (4.16)$$

Following Section 4.5, the rotational frequencies of the Crab as measured in Ljubljana are

$$\nu(t) = \frac{d\phi(t)}{dt} = \frac{1}{0.033621638529}Hz + 0.0000320063Hz - 3.70882 \times 10^{-10}Hzt. \qquad (4.17)$$

Assuming an error on each measured phase of $\sim 300\mu s$ (Fig. 4.11, bottom), the statistical error on the rotational periods is $\delta P \sim 1 \times 10^{-12}$ s (Section 4.5). The statistical error on the radio period from the Jodrell Bank archive is $\sim 10^{-13}$ s. The difference between the optical periods measured in Lj and the radio ones shown in Table 4.7 is from $\sim 4 \times 10^{-11}$ at obs 1, to $-1.5 \sim 10^{-9}$ at the obs 4 15 days later. The discrepancy at obs 4 is huge. It is a conseguence of the optical-radio phase drift which is huge over a 16

Table 4.7: Rotational periods of the Crab pulsar measured at the Vega telescope in Ljubljana on 2008 compared to those reported in the Jodrell Bank radio ephemerides (see Table 5.1). Time of arrivals were barycentered in the Tempo1 mode.

	MJD[a]	Period (Lj) (s)	Period (JB) (s)
1	54749.968365918236522	0.0336216375577	0.03362163751103
2	54750.007936873654867	0.0336216388658	0.03362163882257
3	54750.963133542481746	0.0336216735914	0.03362167364063
4	54765.931893708696666	0.0336222158078	0.03362221729010

[a] Corrected MJD at the solar system barycenter (Tempo1 mode).

days baseline. Such phase-drift may be an indication of noise larger than that expected, however it needs further investigations.

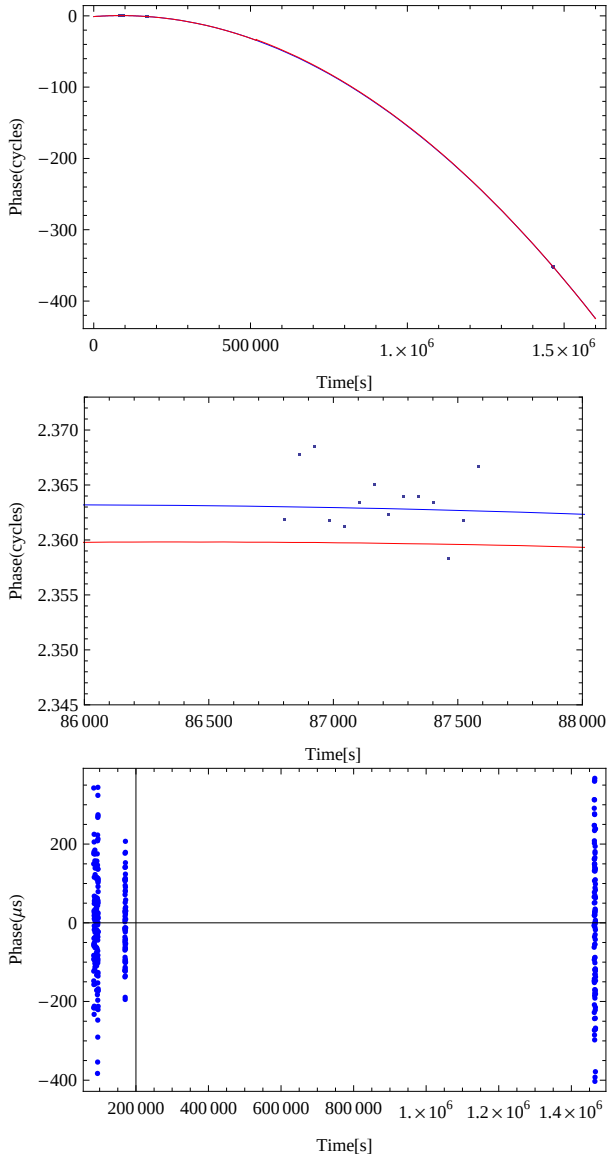

Figure 4.11: *Top*: Behaviour of the phase-drift of the main peak of the Crab over the obsevation run in Ljubljana on October 2008 (blue points). The blue curve is the best-fitted parabola (eq[4.16]). The red curve is the parabola from the Jodrell Bank radio ephemerides (Section 4.3). *Middle*: A zoom-in of the plot on the top, showing the difference in phase between optical and radio (Shearer et al. 2003; Oosterbroek et al. 2008). *Bottom*: phase-residuals after subtracting to the blue points on the top the best-fitted parabola (eq[4.16]; blue curve). The simmetry of the residuals testifies the stringent phasing over 16 days.

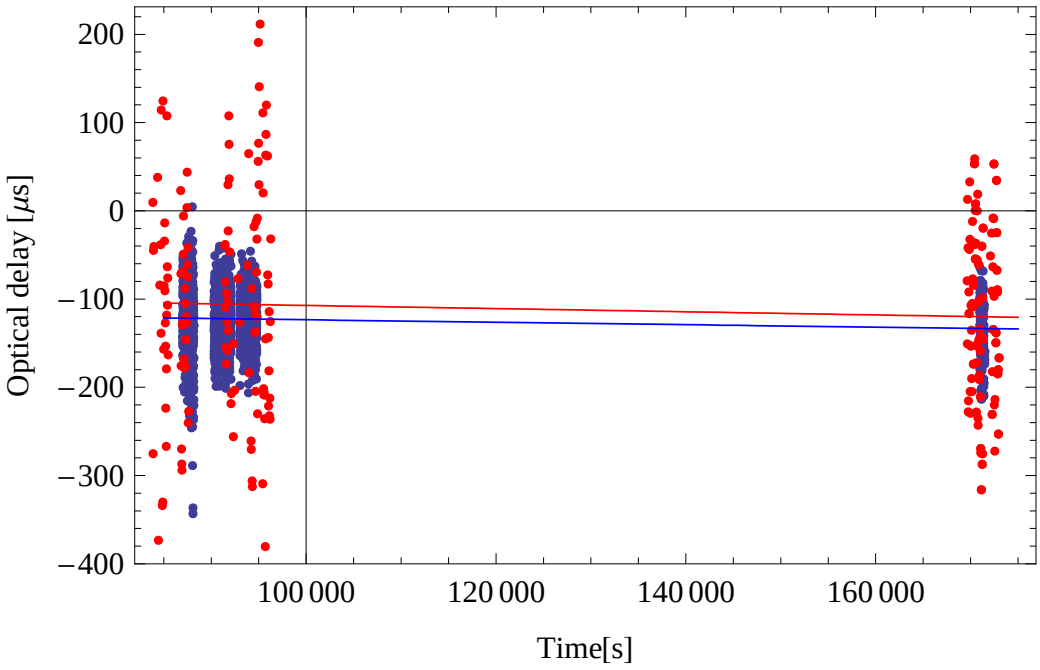

Figure 4.12: Residual of the time of arrivals of the optical peak, with respect to the radio peak, for the Asiago-Ljubljana simultaneous observations. Red points are the Ljubljana observations (see Table 4.6), the blue points the Asiago ones (see Table 4.1). The blue and red lines are linear fits showing a slop of $\sim -15\mu s/day$ (see text).

4.8.1 The Asiago-Ljubljana joint observations

Fig. 4.12 shows the residual of the time of arrivals of the optical peak after subtracting the radio ones to both the simultaneous Asiago-Ljubljana observations (obs 2 and 3 in Table 4.6, obs 2, 3, 4 and half of obs 7 in Table 4.1). The number of time of arrivals for each observation in the Lj run is $N \sim 50$. Each phase-point has been calculated over segments 33 s longer, because of the lower count rate in Lj than Asiago. We would remind that in Asiago the phase is calculated over segments 2 s long. In Ljubljana each time of arrival is uncertain by $300\mu s$, therefore the expected optical time of arrival is uncertain by $300\mu s/\sqrt{N} \sim 35\mu s$ (Boynton et al. 1972). The quoted error by Jodrell Bank on the radio peak is $60\mu s$. Hence the optical peak in Ljubljana leads the radio one by $\sim (104 \pm 70)\mu s$ at $t \sim 86400$ s (epoch of the first observation.)

On this temporal baseline, the expected optical time of arrival in Asiago, in each observation night, is uncertain by $100\mu s/\sqrt{671} \sim 4\mu s$. The optical peak in Asiago leads the radio one by $\sim (121 \pm 60)\mu s$ (the radio error

Table 4.8: Rotational periods of the Crab pulsar measured during the Asiago-Ljubljana observations). Time of arrivals were barycentered in the Tempo1 mode.

	MJD[a]	Period (As) (s)	Period (Lj) (s)
2	54750.007936873654867	0.03362163890	0.03362163916
3	54750.963133542481746	0.03362167418	0.03362167396

[a] Corrected MJD at the solar system barycenter (Tempo1 mode).

dominates).

The difference of the time of arrival of the optical peak as seen by the two observatories is $\sim 17\mu s$ (at $t \sim 86400$ s). The peak in Ljubljana is uncertain by $35\mu s$, that in Asiago by $4\mu s$, thus the error on the residual Ljubljana-Asiago is $\sim 35\mu s$. The optical peak from the Crab pulsar as seen at both observatories is aligned within the error. Over this temporal baseline, both runs show a drift in the phase-residuals of $\sim -15\mu s$/day, with an error bar of $\sim 90\mu s$ for Lj.

Table 4.8 shows the rotational periods measured in As and in Lj from the best-fitted parabolas over the simultaneous run (obs 2 and 3 in Table 4.7, obs 2, 3, 4 and half of obs 7 in Table 4.1). The Poisson statistical error bar is $\sim 2 \times 10^{-11}$ s for Lj, $\sim 10^{-12}$ for As. The difference between the rotational periods in Table 4.8 oscillates from $\sim 2 \times 10^{-10}$ s to $\sim -2 \times 10^{-10}$ s over the simultaneous run. Fig. 4.13 shows in more detail the As-Lj phasing. The figure shows the difference of the best-fitted parabola to the As phases with that fitted to the Lj phases. We see that the difference is not within the Poisson error ($\sim 35\mu s$) all over the run. The slope of the parabola in Fig. 4.13 is the difference between the rotational periods measured at the two observatories. Thus, the periods agree around the maximum of the parabola, but they do not agree within the Poisson error ($\sim 10^{-11}$ s) at the observation epochs (red points). From the figure we also see in more detail that the difference of the time of arrival of the Crab optical peak as measured by the two observatories is within the Poisson error ($\sim 35\mu s$) only at some observation epochs. Whether this extra-noise component is intrinsic in the source or it is an artifact of the much lower count rate in Lj remains to be investigated. We would remind that both the instrumentations were calibrated to better than ± 10 ns by means of a pulsar simulator (Section 4.7).

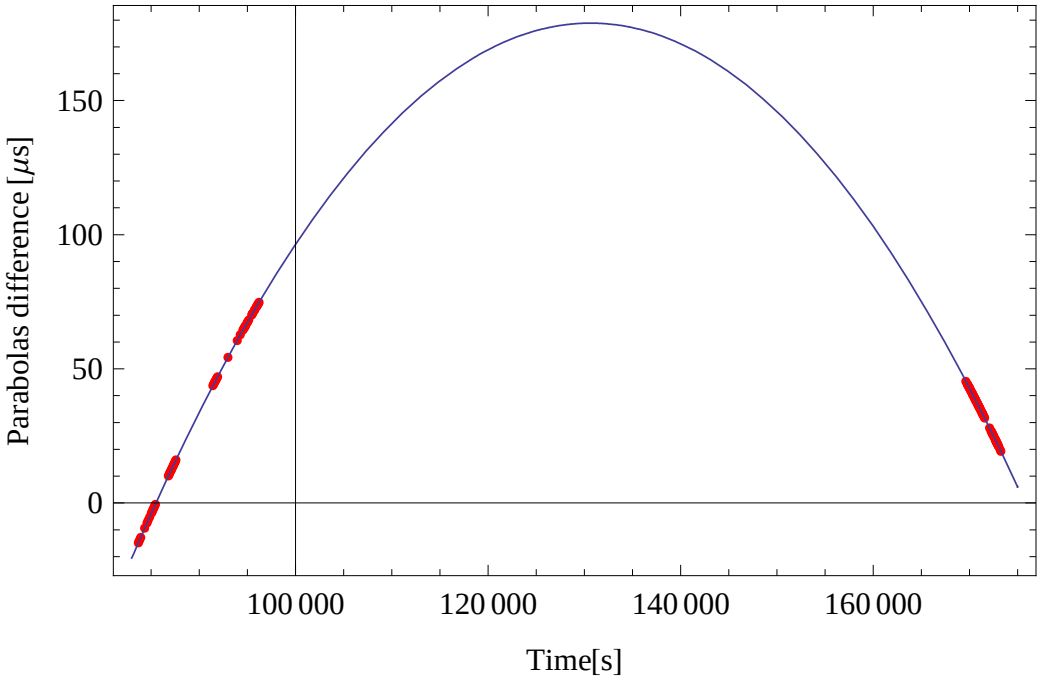

Figure 4.13: Difference of the best-fitted parabola to the Asiago phases with that fitted to the Lj phases during simultaneous observations.

As already mentioned, a more extensive analysis of the pulsar timing noise and related errors is needed before any definitive conclusion about all these discrepances can be drawn. A further discussion on the discrepancies we have described in this Chapter is given in Section 5.6.

Chapter 5

La Silla observations

The Crab pulsar was also observed by the team from the University of Padova with the extremely fast optical photon-counter Iqueye mounted at the NTT telescope in La Silla. The phase-analysis procedure described in the previous chapters was applied also to the data collected by Iqueye. The rotational period of the Crab was measured with an accuracy better than a few ps. The quality of the data is such that we were able to determine the pulsar first-order slow down over a baseline of only 2 days.
We compared our measurements to the Jodrell Bank radio ephemerides. Discrepancies with respect to the radio ephemerides and possible implications are discussed as well.

5.1 Iqueye: The Italian Quantum Eye

For a description of the scientific motivations of Iqueye and of its optomechanical characteristics see Barbieri et al. (2009), Naletto et al. (2009) and references therein. Iqueye is a conceptually simple fixed-aperture photometer which collects the light within a field of view (FOV) of few arcseconds around the target object. It is mounted at the Nasmyth focus of the 3.6-m ESO NTT. A holed folding mirror at 45 on the NTT focal plane brings a 1 arcmin field around the star under investigation to the field acquisition TV camera. The light from the target object instead passes through the central hole and is collected by a collimating refracting system. Two filter wheels located in the parallel beam after the first lens allow the selection of different filters and polarizers. Then the light reaches a focusing system which (de)magnifies the telescope image by a 1/3.25 factor. On this intermediate focal plane, one out of three pinholes (200, 300 and 500 micrometers diameter) can be inserted. These pinholes act as field stops, and their sizes allow the selection

of three different FOVs (3.5, 5.2 and 8.7 arcsec diameter). After the pinhole, the light impinges on a pyramid having four refracting surfaces and whose tip coincides with the center of the shadow of the secondary mirror. The pyramid splits the telescope pupil in four equal portions, and sends the light from each sub-pupil along four perpendicular arms. Along each arm, the sub-pupil light is first collimated and then refocused by a suitable system, further (de)magnifying the image by an additional 1/3.5 factor. Each sub-beam is then focused on a single photon avalanche photodiode (SPAD) operated in Geiger mode. The quantum efficiency of the Silicon SPADs extends from the blue to the near infrared, with a peak sensitivity of 55% at 550 nm. When used without filter, as in the present case, the overall efficiency of Iqueye (SPAD + telescope + atmosphere) at the Zenith is approximately 33%. The dark counts of the temperature-controlled detectors are very low, varying from 30 to 50 count/s for each individual unit. The SPAD circular sensitive area of 100 μm diameter, nominally defines a 5.8 arcsec FOV. Therefore, the smallest pinhole acts as the actual field stop at 3.4 arcsec. This pinhole can be selected when it is necessary to reduce as much as possible the background around the target, e.g. when observing a pulsar embedded in a nebula, as in the present case. The optical solution of splitting the beam by a pyramid in 4 sub-beams was dictated by the need to overcome as much as possible the dead time intrinsic to the SPAD (75 nanoseconds), in order to give to Iqueye the largest possible dynamic range. In other scientific applications (e.g. intensity interferometry; Hanbury Brown 1974), having four independent detectors allows to cross correlate the counts from each sub-aperture. The pulses produced by the SPADs are sent to a Time to Digital Converter (TDC) board which has a nominal resolution of 24.4 ps. Considering also the other possible noise sources, the nominal accuracy of the photon arrival time determination is of the order of 100 ps or better. An external Rubidium oscillator provides the reference frequency to the TDC board. The board acquires also a pulse per second (PPS) from a GPS receiver, used to remove the Rubidium frequency drift and to put the internal detection times on the UTC scale. Taking into account all error factors, the final overall precision of each time tag in the UTC scale is approximately 450 ps, maintained throughout the duration of the observations. In order to take care as well as feasible of the rotation of the NTT building, the GPS antenna was mounted on the top of the dome, at the centre of one of the sliding doors (about 3 meters away from the dome rotation axis). The signal was brought to the receiver by a high-quality, length compensated cable.

The user interface, developed as a Java multitasking code, controls each subsystem (e.g. the mechanisms), performs the data acquisition and storage, provides some real time monitoring of the data acquisition, and provides

tools for a quick look statistical analysis of the data. Each arrival time is recorded on the storage device which has a total capacity of approximately 2 TB. Being the data stored in a mass memory device, all the data can be analyzed in post-processing: this allows, for example, to sort the collected time tags in arbitrarily long time bins still preserving the original data. Between the January and December 2009 run, some improvements were made to the instrument (Naletto et al. 2010), in particular the addition of a fifth SPAD to acquire the signal from the sky.

5.2 Observations at the NTT telescope: The January and December 2009 runs

The Iqueye team (Naletto et al. 2009) performed observations at the NTT telescope on 14-19 January and 12-16 December 2009, operating Iqueye across its entire range of count rates, from extremely faint to very bright sources. The capability of the apparatus to time-tag photons with extremely accurate precision over a very wide dynamic range was demonstrated convincingly.

The Crab pulsar was observed several times during the two runs (see the log of the observations in Table 5.1). Fig. 5.1 (top) shows the capabilities of Iqueye in conventional high speed photometry. The great sensitivity of Iqueye is clearly evident: it is able to resolve to high accuracy the 33 ms single periods of this weak V = 16.5 object. The pulses from the pulsar are after transmission through a linear polarizer, with the counts binned in 0.5 ms time bins, which is 1/66th of the pulsar period.

Observations of the pulsar PSR B0540-69 in the Large Magellanic Cloud were pursued as well and are described in Appendix B.
A naive experiment to study the spatial second-order degree of light (see Appendix A) has been made by cross correlating the signal from the four channels of Iqueye (Naletto et al. 2009).

Table 5.1: Log of the January/December 2009 observations of the Crab pulsar performed with Iqueye mounted at the NTT telescope in La Silla. The start time of the observations is the GPS integer second, accurate to better than approximately +/-30 nanoseconds.

	Starting time (UTC)	MJD[a]	Duration (s)
1	January 16, 01:55:33	54847.08587011805557	1197
2	January 16, 02:31:07	54847.11459567151620	1797
3	January 17, 01:22:18	54848.06272740807870	3597
4	January 19, 00:48:19	54850.03901748245370	3597
5	January 20, 01:28:31	54851.07300875886574	3712
6	December 13, 03:51:16	55178.16707177530092	1792
7	December 14, 02:36:51	55179.11539707857639	2602
8	December 14, 04:40:15	55179.20109179855324	2596
9	December 15, 03:20:17	55180.14556120746528	2570
10	December 16 02:18:16	55181.10249429464120	1922
11	December 16 03:18:48	55181.14453133057870	892

[a] Corrected MJD at the solar system barycenter (Tempo1 mode).

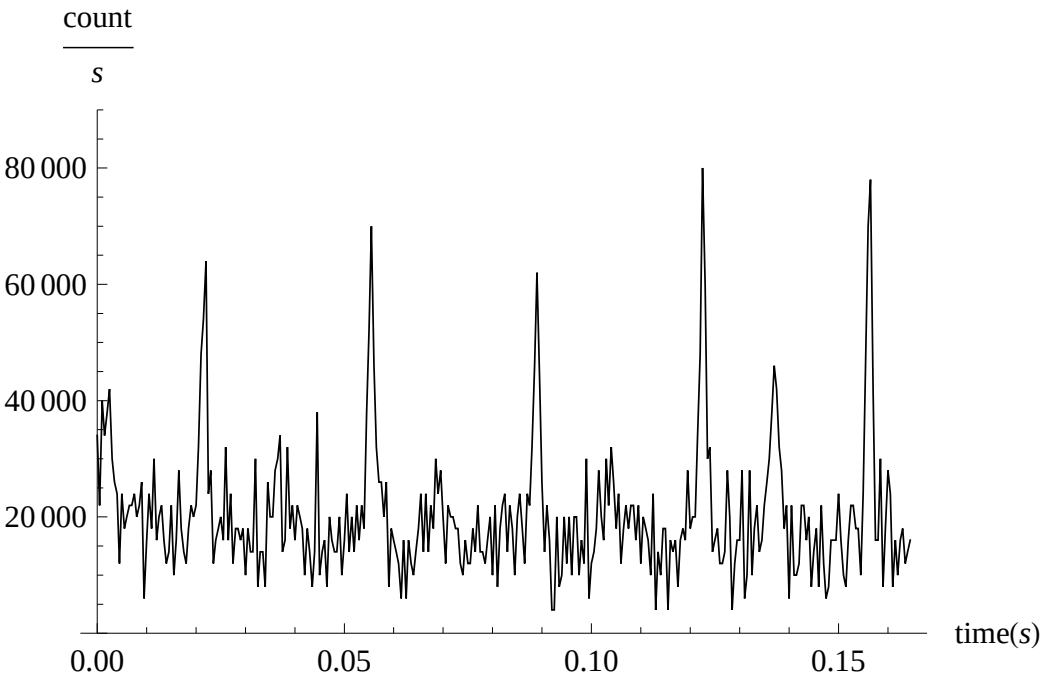

Figure 5.1: The first five pulses from the Crab pulsar as detected by Iqueye at NTT. The bin time is $5 \times 10^{-4} s$

5.3 Rotational periods and first derivative from Iqueye: The January 2009 run

Similarly to Chapter 4 for the Asiago 2008 run, here we report the rotational periods as calculated by Iqueye mounted at the NTT on January 2009. Fig 5.2 shows the results for the January 2009 run. The figure on the top describes the phase-drift behaviour with respect to a reference epoch MJD=54847.0 (see Table 5.1 for a log of the observations) and a folding period P=0.0336252342 s (radio period at MJD=54849.0). The blue points are the Crab phases as measured by Iqueye. The red curve is the radio phase-drift as from the Jodrell Bank monthly ephemerides archive. A zoom-in (middle) shows the best-fitting parabola to the Iqueye phases (blue curve). The offset between the red and the blue curve is the optical-radio phase delay (Shearer et al. 2003; Oosterbroek et al. 2008, see Section 5.5.1). Finally, the figure on the bottom shows the residuals left out after subtracting the best-fitted parabola (blue curve) to the phases (blue points). The spread of the residuals is similar ($\sim 40 \mu s$) to that obtained in the December run (Fig. 5.3). The

Table 5.2: Rotational periods of the Crab pulsar measured by Iqueye on January 2009 compared to those reported by Jodrell Bank radio ephemerides (see Table 5.1 for a log of the observations).

	MJD[a]	Period (NTT) (s)	Period (JB) (s)
1	54847.08587011805557	0.03362516470042	0.03362516469808
2	54847.11459567151620	0.03362516574368	0.03362516574136
3	54848.06272740807870	0.03362520017813	0.03362520017654
4	54850.03901748245370	0.03362527195367	0.03362527195304
5	54851.07300875886574	0.03362530950662	0.03362530950632

[a] Corrected MJD at the solar system barycenter (Tempo1 mode).

best-fitting solution to the optical phase in Fig 5.2 (top) gives

$$\psi(t) = 1.8791 + \frac{0.0000642735}{s}t - \frac{1.85888 \times 10^{-10}}{s^2}t^2 \qquad (5.1)$$

Table 5.2 shows the rotational periods calculated with equation (5.1) in (4.11) (for the observations listed see Table 5.1). Over the run the difference optical-radio oscillates from ~ -2.3 ps to ~ 2.3 ps. The estimated statistical error is $\sim 5 \times 10^{-14}$ s (see Section 4.5), and that quoted by Jodrell Bank is 1.8×10^{-13} s.

The first derivative of the frequency quoted by Jodrell Bank at MJD=54847.0 is $\dot{\nu} \sim -3.7178476 \times 10^{-10} \pm 3.6 \times 10^{-16}$, that obtained from Iqueye in this run is $\dot{\nu} \sim -3.7177633 \times 10^{-10} \pm 2.6 \times 10^{-16}$. They differ by $\sim 8.4 \times 10^{-15}$ ($\sim$ 28 times the estimated error in $\dot{\nu}$). The change of the first derivative all over the run due to the second derivative ($\ddot{\nu} = 1.5 \times 10^{-20}$) is $\ddot{\nu}\Delta T = 1.5 \times 10^{-20} \times 350000s = 5.25 \times 10^{-15}$, where $\Delta T = 350000$ s is the time interval from MJD=54847.0 to the last observation. If we account for $\ddot{\nu}$ then $\dot{\nu} = 3.7177633 \times 10^{-10} + 5.25 \times 10^{-15} = 3.7178158 \times 10^{-10}$ at MJD=54847.0, therefore the radio and optical differ by 11 times the estimated error in $\dot{\nu}$. As in the December run case, both the rotational periods and first derivatives mesured by Iqueye are off those reported by the Jodrell Bank observatory.

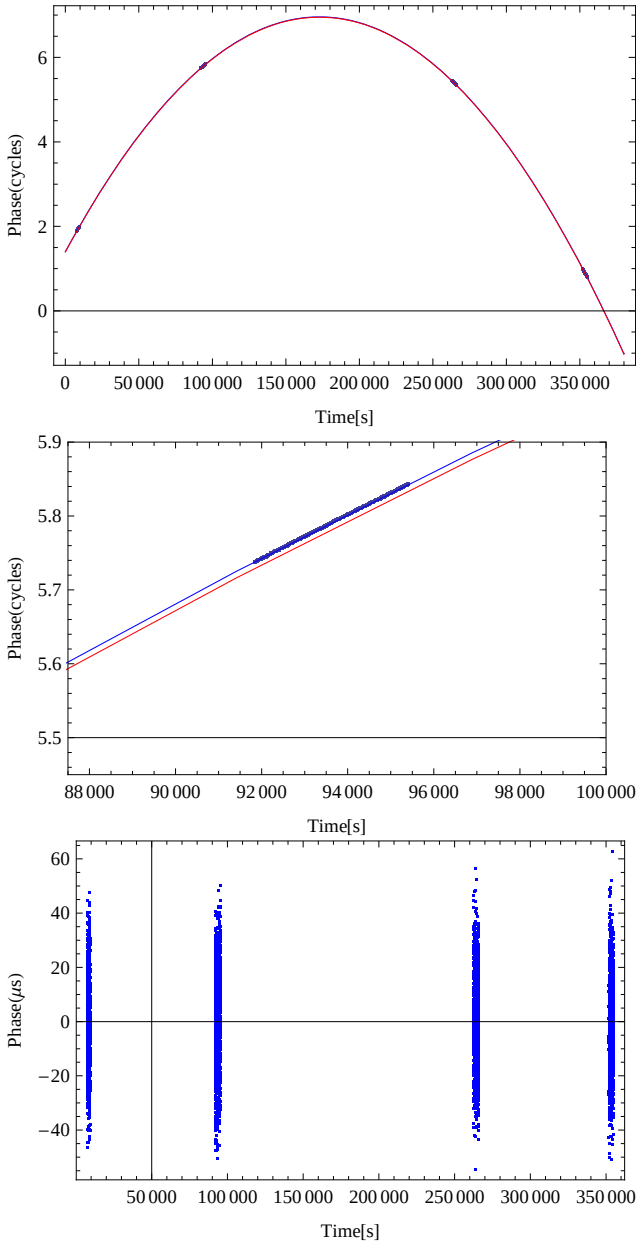

Figure 5.2: *Top*: Behaviour of the phase-drift of the main peak of the Crab over the obsevation run in La Silla on January 2009 (blue points). The blue curve is the best-fitted parabola (eq[5.1]). The red curve is the parabola from the Jodrell Bank radio ephemerides (Section 4.3). *Middle*: A zoom-in of the plot on the top, showing the difference in phase between optical and radio (Shearer et al. 2003; Oosterbroek et al. 2008, see Section 5.5.1). *Bottom*: phase-residuals after subtracting to the blue points on the top the best-fitted parabola (eq[5.1]; blue curve).

5.4 The December 2009 run at NTT

Table 5.3: Rotational periods of the Crab pulsar measured by Iqueye on December 2009 compared to those reported by Jodrell Bank radio ephemerides (see Table 5.1 for a log of the observations).

	MJD[a]	Period (NTT) (s)	Period (JB) (s)
1	55178.16707177530092	0.0336371877769	0.0336371877689
2	55179.11539707857639	0.0336372222108	0.0336372222034
3	55179.20109179855324	0.0336372253224	0.0336372253150
4	55180.14556120746528	0.0336372596163	0.0336372596096
5	55181.10249429464120	0.0336372943628	0.0336372943567
6	55181.14453133057870	0.0336372958892	0.0336372958831

[a] Corrected MJD at the solar system barycenter (Tempo1 mode).

Fig 5.3 shows the parabolic fit to the phase-drift (with respect to the epoch MJD=55178 and to the folding period P=0.0336372543529), a zoom-in to show the offset between the radio and the optical phase (Shearer et al. 2003; Oosterbroek et al. 2008) and the residuals left out after subtracting the best-fitted parabola. Equation (5.2) gives the best-fitted parabola to the phases from Iqueye

$$\psi(t) = 0.85062 + \frac{0.0000642058}{s}t - \frac{1.85715 \times 10^{-10}}{s^2}t^2 \qquad (5.2)$$

The assumed error on each measured phase is the spread of the residuals shown in Fig 5.3 (bottom). Following the same calculations in Section 4.5 the statistical error on the rotational periods determination is $\delta P \sim 2.5 \times 10^{-13}$ s. That reported by Jodrell Bank is $\sim 10^{-13}$ s. Although the statistical error is a bit lower than that obtained by Aqueye, the rotational periods are $\sim 3 - 6$ ps systematically longer than the radio ones, a discrepancy similar to the that noticed in Asiago (~ 3 ps) and in the January NTT run, altough the count rate between Asiago and NTT is different.
The spin down rate of the neutron star is $\dot{\nu} \sim -3.71564 \times 10^{-10} \pm 1 \times 10^{-15}$ and that reported in the Jodrell Bank ephemerides is $\dot{\nu} \sim -3.71436 \times 10^{-10}$. As we already mentioned in Section 4.5 these differences might be caused by oscillations of the dispersion measure and the radio phase leading

to radio ephemerides slighly different than those reported in the JB archive. These discrepancies may also be due to an extra compononent of noise, but further investigations are needed to confirm it. A further discussion on these discrepancies is reported in Section 5.6.

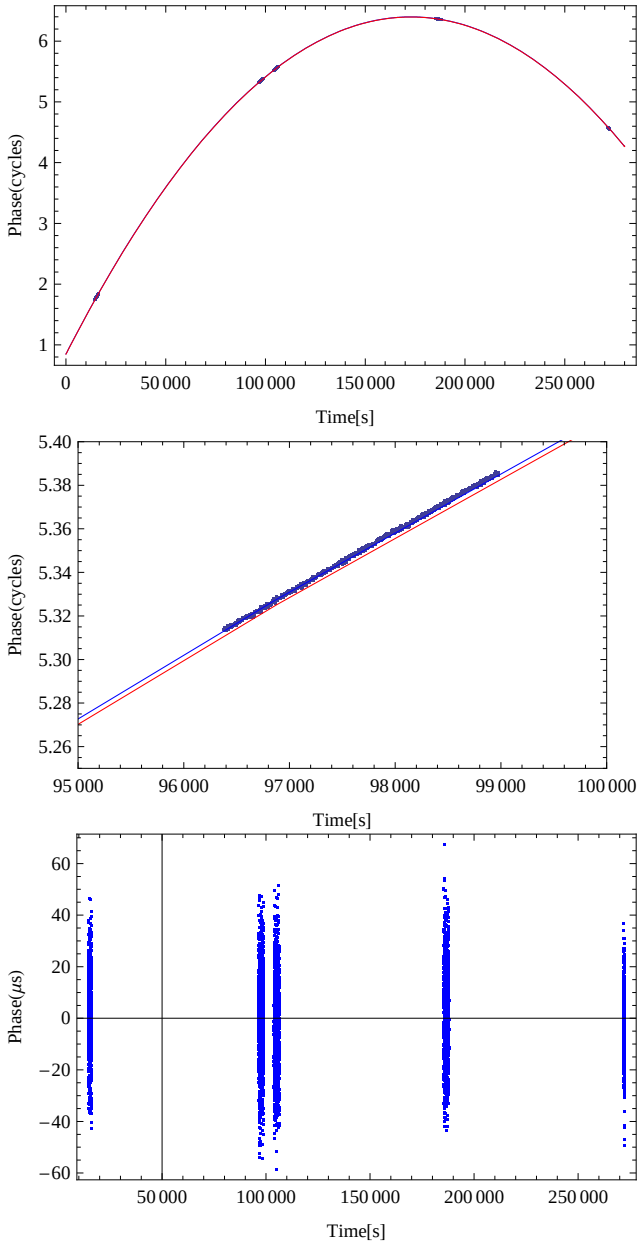

Figure 5.3: *Top*: Behaviour of the phase-drift of the main peak of the Crab over the obsevation run in La Silla on December 2009 (blue points). The blue curve is the best-fitted parabola (eq[5.2]). The red curve is the parabola from the Jodrell Bank radio ephemerides (Section4.3). *Middle*: A zoom-in of the plot on the top, showing the difference in phase between optical and radio (Shearer et al. 2003; Oosterbroek et al. 2008, see sectionv5.5.2)). *Bottom*: phase-residuals after subtracting to the blue points on the top the best-fitted parabola (eq[5.2]; blue curve).

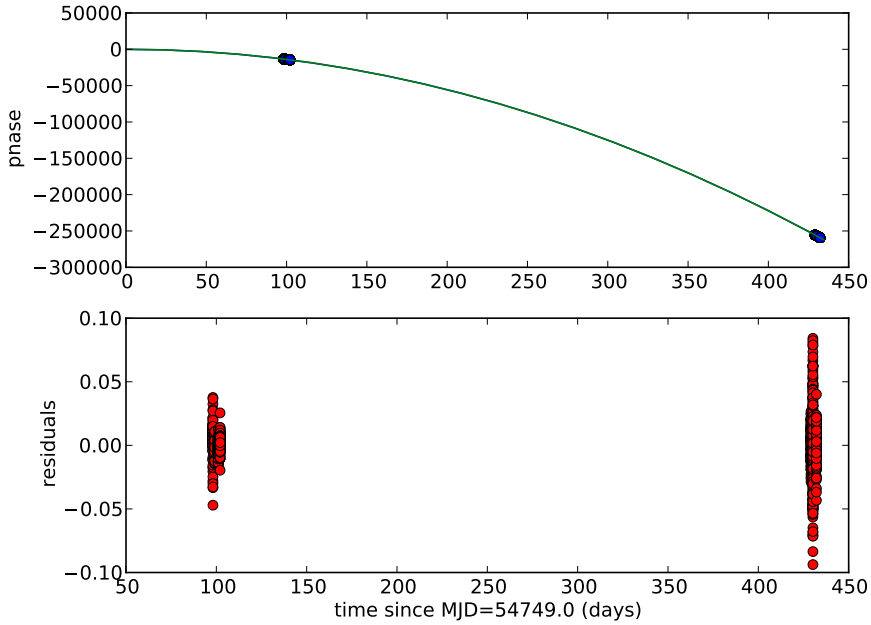

Figure 5.4: Phase-connection of the January-Decmber 2009 run. The symmetric distribution of the residuals shows the Iqueye capability in measuring with high accuracy the phase of the pulsar.

5.5 Phase-residuals analysis: La Silla runs

The analysis of the phase-residuals left out after subtracting the standard pulsar timing model (3.10) may reveal interesting features of the pulsar and its surroundings. As we already have seen in Section 4.4.1, by studying the residuals one can also check for possible discrepancies on the modelling. If some systematic residuals show up, then it is interesting to investigate on the physical origin. A very nice result obtained from the analysis of the phase-residuals was the discovery of the first extrasolar planetary system around the pulsar PSR B1257+12 (Wolszczan & Frail 1992; Wolszczan 1994; Konacki & Wolszczan 2003). Other foundamental results deal with tests of General Relativity theory in the strong field regime (Kramer et al. 2006). Moreover, pulsar timing is now being planned as tool to reveal gravitational wave emission (Stappers et al. 2006).

Fig. 5.4 shows the connection of the phase of the Crab for the two observing runs performed at NTT 11 months apart . The symmetric distribution of the residuals left out after subtracting the best-fitting parabola (Fig. 5.4

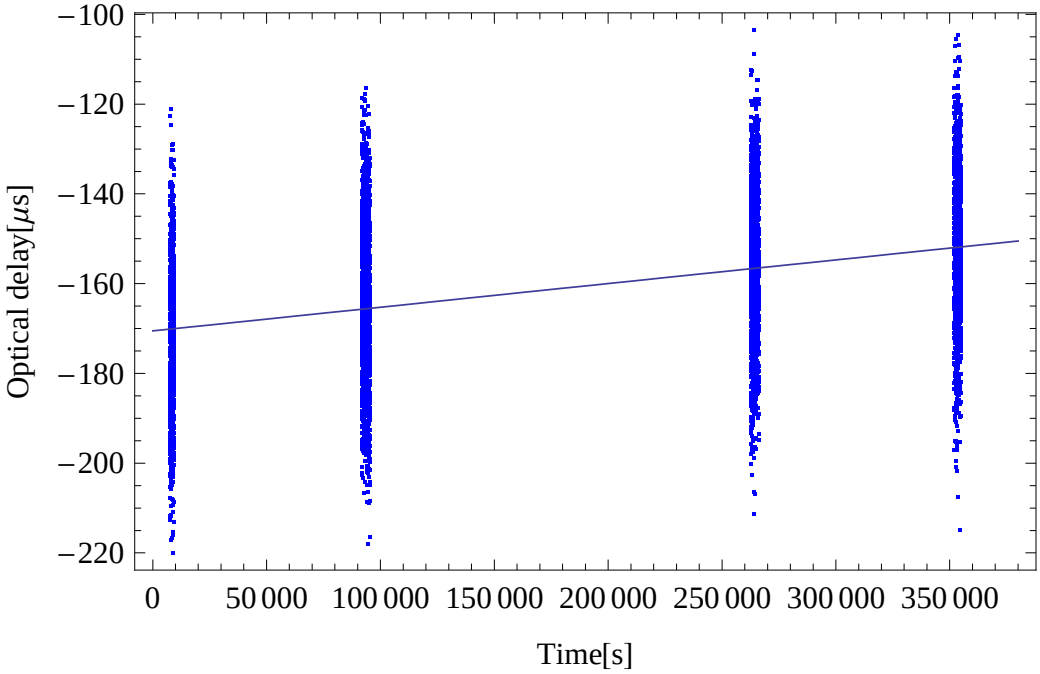

Figure 5.5: *Bottom*: Residual of the time of arrivals of the optical peak, measured by Iqueye, after subtracting the JB radio ones (see Fig. 5.3). The optical peak leads the radio one by $\sim 170\mu s$ (at $t_0 = 0$ see text). The blue line is a linear fit to the residuals giving a drift of the optical peak with respect to the radio one of $\sim 5\mu s/day$. The time t=0 is at MJD=54847 (see Table 5.1 for a log of the observations).

.

bottom) shows that the two data sets can be phase connected. Phases are calculated taking as reference the period at MJD=54749. The sampling interval for the phase is 10 s. The spread of the phases increases with time as the localization of the peak in the folded light curve becomes less accurate. This is caused by the fast motion of the peak at late times. Here a further uncertainty is caused also by the procedure for the localization of the peak itself that is performed by means of a polynomial interpolation.

5.5.1 The January 2009 run

For a log of the observations taken during the January 2009 run at NTT see Table 5.1. Fig. 5.5.1 shows the residual left out after subtracting the Jodrell Bank radio time of arrivals to those measured by Iqueye.

The quoted error on the radio time of arrival at these observation epochs

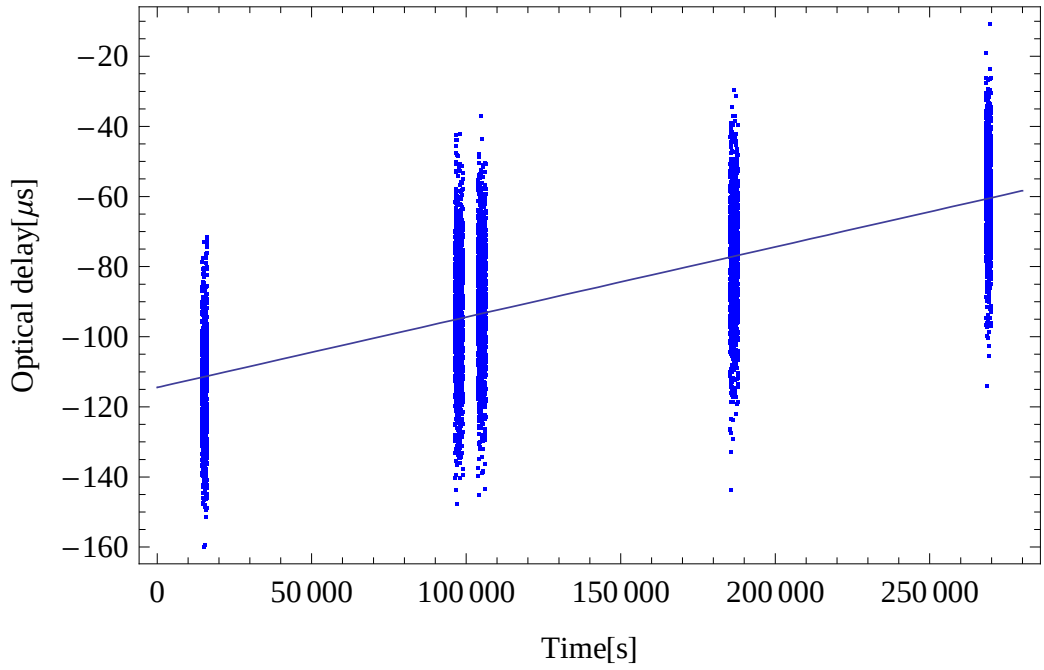

Figure 5.6: Residual of the time of arrivals of the optical peak, measured by Iqueye, after subtracting the JB radio ones (see Fig. 5.3). The negative values means that the optical peak leads the radio one by $\sim 114\mu s$ (at $t_0 = 0$), consistent with the measurements by other observers (Shearer et al. 2003; Oosterbroek et al. 2008). The blue line is a linear fit to the residuals giving a drift of the optical peak with respect to the radio one of $\sim 18\mu s/day$. The time $t = 0$ at MJD=557178 (see Table 5.1 for a log of the observations).

.

(MJD=54846)[1] is $\pm 90\mu s$. As error on each optical time of arrival we assume the spreading of the phase-residuals after subtracting the best-fitted parabola (see Fig. 5.2 bottom), i.e. $\sim \pm 40\mu s$. Assuming a Poissonian statistics, the expected value of the opical time of arrival is uncertain by $40\mu/\sqrt{1730} \sim 1\mu s$ ($N \sim 1730$ is the number of optical time of arrivals measured in each night). Therefore each residuals is uncertain by $\sqrt{(1^2 + 90^2)\mu s^2} \sim 90\mu s$. Fig. 5.5.1 shows an optical peak leading the radio one by $\sim (170 \pm 90)\mu s$ (Shearer et al. 2003; Oosterbroek et al. 2008). The slope gives $\sim (5 \pm 35)\mu s$.

5.5.2 The December 2009 run

Fig. 5.6 shows the residual of the time of arrivals of the optical peak after subtracting the Jodrell Bank radio ephemerides (see Fig. 5.3 top), for the

[1] http://www.jb.man.ac.uk/ pulsar/crab/crab2.txt

data taken in La Silla with Iqueye on December 2009 (see Table 5.1 for a log of the observations). Each points was calculated over intervals 2 s long. From Fig. 5.6 it can be seen that the optical peak leads the radio one by $\sim 100\mu s$, in agreement with other works (Shearer et al. 2003; Oosterbroek et al. 2008).

The quoted error in the Jodrell Bank radio ephemerides[2] on the radio peak is $200\mu s$. Following the estimate in Section 4.5 (now $N \sim 1000$ for each observation night) the error on the expected time of arrival of the optical peak is $\sim 1.3\mu s$. Therefore each residual is uncertain by $\sqrt{(1.3^2 + 200^2)\mu s^2} \sim 200\mu s$. Thus the radio error dominates and our measurements are well within the radio error bar.
The blue line is a linear fit to the residuals and gives a drift of the optical peak with respect the radio one of $\sim (18 \pm 96)\mu s$/day

5.6 Radio-optical phase drifts caused by an extra-noise component?

Let us go back to the measured rotational periods by Aqueye showed in Table 4.3. As a preliminary estimation of the statistical error, we assumed a Poissonian noise (e.g. see Boynton et al. 1972). In Asiago the statistical error is $\sim 1 \times 10^{-12}$ s and the rotational periods are slighlty off the radio ones by $\sim 3 \times 10^{-12}$ s. However the discrepancy is almost within the statistical error, therefore we might not endors firmily conclusions. For the NTT runs disagreemnets larger than the error are more evident than that in Asiago.
Over the temporal baseline of the simultaneous Lj-As run (obs 2, 3, 4 and half of obs 7 in Table 4.1), the statistical error on the rotational periods measured in Asiago is $\sim 1 \times 10^{-12}$ s. If we calculated the rotational periods in Asiago from the best-fitted parabola over the Lj-As run (1 day baseline), they are off with the corresponding in Table 4.3 (entire Asiago run) by $\sim 5 \times 10^{-12}$ s, larger than the statistical errors. Therefore the rotational periods measured by Aqueye (and possible those by Iqueye as well), after barycentering TOAs with Tempo1, are not selfconsistent within the errors. As already pointed out in Section 4.5 it might be an indication of either some uncorrected physical effect in Tempo1 or noise in our data different than the Poissonian one (see also Fig. 4.13). If the measure of a quantity gives values depending on the data used, values differing more than the statistical error, it might mean that the sampling used is affected by some systematic effect, in such a way that each observation contributes with a different weight in the statistical

[2]http://www.jb.man.ac.uk/ pulsar/crab/crab2.txt

analysis.
The difference between radio and optical rotational periods seems to be related to the radio-optical phase drifts shown in Fig. 5.5.1, 5.6, 4.9. Drifts of this type were also noticed in works by J. W. Percival performed with HST (*High Speed Photometer Pulsar Timing and Light Curve Reduction*[3]). For the Asiago run the slope of the blue line in Fig. 4.9 is $\sim -7\mu s/day = -7.7 \times 10^{-11} s/s$, which over the Crab rotational period ($\sim$ 0.033 s) gives rotational periods $\sim$ 3 ps shorter than the radio one, as we already summarized in Table 4.3. Similarly for the December 2009 run: The radio-optical phase drifts is $\sim 18\mu s/day = 2 \times 10^{-10} s/s$ which, over the Crab rotational period, gives rotational periods $\sim$ 7 ps longer than the radio ones. At the end of Section 4.5 we also mentioned that one more possible source of these radio-optical phase discrepancies, thus rotational periods, might be the varying dispersion measure, in such a way that the radio phase reported in the JB archive is slightly different than the actual. However, we above have seen that our optical rotational periods (thus the phase) are not selfconsistent after barycentering TOAs with Tempo1, therefore possible inaccuracies in the radio ephemerides might not be the only cause of these dicrepancies. To check further out whether the problem hides in the Tempo1 emulation mode we barycentered TOAs in Tempo2. We fitted the best-parabola over the As-Lj run and calculated the rotational periods. As in the Tempo1 case, we then compared these periods with those obtained from the best-solution over the entire Asiago run and listed in Table 4.4. As in the Tempo1 case, they differ by $\sim 5 \times 10^{-12}$ s while the statistical error over the As-Lj run is $\sim 1 \times 10^{-12}$ s: They are not selfconsistent within the error. It might mean that the signal from the Crab pulsar is affected by some noise which may not be suitably described by the Poisson statistics. We would stress that we assume *a priori* a Poisson statistics to estimate the error due to the noise, statistics expected for the noise from conuting measurements. We would point out that the statistical error to assign to the measurements needs further investigations. Having in mind these considerations we might not endorse definitive coclusions, but may suspect that the radio-optical phase drifts (we showed in this Chapter and in Section 4.6 for the Asiago run), leading to rotational periods a few ps shorter/longer (see Section 4.5, 5.3, 5.4), might be caused by an extra-noise component (e.g. Lyne et al. 1993; Čadež & Galičič 1996; Čadež et al. 1997, 2001; Scott et al. 2003; Patruno et al. 2009).
Fig. 5.7 is a collage of plots each showing the difference between the best-parabola obtained over the entire run and that obtained with a few observations, for the Asiago, NTT December 2009 and January 2009 run. For

[3]http://www.stsci.edu/hst/hsp/documents/hspisrs.html

the Asiago "reduced" run, obs 2, 3, 4 and half of obs 7 were used (see Table 4.1, 4.3). For the NTT December 2009 run obs 1, 4 and 5 were used to obtained the best-fitted "short" parabola. The other parabola was obtained all over the entire run (Table 5.1, 5.3). Similarly for the NTT January 2009 run one parabola is from the best-fit all over the run, the other using only obs 1, 3 and 5 (Table 5.1, 5.2). From Fig. 5.7 the drifit between the two parabolas (blue parabola) is off the Poissonian error bars ($\sim 5\mu s$ for Asiago, $\sim 1.3\mu s$ for the NTT Dec 2009 run and $\sim 1\mu s$ for the NTT Jan 2009 run). Differences larger than the statistical error may indicate that the signal from the Crab pulsar might be characterized by an extra-noise component not suitable described by the Poissonian statistics (e.g. Patruno et al. 2009). A not yet clear component of noise in pulsars (timing noise) has been observed by other authors, however over much longer integration time than those reported here (Lyne et al. 1993; Scott et al. 2003). With the word "timing noise" one usually refers to what may be left out by the modelling because of its yet unknown nature. Further data analysis is required to have robust conclusions.

Fig. 5.8 shows how much the two parabolas for the Asiago case look like. That is, it descirbes that component making the two parabolas (obtained with different subsets of data) differing each other. We see that the ratio, minus 1, is up to $8\mu s$ at the epoch of some observation (red points). This discrepancy leads to a phase as measured by Aqueye, thus rotational periods, depending on the data set one uses, which is not selfconsistent. In the figure, throught the observation epochs (red points), we interpolated a 15th order polynomial (blue curve). The shape of the blue curve is much alike to that in Lyne et al. (1993) (Fig. 5.8 middle), describing the shape of the timing noise component in the Crab pulsar over many years, with an amplitude of ms. Here we have a curve over days with an amplitude of μs. Boynton et al. (1972) (Fig. 5.8 bottom) report as well sinusoid-like shape curves with different periods and amplitudes, depending on the observation run lenght. Over years with an amplitude of ms, over months hundrends of μs. They also mention that the oscillation seems to have a period which is either 2/3 or 1/3 the lenght of the run.

To conclude, the signal from the Crab pulsar as collected by Aqueye/Iqueye leads us to suspect the existence of some unknown noise component. Future observations and a more extensive data analysis are needed to draw more solid conclusions.

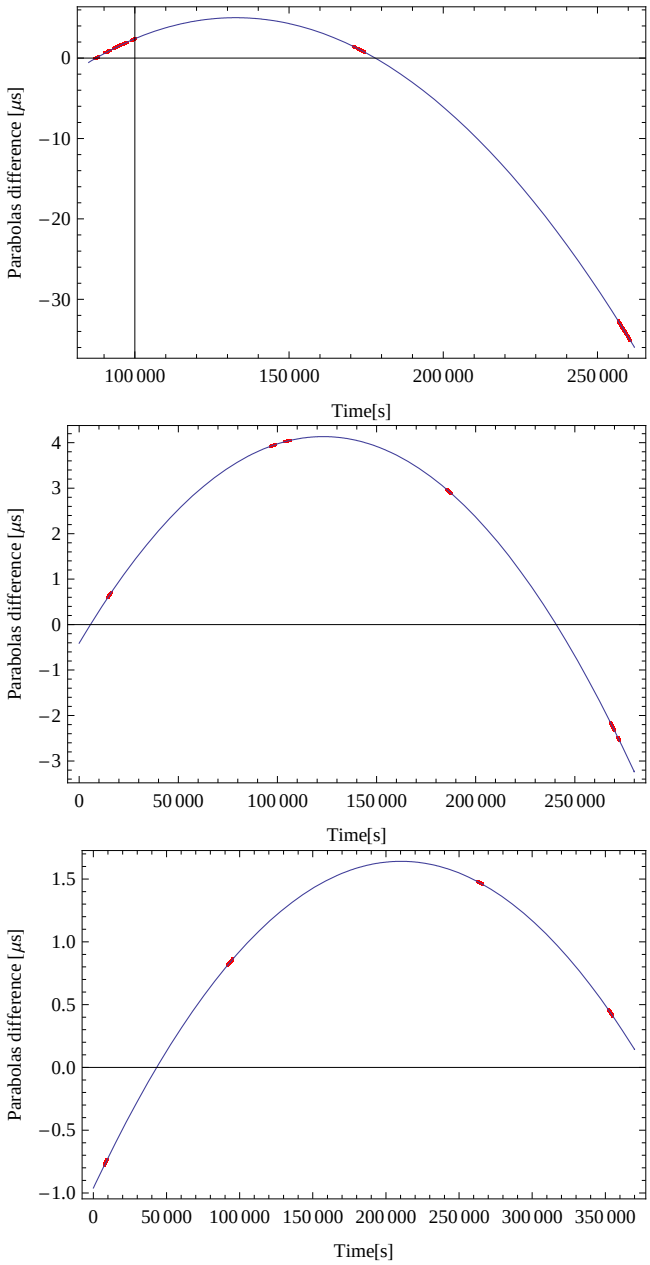

Figure 5.7: Difference of the drift between the best-fitted parabolas over two different set of observations. Red points indicate the epoch of the observations. *Top*: The Asiago parabolas-drift; the statistical Poissonian error bar is $\sim \pm 5\mu s$. One parabola is from the best-fit over the entire obserbvation run, the other is from the best-fit using obs 2, 3, 4 and half of obs 7 (see Table 4.1, 4.4). The drift is huge at the last obs (obs 8): The extrapolated model from the short parabola does not exactly predict where obs 8 shoud fall in the plot (see text). *Middle*: Same as above for the NTT December 2009 run. The statistical Poissonian error bar is $\sim \pm 1.3\mu s$. The difference between the two parabolas is larger than the Poissonian error bar, suggesting an extra-noise component in the signal from the Carb pulsar. *Bottom*: The parabolas-drift for the NTT January 2009 run. The statistical Poissonian error bar is $\sim \pm 1\mu s$.

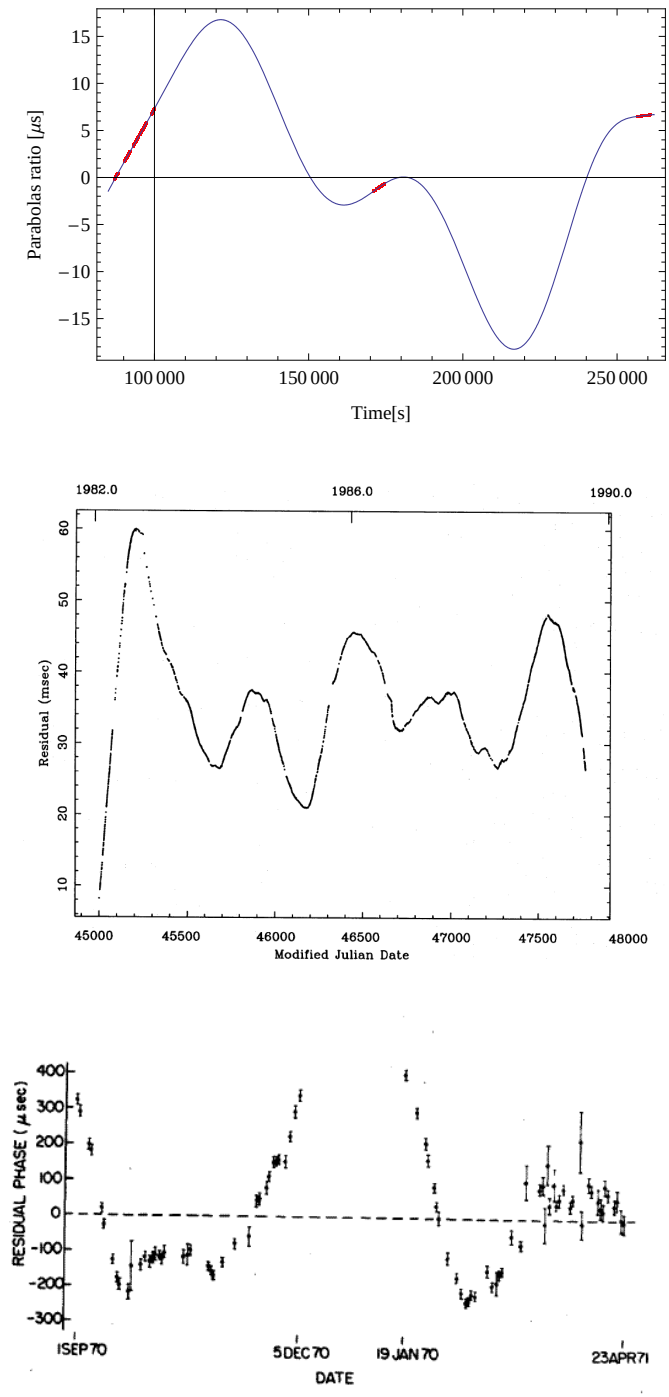

Figure 5.8: Parabolas ratio describing the shape of the component wich makes the two parabolas differing each other (Asiago observation run) (top). One parabola is from the best-fit over the entire observation run, the other is from the best-fit using obs 2, 3, 4 and half of obs 7 (see Table 4.1, 4.4). Sinusoid-like shape curves desribing an extra-noise component in the Crab pulsar are also reported by Lyne et al. (1993) (middle) and Boynton et al. (1972) (bottom).

Chapter 6

Low Mass X-ray Binaries and QPOs

As mentioned in Chapter 1 the Rossi X-ray Timing Explorer satellite (RXTE) discovered millisecond time-scale modulations in the hard X-ray flux from LMXBs. These time-scales are of the order of the Keplerian motion for test-particles orbiting close to the compact object. Therefore, if these quasi-periodic oscillations (QPOs) are produced by modulations at these characteristic frequencies then, in principle, we could use them to give constrains on the mass m and specific angular momentum j of the compact object. Indeed, as shown below, these frequencies depend on these two parameters. This would imply the possibility to constrain the internal structure of a neutron star, that is, the equation of state of matter at nuclear density. Also, one could use QPOs to study the motion of matter in a strongly curved spacetime and check predictions of the General Relativity, such as the existence of an innermost circular orbit (ISCO). Although all these prospects are very exiting, one shuold extremely be careful in the interpretation of the complex phenomenology observed in LMXBs.

This exciting possibility has motivated a number of theoretical investigations (for a general review see van der Klis 2004). Although most of them deal with the motion of matter around the compact object, they differ in the details of the mechanism producing the QPOs (Miller et al. 1998; Morsink & Stella 1999; Abramowicz & Kluźniak 2001; Osherovich & Titarchuk 1999). In this Chapter we will follow the basic idea suggested in this models. We will start describing the motion of test-particles in the Kerr metric. We will then give analytical expressions of the oscillation modes for the motion of a test-particle moving in a quasi-circular orbits. We use these expressions to fit the observed central frequencies of the high frequency QPOs and discuss both implications and limits of this approach. Finally we briefly describe some

recent works accounting for the tidal interaction of matter with the strong gravitational field of a black hole, that maybe related to the underlying twin high frequency QPOs mechanism.

6.1 Motion in a curved space-time

The gravitational field around a rotating black hole is described by the Kerr metric (Kerr 1963). The 4-dimension interval ds^2 in Boyer & Lindquist (1967) coordinates has the following expression

$$ds^2 = \left(-\frac{\Delta A}{B} + \frac{B}{A}\omega^2 \sin^2\theta\right) dt^2 + \frac{B}{A}\sin^2\theta d\varphi^2 + \frac{A}{\Delta}dr^2 + Ad\theta^2 - 2\frac{A}{B}\omega\sin^2\theta d\varphi dt \tag{6.1}$$

where

$$A = r^2 + a^2\cos^2\theta \tag{6.2}$$

$$B = \left(r^2 + a^2\right)^2 - \Delta a \sin^2\theta \tag{6.3}$$

$$\Delta = r^2 - 2mr + a^2 \tag{6.4}$$

$$\omega = \frac{2amr}{B}. \tag{6.5}$$

The previous equations are expressed in geometric units ($G = c = 1$). $m = M/M_\odot$ where M is the mass of the black hole. The parameter a (the angular momentum in geometric units) is related to the the Kerr parameter $j = a/M$, where j is the specific angular momentum of the rotating hole. We can write (6.1) in the compact form

$$ds^2 = g_{\alpha\beta}dx^\alpha dx^\beta \tag{6.6}$$

where $g_{\alpha\beta}$ is the metric tensor

$$g_{\alpha\beta}^{Kerr} = \begin{pmatrix} -\frac{\Delta A}{B} + \frac{B}{A}\omega^2\sin^2\theta & 0 & 0 & -\frac{B}{A}\omega\sin^2\theta \\ 0 & \frac{A}{\Delta} & 0 & 0 \\ 0 & 0 & A & 0 \\ -\frac{B}{A}\omega\sin^2\theta & 0 & 0 & \frac{B}{A}\sin^2\theta \end{pmatrix} \tag{6.7}$$

The indices α and β run from 0 to 3 and describe the time (t=0) and spatial (r=1,θ=2,φ=3) coordinates. In (6.7) we see that the metric coefficients do not depend on ϕ and t. Therefore the t and ϕ components of the 4-momentum (p_t and p_ϕ) are constant of motion. A test particle of mass μ moving in the Kerr metric has:

$$\begin{cases} p_t = -E = const \\ p_\varphi = \Phi = const \end{cases} \tag{6.8}$$

i.e. its energy E and angular momentum Φ are conserved. Their expressions in terms of r, m and a are (Bardeen 1972)

$$\tilde{E} = \frac{r^{3/2} - 2mr^{1/2} \pm am^{1/2}}{r^{3/4}\left(r^{3/2} - 3mr^{1/2} \pm 2am^{1/2}\right)^{1/2}} \tag{6.9}$$

$$\tilde{\Phi} = \pm\frac{m^{1/2}\left(r^2 \mp 2am^{1/2}r^{1/2} + a^2\right)}{r^{3/4}\left(r^{3/2} - 3mr^{1/2} \pm 2am^{1/2}\right)^{1/2}} \tag{6.10}$$

where $\tilde{E}$ and $\tilde{\Phi}$ are in energy and angular momentum divided by the mass μ of the test-particle. The contravariant components of p_t and p_φ are

$$p^t = \mu\frac{dt}{d\tau}\ , \qquad p^\varphi = \mu\frac{d\varphi}{d\tau} \tag{6.11}$$

The variation of φ along the trajectory is

$$\frac{d\varphi}{dt} = \frac{p^\varphi}{p^t}\ . \tag{6.12}$$

Using these expressions, after some math, we can calculate the analytic expression of the Keplerian frequency for the motion of a test-particle in the Kerr metric

$$\begin{aligned} \nu_K &= \frac{d\varphi}{dt} = \frac{1}{2\pi}\left\{\frac{r^2\left(r^2 - 2mr + a^2\right)}{\left[r\left(r^2 + a^2\right) + 2ma^2\right]}\left(\tilde{E} - \omega\tilde{\Phi}\right) + \right. \\ &+ \left. \frac{2mra}{r\left[r\left(r^2 + a^2\right) + 2ma^2\right]}\right\}. \end{aligned} \tag{6.13}$$

For the sake of exactness, (6.13) can not be named "keplerian frequency", since in the Kerr metric one also has to account for the dragging of the inertial frames due to the spinning hole, such that the motion is not keplerian like in the Schwarschild or Minkowski metric. Therefore in the Kerr metric one usually referes to (6.13) as "azimuthal frequency". In the following we will continue to name it "keplerian frequency".

Close to a compact object the orbits should circularize on very short time-scales (Markovic 2000). However in order to study effects due to small deviations from circularity we can calculate the frequency at which a test-particle makes oscillations from the periastron to the apoastron and back, i.e the radial oscillation frequency ν_r. For infinitesimally eccentric orbits, we can write the equation of radial motion $dr/d\tau$ as a Taylor series in $r - r_0$ (r_0 radius of a circular orbit) up to the second order. Since we want to study

very small perturbations in the radial coordinate r, we assume that first order perturbations are negligible and focus on second-order ones. The analytical expression of the radial frequency for orbits with small eccentricity $e \sim 0$, lying in the equatorial plane, is

$$\begin{aligned}
\nu_r &= \frac{\nu_K}{r_0^{7/2}}\left(B_1 - \frac{mra}{\pi\nu_K}\right)\tilde{\Phi}^{-1} \times \\
&\times \left\{-\frac{3a^2}{r_0}\left[1+\frac{4m}{r_0}\right]\tilde{E}^2 + \frac{24am}{r_0^2}\tilde{E}\tilde{\Phi} + \frac{3}{r_0}\tilde{\Phi}^2 + \right. \\
&- \left. 2m\left[1+\frac{6}{r_0^2}\tilde{\Phi}^2\right] + \frac{3a^2}{r_0}\right\}^{1/2}
\end{aligned} \tag{6.14}$$

where r_0 is the radial coordinate the infinitesimal oscillation takes place about.

One more oscillation mode to be taken into account is due to orbits slightly off the equatorial plane. These orbits oscillate in the vertical direction θ about the line of nodes. As before we procede with a Taylor expansion, around $\theta = \frac{\pi}{2}$, of the equation of motion $d\theta/d\tau$ and study second-order perturbations. The vertical frequency for a circular orbit of radius r is

$$\begin{aligned}
\nu_\theta &= \frac{\nu_K}{r^2\tilde{\Phi}}\left(B_1 - \frac{mra}{\pi\nu_K}\right) \times \\
&\times \left\{\frac{a^4}{r^4}\left[\frac{2B_1}{\Delta r^2} - 1\right]\tilde{E}^2 + \left[\frac{1}{B_1}\left(\frac{8m^2a^4}{\Delta r^4} + \frac{4m^2a^4}{B_1 r^2} - \frac{\Delta a^2}{B_1} + 1\right)\right]\tilde{\Phi}^2 + \right. \\
&- \left. \frac{8ma^3}{\Delta r^5}\tilde{E}\tilde{\Phi} - \frac{a^2}{r^4}\right\}^{1/2}
\end{aligned} \tag{6.15}$$

where the subscript (1) means that quantities are calculated at $\theta = \pi/2$.

Following the work by Kennefick & Poisson (1994) we developed a code to calculate these expressions in the more general case of bounded orbits of eccentricity e. The energy E and the angular momentum Φ are expressed as a function of the eccentricity e and the semi-latus rectum p of the orbit, defined such that the periastron of the orbit is $r_p = pM/(1+e)$, with M mass of the black hole and e eccentricity of the orbit. Given the complexity this was done only in the Schwarschild metric, i.e. when the Kerr parameter $j = 0$. More details on calculations in this section are reported in Germanà (2007).

6.1.1 Relativistic frequencis and QPOs

From (6.13) the Keplerian frequency in the Schwarschild metric ($j = 0$) can be written as

$$\begin{aligned} \nu_K &= \frac{\sqrt{GM}}{2\pi r_K^{3/2}} \\ &\sim 1200\ Hz \left(\frac{r_K}{15\ km}\right)^{-3/2} \left(\frac{M}{1.4\ M_\odot}\right)^{1/2} . \end{aligned} \tag{6.16}$$

For a test particle grazing the surface of a neutron star ($M \sim 1.4 M_\odot$, $r \sim 15km$) the Keplerian frequency is ~ 1200 Hz. This frequency is typical of the twin peaks high frequency (HF) QPOs observed in the X-ray flux from LMXBs with a neutron star (NS). For systems with a black hole (BH) the typical frequency of the twin peaks raises $\sim 100 - 400$ Hz. From (6.16) we obtained these values if we rescale for the mass of the compact object, since the innermost keplerian radius r_k scales as M. Therefore HF QPOs in both NS and BH systems may be produced by modulations due to the keplerian motion of matter orbiting the compact object. Blobs of matter may orbit on non-perfect circular orbits and hence they may oscillate at the radial and vertical frequency. Thus, in principle, besides the imprint of the keplerian modulation, also radial and vertical oscillations may be seen in the X-ray power spectra of accreting sources with compact objects, as already suggested by Stella et al. (1999).

The motion of a test particle in a quasi-circular orbit slightly off the equatorial plane is the superposition of the three mentioned modes: azimuthal, radial and vertical. From Fig. 6.1 we see that the radial frequency is smaller than the keplerian one close to the compact object. This peculiar behaviour causes the precession of the orbits. As $\nu_r < \nu_k$, after one complete revolution the particle is not yet at the initial radial position. When it reaches the initial radius, the azimuthal angle is:

$$\Delta\varphi = 2\pi \left[1 - 6\frac{r_g}{r} + 8a\left(\frac{r_g}{r}\right)^{3/2} - 3a^2\left(\frac{r_g}{r}\right)^2\right]^{-1} . \tag{6.17}$$

In a flat space-time ($r/r_g \to \infty$)this quantity is 2π as expected. In a curved space-time $\Delta\phi$ is bigger than 2π and depends on the distance r from the compact object, on its mass m and specific angular momentum j. We refer to this phenomenon as the periastron precession of the orbits. It shows that in a curved space-time eccentric orbits are not closed.
The motion of the periastron occurs at a frequency equal to that of the periastron passage $\nu_p = \nu_k - \nu_r$. From Fig. 6.1 we see that $\nu_p \to 0$ for

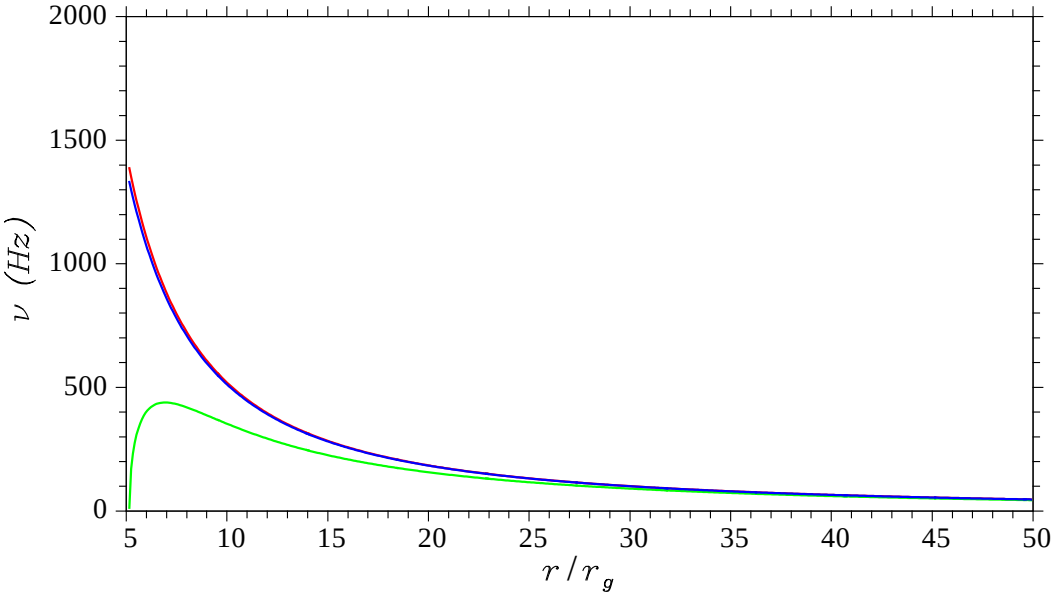

Figure 6.1: Relativistic frequencies for prograde orbits in the Kerr metric for a neutron star with $j = 0.25$ and $m = 1.95 M_{\odot}$. The distance r from the NS is in gravitational radii. The innermost circular orbit (ISCO) is at $\sim 5 r_g$. *Red curve*: Keplerian frequency (eq. [6.13]); *Blue curve*: Vertical frequency (eq. [6.15]); *Green curve*: Radial frequency (eq. [6.14]). Because of the curvature of space-time ν_r reaches a maximum and then drops to zero at the ISCO.

$r \rightarrow \infty$, i.e. in a flat space-time. Also the vertical oscillation frequency ν_θ is different with respect to the keplerian one and this phenomenon induces the precession of the line of nodes of the orbit at a frequency $\nu_{nod} = \nu_k - \nu_\theta$. This phenomenon is known as the Lense-Thirring effect (Lense & Thirring 1918), caused by the dragging of the inertial frames close to a massive spinning body. The effect is a relativistic correction one should account for in order to estimate the correct precession of a gyroscope in the gravitational filed of a spinning body.
All the frequencies we have seen up to here have been invoked to explain both low and high frequency QPOs in accreting X-ray binaries (for a general review, see van der Klis 2004).

6.1.2 The Relativistic Precession Model

In Section 1.5.3 we have seen that a model based on the motion of matter in a strongly curved space-time is the Relativistic Precession Model (RPM; Stella et al. 1999). Fig. 6.2 shows a comparison with the data. The model

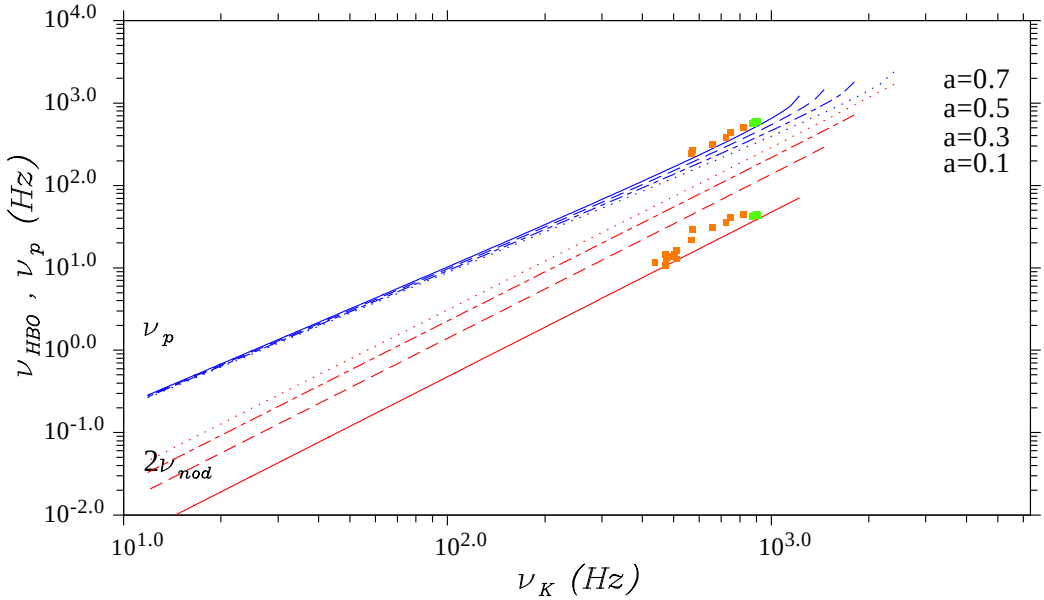

Figure 6.2: Relativistic Precession Model vs observations. Periastron precession frequency $\nu_p = \nu_k - \nu_r$ (*blue curve*) and first overtone of the nodal precession frequency $2\nu_{nod} = 2(\nu_k - \nu_\theta)$ (*red curve*) as a function of the keplerian frequency ν_K. Multiple curves correspond to several values of j for a neutron star with a mass $m = 1.95 M_\odot$. Green points are both HF and LF QPOs observed in the source Scorpius X-1. Orange points are from other sources. We see a remarkble qualitative agreement between the model and the observations for $j \sim 0.1 - 0.2$. HBO on the y axes stands for Horizzontal Branch Oscillation, a class of LF QPOs (Stella et al. 1999).

links the upper peak of twin peaks to the keplerian frequency ν_k, whereas the lower one to the periastron precession frequency ν_p. Low frequency (LF) QPOs (e.g. horizzontal branch oscillations) are linked to twice the nodal precession frequency $2\nu_{nod}$. It is worth noting that the RPM is able to match qualitatively a very complex phenomenon just giving two parameters, i.e. m and j. Subsequent studies have put forward some drawbacks of this model both on the theoretical side and in matching quantitatively the data (e.g Markovic & Lamb 2000).

6.1.3 An alternative interpretation of twin HF QPOs

If QPOs observed in the power spectra of LMXBs are produced by modulations at these characteristic frequencies then, in principle, we could use them to give constrains on m and j. Indeed, as shown above, these frequencies depend on these two parameters. This would imply the possibility to con-

strain the internal structure of a neutron star, that is, the equation of state of matter at nuclear density. Also, one could use QPOs to study the motion of matter in a strongly curved space-time and check predictions of the General Relativity, such as the existence of an innermost circular orbit (ISCO). Although all these prospects are very exiting, one should extremely be careful in the interpretation of the complex phenomenology observed in LMXBs. It is important to stress that, to date, no universally accepted model of the QPO phenomenon exists.

In the following we will describe some ideas on fitting relativistic frequencies to observed twin kHz QPOs in NS LMXBs. We are still basing the mechanism on the relativistic motion as the RPM does, but with a slighlty different interpretation.

We fit the data from systems with a neutron star because in BH LMXBs twin peaks are always detected at a given frequency, i.e. they do not drift up and down as in NS systems they do (van der Klis 2004). Therefore, in BH LMXBs we can not fit any analytical relation showing a dependence on some parameters, since we do not have a range of frequency to fit to.
We use analytical expressions of relativistic frequencies in the Kerr metric to describe geodesics motion around a neutron star. Works by Markovic (2000), and more recently by Török et al. (2010), asses that relativistic frequencies calculated with specific neutron star metrics slightly drift from those obtained in the Kerr metric. Specific neutron star metrics need to be taken into account for describing effects sensytive to the oblatness of the star, i.e. the Lense-Thirring effect, hence the precession frequency of the nodes of the orbits. In the following we will focus our attention only on twin kHz QPOs and link them to the keplerian and apsidal motion ν_r.

We begin considering data from the NS LMXBs Scorpious X-1 (van der Klis et al. 1996). Following the RPM interpretation of twin peaks the upper one is the keplerian frequency ν_k (6.13) whereas the lower peak is the periastron precession frequency of the orbit the blob of matter moves on, i.e. $\nu_p = \nu_k - \nu_r$. We fit the separation of twin peaks, i.e. ν_r (6.14), as function of the keplerian frequency ν_k.

Before doing any numerical fit we should make some assumptions. Following the work by Lattimer & Prakash (2007) on neutron star-structure models we restrict our analysis to the range of reasonable masses and specific angular momentum to be fitted $m = 1.4 - 2.4 M_\odot$ and $j = 0 - 0.5$. The need of putting restrictions on m and j is because of the equation we fit to the data. Indeed we see that the separation of twin peaks ν_r (6.14) dependes on two parameters, m and j. Therefore, once given ν_k in the fit, there are several couples (m, j) giving a similar fit, such that the fit degenerates (see also Török et al. 2010). Therefore we are not interested in determining pre-

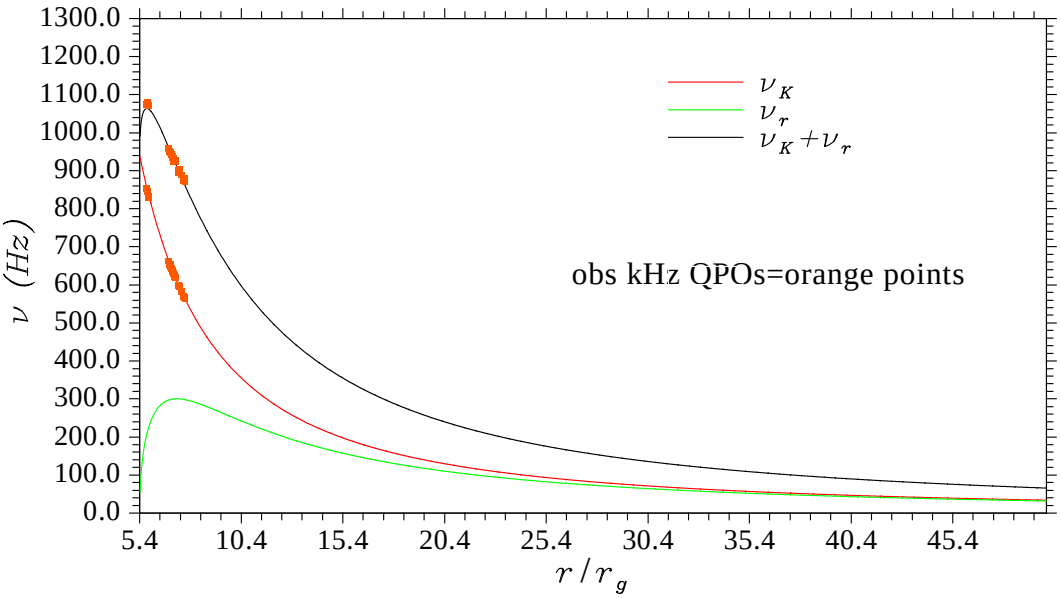

Figure 6.3: Relativistic frequencies vs twin kHz QPOs in the source ScoX-1. Relativistic frequencies are computed from the best-fitting χ^2/dof locus of (m, j) (see Fig. 6.5). Twin peaks may be produced in a region of the space-time around which the radial frequency ν_r (green curve) reaches a maximum.

cise estimates of both m and j. Rather we want to investigate whether we can obtained reasonable numerical fits of relativistic frequencies to observed twin peaks kHz QPOs.

To scan a wide range of mass m and specific angular momentum j we constructed a grid (m, j). As above the mass ranges $m = 1.4 - 2.4 M_\odot$ with a step of 0.1, the specific angular momentum j ranges $j = 0 - 0.5$ and we scanned it with a 0.05 step. Following the RPM we fitted the separation of twin peaks ν_r as function of ν_k, interpreted to be the upper peak of twin peaks. Fig. 6.4 shows the results of the numerical fits. The figure on the top show the χ^2/dof surface (dof stands for degrees of freedom) for all possible combinations of (m, j) in the range as above. The χ^2/dof reaches a deep minimum for $m > 2$ and $0 < j < 0.5$. However when we zoom-in this region (figure on the bottom) we see a minimum $\chi^2/dof \sim 40$ yet big in order to endorse a good numerical fit (in agreement with Markovic & Lamb 2000).

We can give a slightly different interpretation of the twin peaks and checking whether numerical fits improve. From the literature, we know the lower peak always be the more coherent one (see Fig. 1.3; Barret et al. 2005, 2006; Boutelier et al. 2009). Moreover, when RXTE detected these features for the first time, the upper peak was not observed in several sources. To iso-

late it from the noise special improved data analysis techniques had to be developed (Mendez et al. 1998). The keplerian motion is a foundamental oscillation mode instead ν_p is not, thus it appers more suitable to link the keplerian frequency to the more coherent peak, therefore to the lower peak of the twin peaks. In order to understand what to link the upper peak to we can look at the 3:2 ratio the frequencies of twin peaks cluster at (Abramowicz & Kluźniak 2001; Török et al. 2008; Lamb 2003; Belloni et al. 2005; Boutelier et al. 2010). From the proprierties of the space-time we know that the keplerian frequency is twice the radial one where ν_r reaches its maximum (see Fig. 6.1). Thus we link the upper peak to $\nu_k + \nu_r$.

Fig. 6.5 shows the corresponding result of Fig. 6.4 when we link the twin peaks to ν_k and $\nu_k + \nu_r$. Now the χ^2/dof is much smaller all over the grid of (m, j). The minimum $\chi^2/dof \sim 3$ is the azure region shown in the figure on the bottom.

Although the numerical fit is encouring, many aspects of this puzzeling phenomenology remain a matter of debate. If numerical fits with the combination ν_k, $\nu_k+\nu_r$ might be the right way, then we wonder how the modulation at $\nu_k + \nu_r$ is produced. In the next section we show the signal as emitted by a clump of matter tidally disrupted by a black hole. The power spectrum actually shows the peak at $\nu_k+\nu_r$ be the upper one. A model reproducing the observed power spectra is of valuable help in order to understand the working principles of the phenomenon. Besides the relativistic frequencies twin peaks are linked to, a self-consistent model should also describe the observed systematic trends of both the coherence and rms of the peaks (Barret et al. 2006), explaning also why the peaks are produced in a given region of the space-time (see Fig. 6.3), hence describing the energy emission mechanism making QPOs detectable features in a very noisy enviroment.

In Fig. 6.6 and Fig. 6.7 we report the minimum of the χ^2/dof surface for four more sources: GX17+2, a Z-source like Sco X-1, 4U0614+09, 4U1728-34 and 4U1636-53 all atoll-sources. Z-sources are much more luminouses than atoll-sources, accreting close to the Eddington limit (Sanna et al. 2010). We note that the combination ν_k, $\nu_k + \nu_r$ does not work for the peculiar source Circinus X-1 (Boutloukos et al. 2006; Török et al. 2010).
All these plots show a very small χ^2/dof for masses above $2M_\odot$. Such masses are bigger than the canonical neutron star value $1.4M_\odot$. However, in accreting bynary systems a mass of the neutron star larger than the canonical value has been measured (Casares et al. 2006, 2010).

The spin frequency ν_s of some of these neutron stars has been measured from type I X-ray bursts (Méndez & Belloni 2007). In the source in Fig. 6.7 4U1728-34 it was measured to be $\sim 360Hz$ (Méndez & van der Klis 1999). We can roughly draw the locus of (m, j) giving a spin frequency $330Hz <$

$\nu_s < 390Hz$. The spin frequency is given by

$$\nu_s = \frac{1}{2\pi}\frac{G}{c}\frac{M^2}{I}j \tag{6.18}$$

where M is the mass of the neutron star in grams, I its momentum of inertia. From the tables in Morsink & Stella (1999) masses above $2M_\odot$ are only possible with the stiff equation of state (EOS) L. From those tables we read the momentum of inertia I. Crossing the locus of (m, j) giving $330Hz < \nu_s < 390Hz$ with that giving the minimum χ^2/dof (Fig. 6.7), only the couple $(m, j \sim 2.4, 0.2)$ satisfies both the minimum $\chi^2/dof \sim 2$ and the value $\nu_s \sim 363Hz$.

A recent work by Lin et al. (2011) quoted a worse χ^2/dof for both the sources Sco X-1 and 4U1636-53. They argue that the combination ν_k and $\nu_k + \nu_r$ describes well the lower part of the frequencies, the higher part of the observed relation deviates from the theoretical value one expects. They conclude that this may be due because getting closer to the neutron star the phenomenon may be influenced by the dirty surrounding of the star.
Making a direct comparison between our numerical fits with those in Lin et al. (2011) is not straightforward, since the authors do not mention which metric they use to calculate the relativistic frequencies. Moreover, it is not clear why they use only few points out of many to fit the frequencies in the source Sco X-1 (van der Klis et al. 1997; Méndez & van der Klis 2000).
We would stress that the use of QPOs to give precise estimates of both the mass and specific angular momentum may be misleading, because of the many yet poorly understood proprierties of the phenomenon. Rather it may be worth to investigate on the phenomenon by means of numerical simulations able to reproduce what is observed (Čadež et al. 2008; Kostić et al. 2009; Germanà et al. 2009).

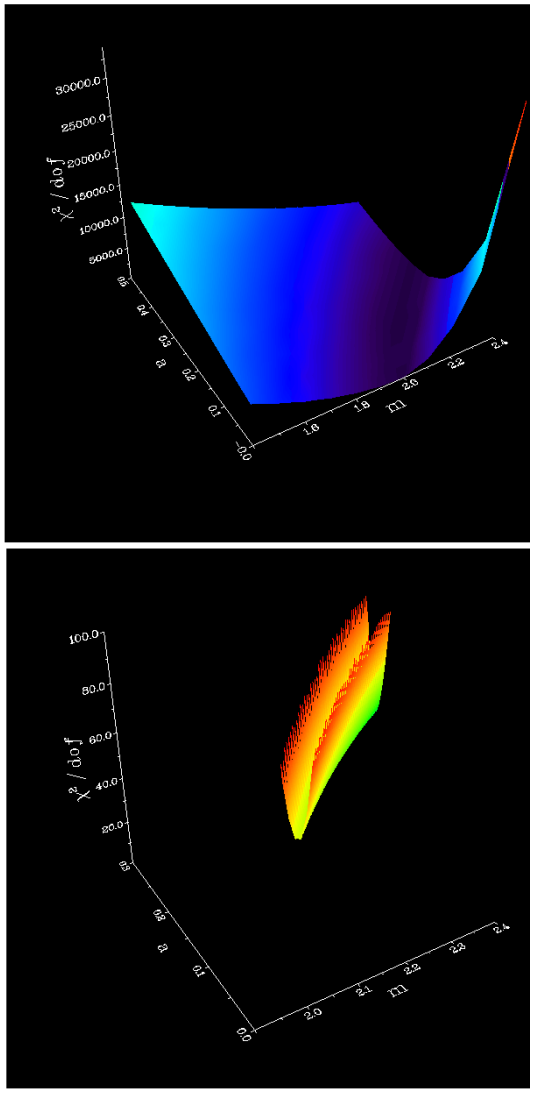

Figure 6.4: Fit of relativistic frequencies to observed kHz QPOs in Sco X-1. *Top*: The χ^2/dof ($dof = 27$) surface for all the possible combinations of (m, j) following the RPM interpretation of twin kHz QPOs. The mass ranges $m = 1.4{-}2.4 M_\odot$, $j = 0{-}0.5$. There is a deep minimum from masses above 2 and $0 < j < 0.3$. Different colours indicate a different χ^2/dof value. *Bottom*: A zoom-in of the region around the minimum χ^2/dof. Although the figure on the top shows a deep minimum, we see that the lowest $\chi^2/dof \sim 40$ is big to endorse a good quantitative numerical fit. In the minimum green region, the χ^2/dof changes of some units.

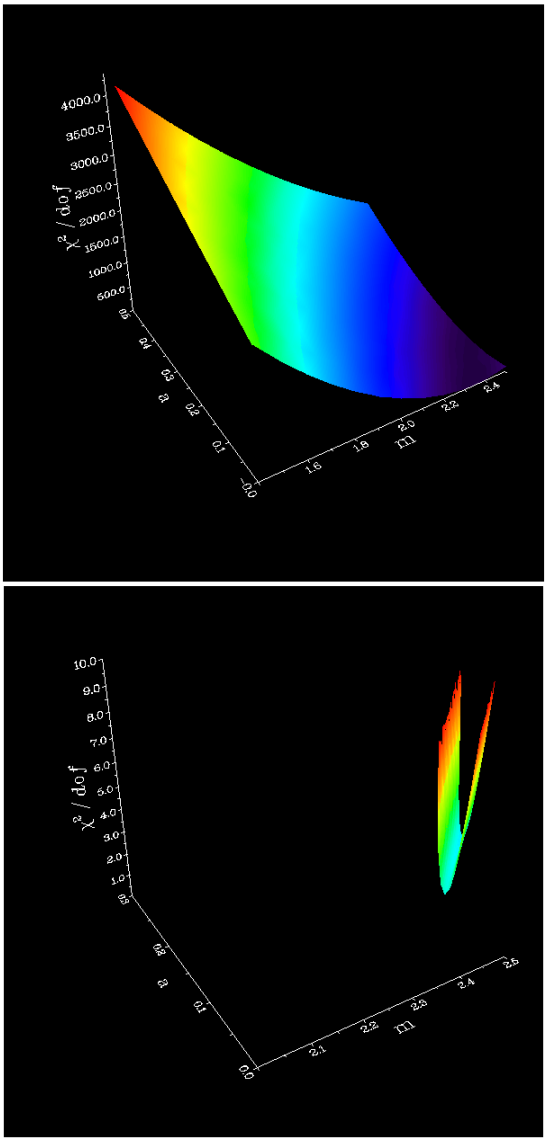

Figure 6.5: Fit of relativistic frequencies to observed kHz QPOs in Sco X-1. *Top*: The χ^2/dof surface for all the possible combinations of (m, j) after interpreting the lower peak of twin peaks as the keplerian frequency ν_k, whereas the upper as $\nu_k + \nu_r$. The mass ranges $m = 1.4 - 2.4 M_\odot$, $j = 0 - 0.5$. There is a deep minimum from masses around ~ 2.4 and $0 < j < 0.3$. Different colours indicate a different χ^2/dof value. *Bottom*: A zoom-in the region around the minimum χ^2/dof above. We see that the lowest $\chi^2/dof \sim 3$ gives a reasonable quantitative numerical fit to the data. In the minimum azure region, the χ^2/dof changes of some units.

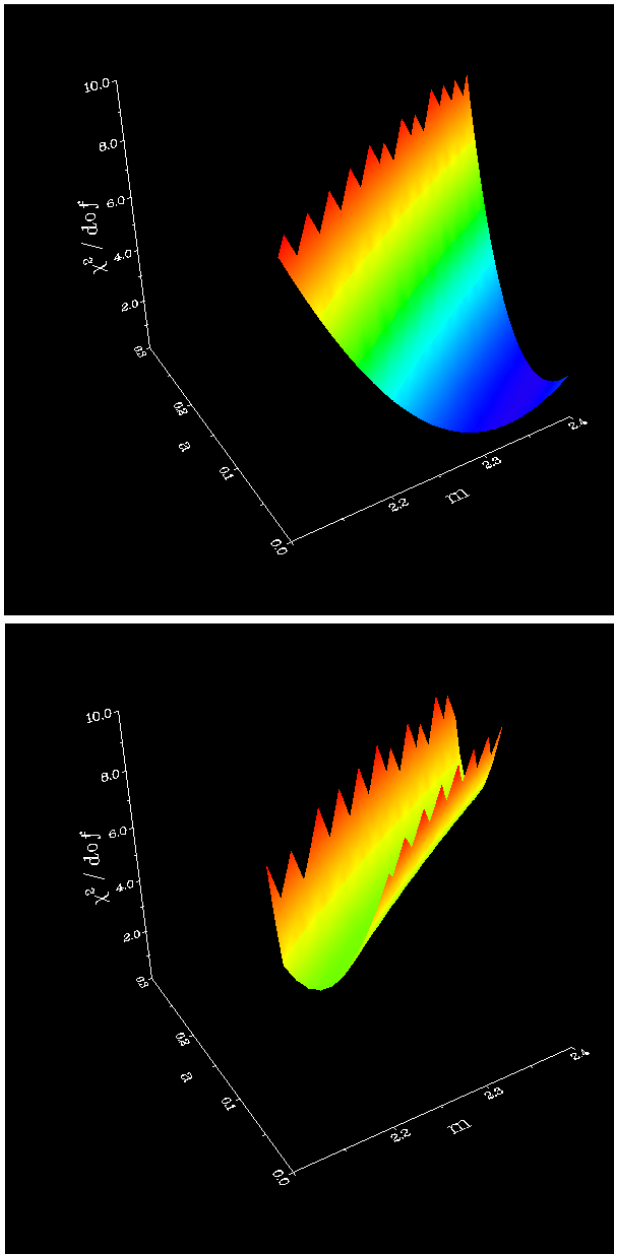

Figure 6.6: Fit of relativistic frequencies to observed kHz QPOs. The upper peak is linked to ν_k the lower one to $\nu_k + \nu_r$. *Top*: The minimum of the χ^2/dof surface for the Z-source GX17+2. The lowest χ^2/dof is ~ 1. The degrees of freedom (dof) are 6. *Bottom*: The minimum of the χ^2/dof surface for the atoll-source 4U0614+09. The lowest χ^2/dof is ~ 6 with $dof = 9$.

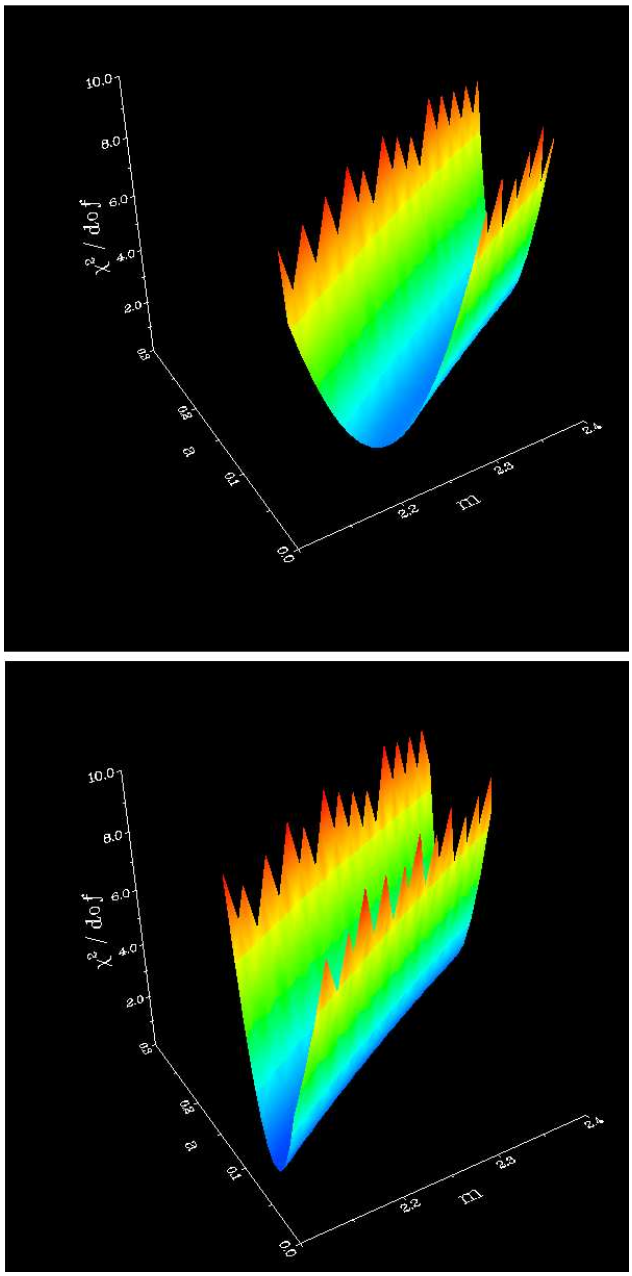

Figure 6.7: Fit of relativistic frequencies to observed kHz QPOs. The upper peak is linked to ν_k the lower one to $\nu_k + \nu_r$. *Top*: The χ^2/dof surface for the atoll-source 4U1636-53. The lowest χ^2/dof is ~ 2 with $dof = 12$. *Bottom*: The χ^2/dof surface for the atoll-source 4U1728-34. The lowest χ^2/dof is ~ 2 with $dof = 13$

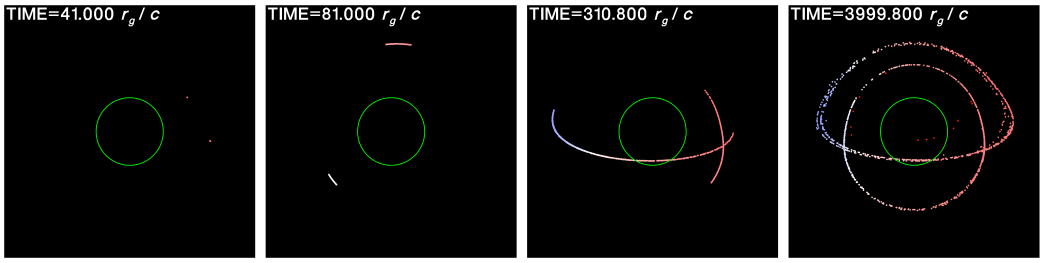

Figure 6.8: The evolution of tidal deformations of a low-mass satellite orbiting a Schwarzschild black hole as seen by an observer 20° above the orbital plane. Due to strong gravitational lensing, two images of the satellite can be seen. The colours correspond to the redshift.

6.2 Tidal effects close to a black hole

In the previous section we have seen that numerical fits of relativistic frequencies to observed QPOs may improve if we asssociate the lower peak to the Keplerian frequency ν_k of a test-particle and the upper peak to $\nu_k + \nu_r$, where ν_r is the radial (or apsidial) frequency.
If QPOs are produced by orbiting blobs of matter close to the compact object then a full-consistent modelling should also account for the interaction of the shape of the blob with the curved geometry of the space-time. Here we show that a blob of matter tidally interacting with a black hole produces a power spectrum that is much alike to those observed.

The tidal evolution of the orbits of low-mass satellites around a Schwarzschild black hole has recently been investigated by Čadež et al. (2008). The numerical code we use (Čadež & Kostić 2005; Kostić 2008; Kostić et al. 2009), allows to study the effects of the strong gravitational field of a black hole on small objects. The appearance of a spherical blob during its tidal evolution, as calculated by numerical simulations, is shown in Figure 6.8. The blob is squeezed and stretched by tidal forces into a bar and then into a ring-like shape along the orbit.

A blob of matter orbiting the black hole on a quasi-circular orbit with a Keplerian frequency ν_k moves from the periastron of the orbit to the apoastron and back with a radial frequency $\nu_r \neq \nu_k$. During this motion the blob undergoes oscillations due to the changing tidal field: At the periastron the tidal force is stronger than at apoastron. Hence the tidal force does work against internal pressure forces and this work is transformed in internal energy of the blob. Gomboc & Čadež (2005) estimated that the energy release during resonant oscillations can be as high as $\sim 0.1\ mc^2$. Therefore, a $\sim$ 150 m blob of dense matter orbiting close to a 10 $M_\odot$ black hole can

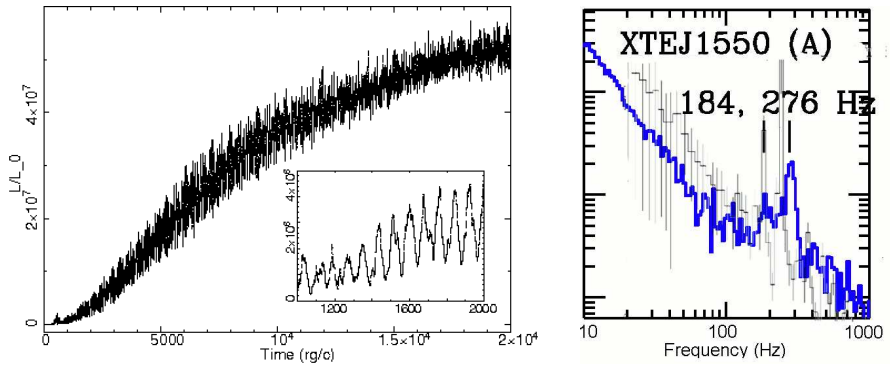

Figure 6.9: *Left*: simulated light curve produced by a clump of matter orbiting a Schwarzschild black hole. *Right*: Fit of the simulated power spectrum (thin line) and the high frequency part of the observed one of the X-ray binary XTE J1550-564 (thick line) (Remillard & McClintock 2006).

radiate energy of $\sim 10^{34}$ erg.

Figure 6.9 (left) shows the light curve produced by the blob in Figure 6.8. In this region of space-time, the Keplerian frequency (ν_k) is almost three times the radial one (ν_r). During tidal evolution, the light curve shows an overall increase in luminosity which is a consequence of increasing emitting area of the source. The luminosity is normalised to its initial value L_0. The time is expressed in $r_{\rm g}/c$ units. For a 10 $M_\odot$ black hole, the light curve lasts for ~ 1 s. The inset in the figure is an enlargement of a small part of the light curve: each peak takes place on a time scale which is almost the expected Keplerian period at this radius. The peaks are due to relativistic effects, such as gravitational lensing, Doppler boosting and blue/redshift.

Figure 6.9 (right) shows the fit of the simulated power spectrum and the high frequency part of the one observed in LMXB XTE J1550-564 that contains a black hole (Germanà et al. 2009). The simulated power spectrum describes the signal emitted by a blob 0.01 r_g big (e.g. $\sim$ 150 m for a 10 $M_\odot$ black hole) orbiting the black hole on an orbit with eccentricity of $e \sim 0.05$ and periastron of ~ 6.1 r_g, that is highly disrupted by the tidal force (Fig 6.8). The simulated power spectrum shows the twin peaks and the observed characteristic power law (Belloni & Hasinger 1990). The upper peak corresopnds to $\nu_k + \nu_r$, the lower one to ν_k.

At present, we are working at the code in order to improve the accuracy of the calculation of the power and coherence of the QPO peaks.

Summary

In light of the novel extremely fast optical photon-counters which have been designed for the future E-ELT (Dravins et al. 2005), prototypes for the Copernico telescope in Asiago (Aqueye, the Asiago Quantum Eye; Barbieri et al. 2008, 2009), for the NTT telescope in La Silla (Iqueye, the Italian Quantum Eye; Naletto et al. 2009, 2010) and for the Vega telescope in Ljubljana were constructed. This new generation of optical photon-counters will allow to study the statistics of the enormous stream of photons collected (e.g. Dravins & Germanà 2008). High-accuracy statistical studies on the time of arrivals of the photons collected requires extreme precise time-tagging. The technology of these instruments is based on Silicon Photon Avalanche Diods (SPADs) and on electronics capable of sustain arrival rates from 10 Hz to 1 GHz (E. Verroi 2011, PhD thesis).
In this PhD thesis we presented the scientific analysis of the data collected from the optical counterpart of the Crab pulsar by means of the novel photon-counters Aqueye and Iqueye. Synchronized observations between Asiago and the other prototype at the Vega telescope in Ljubljana have been discussed as well.

The photons from the pulsar are collected at the observatory, and we refer to them as site arrival times (SATs). Before performing timing analysis some corrections to the SATs need to be done, i.e. we have to reconstruct the time of arrivals (TOAs) as detected by an observer in an inertial reference frame. This is meant to clean TOAs by all the effects they carry imprints of, undergone along the path from the source to the observatory. For instance, for radio frequencies the dispersion measure due to the interstellar medium is relavant. The proper motion of the pulsar also introduces effects affecting TOAs and needs to be taken into account. Photons get through our solar system and therefore their trajectories are distorted by the curvature of the space-time due to the presence of massive bodies such as the Sun, Jupiter, Saturn and the other smaller planets. Precise timing also requires the time beaten by clocks being uniform. In a gravitational field clocks run slower and this effect is also differential, depending on the gravitational potential

the clock lies in. To correct for these effects TOAs are referred to the solar system barycenter (SSB). We applied these corrections to the photons collected by Aqueye/Iqueye by means of the software Tempo2 (Hobbs et al. 2006a; Edwards et al. 2006). Tempo2 is a software meant to model with exterme precision (up to ∼1 ns) TOAs as collected by an inertial observer.

After barycentering TOAs we analyzed them by means of several tools. Light curves and rotational periods of the Crab pulsar were calculated by means of epoch folding techniques, implemented in the software Xronos[1] v. 5.21, distributed by the NASA's High Energy Astrophysics Science Archive Research. By fitting the folded light curve profile to a Fourier series we calculated the statistical error associated to epoch folding thechniques (Larsson 1996). We concluded that our measures are within the error bars (120 picoseconds).

In order to obtain higher-accuracy rotational periods phase-analysis tools were developed by Andrej Čadež (2008, Harrison project report). These technique is widely used in pulsar astronomy. It consists in determining the phase of a given point of the pulsar lght curve profile and follow its behaviour. The phase at each n seconds long integration time interval is usually obtained by cross-correlating the pulsar profile with a standard template. In our analysis the template used is the first derivative of the analytical signal constructed from the observed profile. Its specific implementation is in Čadež (2008, Harrison project report). Cross-correlating the first derivative of the profile to the signal, instead of the profile itself, let us get a high accuracy in measuring the phase of the main peak of the Crab.
With such a tool at hand, we investigated the phase evolution of the Crab pulsar profile calculated every 2 seconds. We noticed inaccuracies in the modelling of the Roemer delay due to wrong Tempo2 configuration files. These problems were noticed on several installations of the software. After correcting for them, from the phase behaviour we calculated the rotational periods of the Crab and compared them to those reported in the Jodrell Bank Crab radio ephemerides archive.
We conclude that the rotational periods measured by Aqueye in Asiago and Iqueye in La Silla agree up to a few picoseconds with the radio ones. However, assuming a Poissonian statistics on the TOAs, as expected for the noise from photon-counting measurements (Boynton et al. 1972), the statistical error in Asiago ($\sim 1 \times 10^{-12}$ s) is sligthly smaller than the radio-optical rotational periods discrepancies ($\sim 3 \times 10^{-12}$ s). For the NTT runs the statistical error is smaller ($\sim 10^{-13}$ s) because of the higher photon-count rate, but the discrapancies with the radio archive on rotational periods are again like those

[1] http://xronos.gsfc.nasa.gov/

in Asiago ($\sim 3 \times 10^{-12}$ s). We were able to measure the spin down of the neutron star ($\sim 4 \times 10^{-13}$ s/s) already over a temporal baseline of 2 days. Discrepancies with the radio measurements larger than the statistical error were reported as well.
By comparing the time of arrival of the optical peak from the Crab at the SSB to that reported in the Jodrell Bank radio ephemerides archive we found that the optical peak leads the radio one by $\sim 120\mu s$, as reported in previous analyses (Shearer et al. 2003; Oosterbroek et al. 2008). Since the radio error bar dominates and since in this PhD project we did not deal with optical-radio simultaneous observations (for some observing run the radio delay is well within the error bar) we might not endorse our results as firmly as other authors did (Shearer et al. 2003; Oosterbroek et al. 2008).

We investigated further out on the optical-radio rotational periods discrepancies mentioned above. They maybe related to radio-optical phase drifts we noticed, although statistically meaningless, and observed by J. W. Percival (*High Speed Photometer Pulsar Timing and Light Curve Reduction*[2]) as well. Then, in more detail, we cross-checked the optical phase measured by Aqueye/Iqueye and we may conclude that the signal collected seems to display an extra-noise component, that is, it seems not to be suitably described by the Poisson statistics. Non-Poissonian noise (timing noise) in the Crab pulsar, and more in general in pulsars, has been noticed and studied by several authors, however over much longer temporal baselines than those reported here (a few days) (e.g. Groth 1975; Helfand et al. 1980; Lyne et al. 1993; Čadež & Galičič 1996; Čadež et al. 1997, 2001; Scott et al. 2003; Patruno et al. 2009). To conclude, the signal from the Crab pulsar as collected by Aqueye/Iqueye leads us to suspect the existence of some unknown noise component. Future observations and a more extensive data analysis are needed to draw more solid conclusions.

An indipendent prototype of very fast photometer with a similar technology was built at the University of Ljubljana by the research group led by prof. Andrej Čadež. Synchronized observations of the Crab pulsar between Asiago (As) and the observatory of Ljubljana (Lj) were pursued. The goal of these joint observations was to show how smooth we can synchronize the phase of the Crab as seen by two of such prototypes at different locations.
The photon statistics in Lj is lower than that in As. We showed a stringent phasing of the Crab pulsar over the entire 16 days Lj run. However, as in the Asiago case, the Crab pulsar rotational periods measured in Lj are off the Jodrell Bank ones by more than the statistical error. They agree within a time window in the run.

[2]http://www.stsci.edu/hst/hsp/documents/hspisrs.html

Regarding the joint As-Lj observations, we have shown that the rotational periods measured from the As-Lj joint observations do not agree within the Poisson error ($\sim 10^{-11}$ s). The difference between the best-fitted solution to the As phases with that fitted to the Lj ones shows, in more detail, that the phase as seen by the two instruments differ more than Poisson error ($\sim 30\mu s$) at some observation epochs. This might be an indication of extra-noise in the source. This issue remains to be investigated with further simulataneous runs.

In this PhD project we also investigated some ideas on modelling the millisecond timing X-ray varaiblity detected in the power spectra of Low Mass X-ray Binaries (LMXBs), with either a netron star or a black hole. These sources mainly emit in the X-ray band and millisecond variability, up to date, has been detected in the X-ray band. Millisecond time-scales are typical for matter orbiting close to the compact object, therefore studying these features might provide a way to investigate the motion of matter close to a compact object, thus probing General Relativity in its strong field limit. Moreover, if such High Frequency Quasi-periodic Oscillations (HF QPOs) are actually produced by energetic X-ray emission from satellites orbiting the compact object, one, in principle, could constrain both the mass and the angular momentum of a neutron star, therefore constraining the equation of state of the matter at nuclear density. Indeed, as we have shown for the Kerr metric case, orbital (ν_k) and apsidial (ν_r) frequencies depend on both the mass (m) and the specific angular momentum (j) of the compact object. This exciting possibility has motivated a number of theoretical investigations (for a general review see van der Klis 2004). Although all these prospects are very exiting, one shuold be extremely careful in the interpretation of the complex phenomenology observed in LMXBs.

HF QPOs often show up as a couple and are named twin peak HF QPOs (e.g. van der Klis et al. 1996). The Relativistic Precession Model (RPM) by Stella et al. (1999) links the upper peak in frequency of twin peaks to the keplerian frequency ν_k of a test-particle orbiting the central object, whereas the lower one to the periastron precession frequency $\nu_p = \nu_k - \nu_r$ of the orbit the test-particle moves on (ν_r is the apsidial oscillation frequency, i.e. from the periastron to the apoastron and back). The RPM is able to match qualitatively a very complex phenomenon just giving two parameters, i.e. m and j. Subsequent studies have put forward some drawbacks of this model both on the theoretical side and in matching quantitatively the data (e.g Markovic & Lamb 2000). We would remark that obtaining precise estimate of both m and j by means of QPOs may be misleading because of the yet poorly understood proprerties of the phenomenology. Therefore in this PhD project we were not interested in determining precise estimates of both m

and j. Rather we wanted to investigate whether we could obtain reasonable numerical fits of relativistic frequencies to observed twin peaks HF QPOs.

We have performed some numerical fits of relativistic frequencies in the Kerr metric to observed HF QPOs in systems with a neutron star (NS LMXBs). We have shown that numerical fits can improve if we give a slightly different interpretation of twin HF QPOS in NS LMXBs (in these systems they are called twin kiloHertz (kHz) QPOs). We have seen that if we link the lower peak of twin peaks to ν_k and the upper one to $\nu_k + \nu_r$ the minimum of the χ^2/dof fit of the relativistic frequencies with respect to the data as a function of m and j reaches a deep minimum for masses of the neutron star above $2M_\odot$. Such masses are bigger than the canonical neutron star value $1.4M_\odot$ infered from binary radio pulsars. However, in accreting bynary systems a mass of the neutron star larger than the canonical value has been measured (Casares et al. 2006, 2010). We note that precise measurements of neutron star masses by means of millisecond QPOs are uncertain because of the yet poorly understood phenomenology.

With this interpretation in mind, in collaboration with Prof. A. Čadež and Dr. U. Kostić from the University of Ljubljana, some simulations were run with a code computing how a distant observer would see the signal emitted by a small satellite orbiting a Schwarschild balck hole and tidally interacting with it. The code was developed by Čadež et al. (2008) and Kostić et al. (2009). The numerical simulations show that a small satellite 150 m large orbiting a hole of $10M_\odot$, on an orbit with eccentricity of ~ 0.05 and periastron r_p at about the innermost circular orbit ($r_p \sim 6.1 r_g \sim 90$ km), produces a signal that is much alike to the observed one (Germanà et al. 2009). From the power spectrum of the simulation both twin peaks HF QPOs are recognized: The lower peak corresponds to the keplerian frequency ν_k, the upper peak to the modulation at $\nu_k + \nu_r$. The simulation shows that, at this radial coordinate, the frequencies of the twin peaks are in a $(\nu_k + \nu_r)/\nu_k = 1.26$ ratio, near to the 3:2 ratio the central frequencies of HF QPOs cluster at (Török et al. 2006). The numerical simulation also reproduces the characterist power law seen in observed power spectra (e.g. Belloni & Hasinger 1990).

A model reproducing the observed power spectra is of valuable help in order to understand the working principles of the phenomenon. Besides the relativistic frequencies twin peaks are linked to, a self-consistent modelling should also describe the observed systematic trends of both the coherence and rms of the peaks (Barret et al. 2006), explaning also why the peaks are produced in a given region of the space-time, hence describing the energy emission mechanism making QPOs detectable features in a very noisy enviroment.

Appendix A

Auto-correlation: understanding the nature of the EM field

The auto-correlation function of the electromagnetic field (EM) can give us information on the nature of the emission mechanism. Let us concentrate only on the electric filed (E), since the magnetic one follows similar concepts. If the function $f(\mathbf{r}, t)$ is the electric field $E(\mathbf{r}, t)$ emitted by a source, from the autocorrelation function we can get information on the spatial and temporal coherence of light. These concepts are the working principles of both the Michelson and Hanbury Brown interferometers. Both of them measure the spatial degree of coherence of light, from which the diameter of the source can be deduced. The Michelson interferometer measures the degree of first-order coherence, auto-correlating the electric field of the light collected at the same instant and at two different spatial points. The Hanbury Brown interferometer measures the degree of second-order coherence.

The first-order auto-correlation function is, at the two spatial-temporal points $(\mathbf{r}_1 t_1)$ e $(\mathbf{r}_2 t_2)$, (Loudon 1973)

$$\left\langle E^* \left(\mathbf{r}_1 t_1\right) E \left(\mathbf{r}_2 t_2\right)\right\rangle = \lim_{T\to\infty} \frac{1}{T} \int_0^T E^* \left(\mathbf{r}_1 t_1\right) E \left(\mathbf{r}_2 t_1 + t_{21}\right) dt_1 \tag{6.19}$$

and the degree of first-order coherence is its normalization

$$\gamma^{(1)} \left(\mathbf{r}_1 t_1, \mathbf{r}_2 t_2\right) \equiv \gamma_{12}^{(1)} = \frac{\left|\left\langle E^* \left(\mathbf{r}_1 t_1\right) E \left(\mathbf{r}_2 t_2\right)\right\rangle\right|}{\left(\left\langle \left|E \left(\mathbf{r}_1 t_1\right)\right|^2 \right\rangle \left\langle \left|E \left(\mathbf{r}_2 t_2\right)\right|^2 \right\rangle\right)^{1/2}}, \tag{6.20}$$

therefore information about the phase of E are preserved. The degree of second-order coherence of light is

$$\gamma^{(2)} \left(\mathbf{r}_1 t_1, \mathbf{r}_2 t_2; \mathbf{r}_2 t_2, \mathbf{r}_1 t_1\right) \equiv \gamma_{12}^{(2)} = \frac{\left\langle E^* \left(\mathbf{r}_1 t_1\right) E^* \left(\mathbf{r}_2 t_2\right) E \left(\mathbf{r}_2 t_2\right) E \left(\mathbf{r}_1 t_1\right)\right\rangle}{\left\langle \left|E \left(\mathbf{r}_1 t_1\right)\right|\right\rangle^2}. \tag{6.21}$$

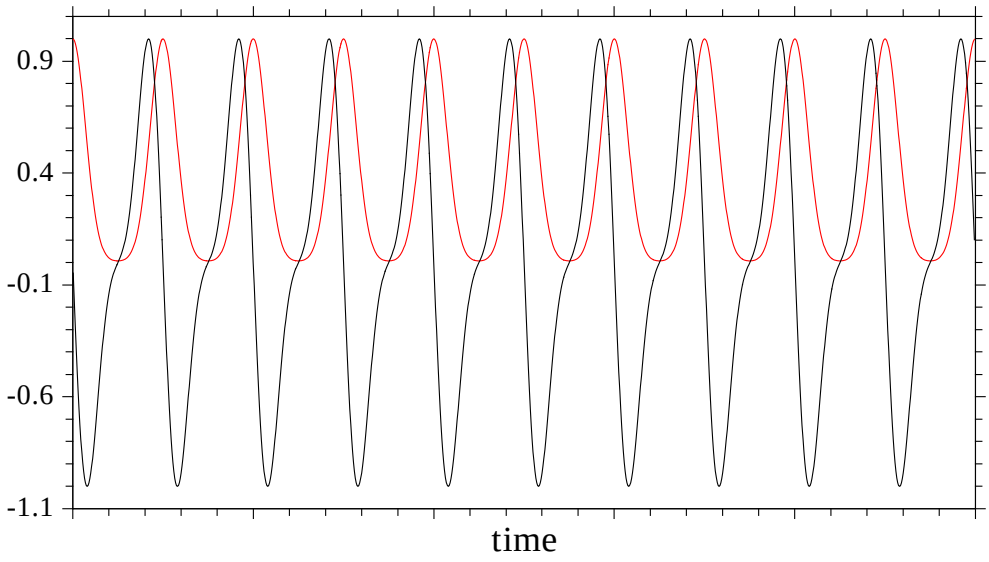

Figure 6.10: *Black curve*: Real part of the electric field from a chaotic process. *Red curve*: Intensity profile of the electric field. The profile is described by a gaussian because of the randomness of the emission mechanism. The width of the gaussian profile rapresents the coherence time of light. The x axes is in random units. For chaotic light it is in 10^{-15} s units. The y axes is normalized to unit (Germanà 2007, Research stay report, Lund Observatory)

and we can write it as

$$\gamma_{12}^{(2)} = \frac{\langle I(\mathbf{r}_1 t_1)\, I(\mathbf{r}_2 t_2)\rangle}{\langle I(\mathbf{r}_1 t_1)\rangle^2}. \tag{6.22}$$

We see that the Hanbury Brown intensity interferometr measures the degree of correlation of the intensity of light, thus information about the phase are lost and the instrument is insensytive to perturbations due to mechanical oscillations of the apparatus or caused by the atmosphere light gets through. In this respect the intensity interferometr has a big advantage with respect to the Michelson one. However since the intensity interferometer measures second-order effects, it requires a high photon-fluxes to reach the minimum required signal-to noise ratio (for more details see Hanbury Brown 1974).

From the working principles of an intensity interferometer one deduces that they can be used to study the coherence time of light, thus studying the nature of the emission mechanisms. Indeed the auto-correlation function at the same point but at two different instants gives information about the coherence time of light, i.e. it tells us how coherent the emission mechanisms is.

The amplitude of an electric filed emitted in a cahotic process (e.g. colliding process) is described by a gaussian whose $FWHM$ is linked to the mean free path of the atomos. For a cahotic process the spectral line has a gaussian shape. The Fourier transform of a gaussian is a gaussian, thus if we Fourier transform the spectral line into the Fourier time domain we get the profile of the intensity of the electric field. Its width is the time-scale over wchich the intensity makes oscillations (Fig. 6.10) and for (6.22) the coherence time of light (Germanà 2007, Research stay report, Lund Observatory).

The intensity-correlation of signals is used in medical and other apllications under the name of *intensity-correlation spectroscopy*. Intensity-correlation spectroscopy was pinoreed by Phillips et al. (1967) to measure in the laboratory the width of extremely narrow spectral line ($\sim 100MHz$). In light of the extremely fast optical photon-counters are being developed (Barbieri et al. 2009; Naletto et al. 2009), the method has recently been proposed (Dravins & Germanà 2008) to give proofs of "suspected" laser emession in astrophysical sources such as η Carinae (Johansson & Letokhov 2007).

Appendix B

The pulsar PSR B0540-69 in the LMC

The pulsar PSR B0540-69 (Seward et al. 1984) is a 50 ms pulsar in the Large Magellanic Cloud, the second brightest ($V \sim 22.5$) in the optical band after the Crab pulsar ($V \sim 16.5$). It has been observed in recent years with a variety of imaging and spectroscopic instruments on ground as well as space telescopes (Serafimovich et al. 2004; Mignani et al. 2010).

B0540-69 has been observed with Iqueye mounted at the NTT telescope in La Silla (Gradari et al. 2010). Table 6.2 shows a log of the observations. The columns UTC and MJD provide values of time and date at mid counting period referred to the barycentre of the solar system in TCB units (Tempo2; Hobbs et al. 2006b).

Gradari et al. (2010) binned the arrival times in convenient time bins, e.g. 1/20 of the expected period, so that standard time-series analysis algorithms can be applied to single out the frequencies in the signal. The Power Spectral Density of the data was dominated by a frequency at the expected (according to the ephemerides available in the literature) value of 19.7433 Hz (period

Table 6.1: Log of the observations of Iqueye at the NTT

Date	UTC (hh mm ss)	MJD (d) (mid-exposure time)	Observation duration (s)
2009 01 18	05 11 10.0	54849.21665	5994
2009 01 20	04 03 19.0	54851.16190	5874
2009 12 14	07 27 59.9	55179.31111	3600
2009 12 15	02 42 00.0	55180.11250	3600
2009 12 16	01 39 59.6	55181.06944	3000
2009 12 18	02 30 00.3	55183.10417	3600

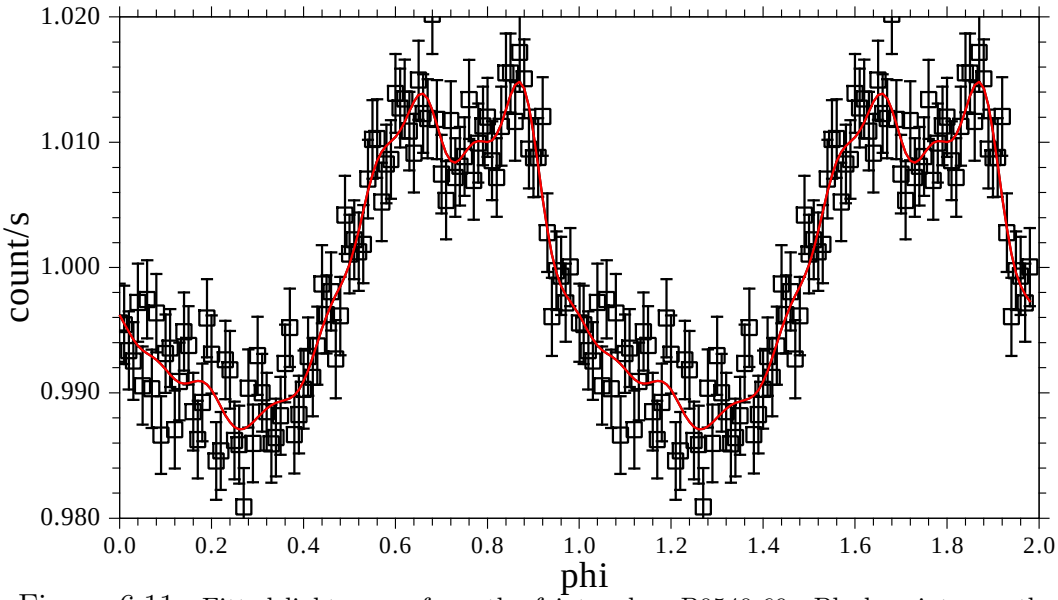

Figure 6.11: Fitted light curve from the faint pulsar B0540-69. Black points are the observed folded light curve. The red line is the fitted Fouriers series. Ten harmonics were used in order to reach a $\chi^2/dof \sim 1$. The characteristic profile of the source is clearly seen.

around 0.05065 s) for January's data and 19.7380 Hz (period around 0.05066 s) for December's data with a statistical significance higher than 20 standard deviations (σ) of noise; no other signal was visible above 30 σ of noise in the range 0-200 Hz.

In order to perform the detailed analysis of the period and light curve, the arrival times of the photons are referred to the barycentre of the solar system, by using the latest release of the Tempo2 software (Hobbs et al. 2006b; Edwards et al. 2006) with the DE405 JPL Ephemerides (Standish 1998).

Figure 6.11 shows both the observed folded profile (black points) and that obtained analitically (red curve) after fitting a Fourier series to tha observed one. An iteration least-square fit procedure was applied. The characteristic double peak profile of B0540 is clearly seen. The data provide the most detailed optical light curve available so far for this pulsar, extending to 27 years the time spanned by X, optical and radio data and allowing a refined determination of the first and second derivatives of the pulsar spin rate. Further details are in Gradari et al. (2010).

Aknowledgements

I would like to thank all the Aqueye/Iqueye team for the work done during the past three years and the help to reach the goals described in this PhD thesis. In particular thanks to Prof. Cesare Barbieri, Prof. Andrej Čadež, Prof. Massimo Calvani and Prof. Luca Zampieri for the support. Thanks again to Prof. Massimo Calvani for his pleasent company and support. Thank you to Dr. Uroš Kostić for the patience shown when I persecuted him with QPOs even during lunch time.

List of Figures

List of Tables

Bibliography

Abdo, A. A., Ackermann, M., Ajello, M., et al. 2010, ApJS, 187, 460

Abramowicz, M. A. & Kluźniak, W. 2001, A&A, 374, L19

Baade, W. & Zwicky, F. 1934, Physical Review, 46, 76

Backer, D. C., Hama, S., van Hook, S., & Foster, R. S. 1993, ApJ, 404, 636

Backer, D. C. & Hellings, R. W. 1986, ARA&A, 24, 537

Barbieri, C., da Deppo, V., D'Onofrio, M., et al. 2006, in IAU Symposium, Vol. 232, The Scientific Requirements for Extremely Large Telescopes, ed. P. Whitelock, M. Dennefeld, & B. Leibundgut, 506–507

Barbieri, C., Naletto, G., Occhipinti, T., et al. 2009, Journal of Modern Optics, 56, 261

Barbieri, C., Naletto, G., Occhipinti, T., et al. 2008, Journal of Modern Optics,

Barret, D., Olive, J., & Miller, M. C. 2005, Astronomische Nachrichten, 326, 808

Barret, D., Olive, J.-F., & Miller, M. C. 2006, MNRAS, 370, 1140

Becker, W. 2009, in Astrophysics and Space Science Library, Vol. 357, Astrophysics and Space Science Library, ed. W. Becker, 91–+

Belloni, T. & Hasinger, G. 1990, A&A, 227, L33

Belloni, T., Méndez, M., & Homan, J. 2005, A&A, 437, 209

Bolton, J. G., Stanley, G. J., & Slee, O. B. 1949, Nature, 164, 101

Boutelier, M., Barret, D., Lin, Y., & Török, G. 2010, MNRAS, 401, 1290

Boutelier, M., Barret, D., & Miller, M. C. 2009, MNRAS, 399, 1901

Boutloukos, S., van der Klis, M., Altamirano, D., et al. 2006, ApJ, 653, 1435

Bowyer, S., Byram, E. T., Chubb, T. A., & Friedman, H. 1964, Science, 146, 912

Boyer, R. H. & Lindquist, R. W. 1967, Journal of Mathematical Physics, 8, 265

Boynton, P. E., Groth, E. J., Hutchinson, D. P., et al. 1972, ApJ, 175, 217

Bradt, H. V., Rothschild, R. E., & Swank, J. H. 1993, A&AS, 97, 355

Carramiñana, A., Čadež, A., & Zwitter, T. 2000, ApJ, 542, 974

Casares, J., Cornelisse, R., Steeghs, D., et al. 2006, MNRAS, 373, 1235

Casares, J., González Hernández, J. I., Israelian, G., & Rebolo, R. 2010, MNRAS, 401, 2517

Cocke, W. J., Disney, M. J., & Taylor, D. J. 1969, Nature, 221, 525

Comella, J. M., Craft, H. D., Lovelace, R. V. E., & Sutton, J. M. 1969, Nature, 221, 453

Cordes, J. M. & Helfand, D. J. 1980, ApJ, 239, 640

Dean, A. J., Clark, D. J., Stephen, J. B., et al. 2008, Science, 321, 1183

Dravins, D., Barbieri, C., Fosbury, R. A. E., et al. 2005, ArXiv Astrophysics e-prints

Dravins, D. & Germanà, C. 2008, in American Institute of Physics Conference Series, Vol. 984, High Time Resolution Astrophysics: The Universe at Sub-Second Timescales, ed. D. Phelan, O. Ryan, & A. Shearer, 216–224

Edwards, R. T., Hobbs, G. B., & Manchester, R. N. 2006, MNRAS, 372, 1549

Fordham, J. L. A., Vranesevic, N., Carramiñana, A., et al. 2002, ApJ, 581, 485

Forman, W., Giacconi, R., Jones, C., Schreier, E., & Tananbaum, H. 1974, ApJ, 193, L67

Frank, J., King, A., & Raine, D. J. 2002, Accretion Power in Astrophysics: Third Edition, ed. Frank, J., King, A., & Raine, D. J.

Fukushima, T. 1995, A&A, 294, 895

Germanà, C., Kostić, U., Čadež, A., & Calvani, M. 2009, in American Institute of Physics Conference Series, Vol. 1126, American Institute of Physics Conference Series, ed. J. Rodriguez & P. Ferrando, 367–369

Gomboc, A. & Čadež, A. 2005, ApJ, 625, 278

Gradari, S., Barbieri, M., Barbieri, C., et al. 2010, ArXiv e-prints

Groth, E. J. 1975, ApJS, 29, 453

Guinot, B. 1988, A&A, 192, 370

Hanbury Brown, R. 1974, The intensity interferometer. Its applications to astronomy (London: Taylor & Francis)

Haymes, R. C., Ellis, D. V., Fishman, G. J., Kurfess, J. D., & Tucker, W. H. 1968, ApJ, 151, L9+

Helfand, D. J., Taylor, J. H., Backus, P. R., & Cordes, J. M. 1980, ApJ, 237, 206

Hewish, A., Bell, S. J., Pilkington, J. D. H., Scott, P. F., & Collins, R. A. 1968, Nature, 217, 709

Hobbs, G., Edwards, R., & Manchester, R. 2006a, Chinese Journal of Astronomy and Astrophysics Supplement, 6, 020000

Hobbs, G., Lyne, A., & Kramer, M. 2006b, Chinese Journal of Astronomy and Astrophysics Supplement, 6, 020000

Horowitz, P., Papaliolios, C., Carleton, N. P., et al. 1971, ApJ, 166, L91+

Hulse, R. A. & Taylor, J. H. 1975, ApJ, 195, L51

Irwin, A. W. & Fukushima, T. 1999, A&A, 348, 642

Johansson, S. & Letokhov, V. S. 2007, New Astronomy Review, 51, 443

Kaaret, P., Yu, W., Ford, E. C., & Zhang, S. N. 1998, ApJ, 497, L93

Kanbach, G., Kruehler, T., Steiakaki, A., & Mignani, R. 2010, The Astronomer's Telegram, 2867, 1

Kanbach, G., Słowikowska, A., Kellner, S., & Steinle, H. 2005, in American Institute of Physics Conference Series, Vol. 801, Astrophysical Sources of High Energy Particles and Radiation, ed. T. Bulik, B. Rudak, & G. Madejski, 306–311

Karpov, S., Beskin, G., Biryukov, A., et al. 2007, ArXiv e-prints

Kennefick, D. & Poisson, E. 1994, Phys. Rev. D, 50, 3816

Kerr, R. P. 1963, Physical Review Letters, 11, 237

Konacki, M. & Wolszczan, A. 2003, ApJ, 591, L147

Kostić, U. 2008, PhD thesis, Univ. Ljubljana

Kostić, U., Čadež, A., Calvani, M., & Gomboc, A. 2009, A&A, 496, 307

Kovacs, G. 1981, Ap&SS, 78, 175

Kramer, M., Stairs, I. H., Manchester, R. N., et al. 2006, Science, 314, 97

Kuiper, L., Hermsen, W., Walter, R., & Foschini, L. 2003, A&A, 411, L31

Lamb, F. K. 2003, in Astronomical Society of the Pacific Conference Series, Vol. 308, Astronomical Society of the Pacific Conference Series, ed. E. P. van den Heuvel, L. Kaper, E. Rol, & R. A. M. J. Wijers, 221–+

Large, M. I., Vaughan, A. E., & Mills, B. Y. 1968a, Nature, 220, 340

Large, M. I., Vaughan, A. E., & Wielebinski, R. 1968b, Nature, 220, 753

Larsson, S. 1996, A&AS, 117, 197

Lattimer, J. M. & Prakash, M. 2007, Phys. Rep., 442, 109

Leahy, D. A. 1987, A&A, 180, 275

Leahy, D. A., Elsner, R. F., & Weisskopf, M. C. 1983, ApJ, 272, 256

Lense, J. & Thirring, H. 1918, Physikalische Zeitschrift, 19, 156

Lin, Y., Boutelier, M., Barret, D., & Zhang, S. 2011, ApJ, 726, 74

Loudon, R. 1973, The quantum theory of light., ed. Loudon, R.

Lundqvist, P., Sollerman, J., Gull, T. R., et al. 1999, in Bulletin of the American Astronomical Society, Vol. 31, Bulletin of the American Astronomical Society, 903–+

Lynds, R., Maran, S. P., & Trumbo, D. E. 1969, ApJ, 155, L121+

Lyne, A. G., Pritchard, R. S., & Graham-Smith, F. 1993, MNRAS, 265, 1003

Manchester, R. N. 2010, Highlights of Astronomy, 15, 233

Markovic, D. 2000, ArXiv Astrophysics e-prints

Markovic, D. & Lamb, F. K. 2000, ArXiv Astrophysics e-prints

McCarthy, D. D. & Luzum, B. J. 2003, Celestial Mechanics and Dynamical Astronomy, 85, 37

McCarthy, D. D. & Petit, G. 2004, IERS Conventions (2003), ed. McCarthy, D. D. & Petit, G.

Méndez, M. & Belloni, T. 2007, MNRAS, 381, 790

Méndez, M. & van der Klis, M. 1999, ApJ, 517, L51

Méndez, M. & van der Klis, M. 2000, MNRAS, 318, 938

Mendez, M., van der Klis, M., van Paradijs, J., et al. 1998, ApJ, 494, L65+

Mignani, R. P. 2009a, ArXiv e-prints

Mignani, R. P. 2009b, ArXiv e-prints

Mignani, R. P. 2010, ArXiv e-prints

Mignani, R. P., Sartori, A., de Luca, A., et al. 2010, A&A, 515, A110+

Miller, M. C., Lamb, F. K., & Psaltis, D. 1998, ApJ, 508, 791

Minkowski, R. 1942, ApJ, 96, 199

Molkov, S., Jourdain, E., & Roques, J. P. 2010, ApJ, 708, 403

Morsink, S. M. & Stella, L. 1999, ApJ, 513, 827

Naletto, G., Barbieri, C., Occhipinti, T., et al. 2009, A&A, 508, 531

Naletto, G., Barbieri, C., Occhipinti, T., et al. 2007, in Society of Photo-Optical Instrumentation Engineers (SPIE) Conference Series, Vol. 6583, Society of Photo-Optical Instrumentation Engineers (SPIE) Conference Series

Naletto, G., Barbieri, C., Verroi, E., et al. 2010, in Society of Photo-Optical Instrumentation Engineers (SPIE) Conference Series, Vol. 7735, Society of Photo-Optical Instrumentation Engineers (SPIE) Conference Series

Nasuti, F. P., Mignani, R., Caraveo, P. A., & Bignami, G. F. 1996, A&A, 314, 849

Nowak, M. A., Vaughan, B. A., Wilms, J., Dove, J. B., & Begelman, M. C. 1999, ApJ, 510, 874

Oosterbroek, T., Cognard, I., Golden, A., et al. 2008, A&A, 488, 271

Osherovich, V. & Titarchuk, L. 1999, ApJ, 522, L113

Patruno, A., Altamirano, D., Hessels, J. W. T., et al. 2009, ApJ, 690, 1856

Percival, J. W., Biggs, J. D., Dolan, J. F., et al. 1993, ApJ, 407, 276

Petit, G. 2003, in Journées 2001 - systèmes de référence spatio-temporels. Influence of geophysics, time and space reference frames on Earth rotation studies, ed. N. Capitaine, Vol. 13, 163–168

Phillips, D. T., Kleiman, H., & Davis, S. P. 1967, Physical Review, 153, 113

Psaltis, D., Belloni, T., & van der Klis, M. 1999, ApJ, 520, 262

Remillard, R. A. & McClintock, J. E. 2006, ARA&A, 44, 49

Richter, G. W. & Matzner, R. A. 1983, Phys. Rev. D, 28, 3007

Rickman, H. 2001, Transactions of the International Astronomical Union, Series B, 24

Rots, A. H., Jahoda, K., & Lyne, A. G. 2004, ApJ, 605, L129

Sanna, A., Méndez, M., Altamirano, D., et al. 2010, MNRAS, 408, 622

Scott, D. M., Finger, M. H., & Wilson, C. A. 2003, MNRAS, 344, 412

Serafimovich, N. I., Shibanov, Y. A., Lundqvist, P., & Sollerman, J. 2004, A&A, 425, 1041

Seward, F. D., Harnden, Jr., F. R., & Helfand, D. J. 1984, ApJ, 287, L19

Shearer, A., Stappers, B., O'Connor, P., et al. 2003, Science, 301, 493

Słowikowska, A., Kanbach, G., Kramer, M., & Stefanescu, A. 2009, MNRAS, 397, 103

Staelin, D. H. & Reifenstein, III, E. C. 1968, Science, 162, 1481

Stairs, I. H., Lyne, A. G., & Shemar, S. L. 2000, Nature, 406, 484

Standish, E. M. 1998, A&A, 336, 381

Stappers, B. W., Kramer, M., Lyne, A. G., D'Amico, N., & Jessner, A. 2006, Chinese Journal of Astronomy and Astrophysics Supplement, 6, 020000

Stella, L., Vietri, M., & Morsink, S. M. 1999, ApJ, 524, L63

Török, G., Abramowicz, M., Kluźniak, W., & Stuchlík, Z. 2006, in American Institute of Physics Conference Series, Vol. 861, Albert Einstein Century International Conference, 786–793

Török, G., Abramowicz, M. A., Bakala, P., et al. 2008, Acta Astronomica, 58, 15

Török, G., Bakala, P., Šrámková, E., Stuchlík, Z., & Urbanec, M. 2010, ApJ, 714, 748

Čadež, A., Calvani, M., & Kostić, U. 2008, A&A, 487, 527

Čadež, A. & Galičič, M. 1996, A&A, 306, 443

Čadež, A., Galičič, M., & Calvani, M. 1997, A&A, 324, 1005

Čadež, A. & Kostić, U. 2005, Phys. Rev. D, 72, 104024

Čadež, A., Vidrih, S., Galičič, M., & Carramiñana, A. 2001, A&A, 366, 930

van der Klis, M. 2004, ArXiv Astrophysics e-prints

van der Klis, M., Swank, J. H., Zhang, W., et al. 1996, ApJ, 469, L1+

van der Klis, M., Wijnands, R. A. D., Horne, K., & Chen, W. 1997, ApJ, 481, L97+

Wijnands, R., van der Klis, M., Homan, J., et al. 2003, Nature, 424, 44

Wolszczan, A. 1994, Science, 264, 538

Wolszczan, A. & Frail, D. A. 1992, Nature, 355, 145

Zampieri, L., Germanà, C., Barbieri, C., et al. 2011, Advances in Space Research, 47, 365